`공학석사 학위논문

Phase Diagram Study and Thermodynamic Assessment of the MgO-MgF_2-Y_2O_3-YF_3 system

MgO-MgF_2-Y_2O_3-YF_3 4원계 시스템의 상태도 실험과 열역학 모델링

2022 년 8 월

서울대학교 대학원

재료공학부

백 승 주

$MgO-MgF_2-Y_2O_3-YF_3$ 4원계 시스템의 상태도 실험과 열역학 모델링

지도 교수 정 인 호

이 논문을 공학석사 학위논문으로 제출함
2022 년 08 월

서울대학교 대학원
재료공학부
백승주

백승주의 공학석사 학위논문을 인준함
2022 년 08 월

위 원 장 ________ 홍 성 현 ________ (인)

부위원장 ________ 정 인 호 ________ (인)

위 원 ________ 정 성 민 ________ (인)

Abstract

The establishment of a reliable thermodynamic database to understand the thermodynamic properties and phase equilibria is crucial in high temperature materials processing including metallurgy, glassmaking, and engineering ceramics fabrications.. As part of a long-term research project to search new ceramic coating materials suitable for plasma environment, the thermodynamic database of MgO-MgF_2-Y_2O_3-YF_3 system was developed based on CALculation of PHAse Diagram (CALPHAD) method. Due to lack of phase diagram experiment data in binary Y_2O_3-YF_3, and MgO-MgF_2-Y_2O_3-YF_3 reciprocal system, the phase equilibria of the binary and reciprocal systems were investigated using a classical equilibration/quenching experiment and differential thermal analysis (DTA). Equilibrium phases were confirmed by electron probe microanalysis (EPMA) and X-ray diffraction (XRD) phase analysis. For the very first time, the entire range of the phase diagram of yttrium oxy-fluoride system up to 1973 K was experimentally determined. It is found that cubic-Y_2O_3 phase dissolves more than 5 mol % of YF_3 at 1973 K. The melting points of YOF and vernier phases are found to be higher than 1973 K and their steep liquidus in the YF_3-rich region are determined. The phase diagram of the MgO-MgF_2-Y_2O_3-YF_3 system was investigated from 1273 to 1773 K for the very first time. Eutectic reactions and isothermal liquidus lines were precisely studied and no existence of ternary or quaternary compound was confirmed. Based on new experimental phase diagram data and thermodynamic property data in the literature, the Y_2O_3-YF_3 and MgO-MgF_2-Y_2O_3-YF_3 systems were thermodynamically modeled by the CALPHAD method and the accurate thermodynamic database was prepared. As applications of the thermodynamic database, metastable solubilities of YF_3 in Y_2O_3 during plasma etching process were calculated.

Keywords : MgO-MgF_2-Y_2O_3-YF_3, YOF, Phase Diagram, Thermodynamics, CAPHAD

Table of Contents

List of Figures

List of Tables

Chapter 1. Introduction

1.1 Research Objective

As oxyfluoride layer and MgO-Y_2O_3 composite are promising candidates for plasma resistant coating materials the thermodynamic behavior of these materials in plasma gas condition is crucial. Furthermore, MgO-MgF_2-Y_2O_3-YF_3 system can be utilized to predict the thermal stability and behavior of magnesia refractory and YSZ in the solid oxide membrane (SOM) process by expanding the database with zirconia and calcium fluoride. However, the accurate and reliable phase diagrams of the system have not been well studied.

The objective of this study is to establish a self-consistent thermodynamic database with high accuracy and predictability of the MgO-MgF_2-Y_2O_3-YF_3 system employing CALculation of PHAse Diagram (CALPHAD) method. In the CALPHAD database development, all available experimental phase diagram and thermodynamic property data are critically evaluated and optimized to find the one set of self-consistent Gibbs energy functions of all phases in the system. The phase diagram and thermodynamic property measurement can be conducted to enable the development, if necessary. The optimization of the MgO-MgF_2-Y_2O_3-YF_3 system was performed using new experimental data and data from the literature. The phase diagram studies for Y_2O_3-YF_3 and MgO-MgF_2-Y_2O_3-YF_3 systems were carried out in order to develop a reliable database of the MgO-MgF_2-Y_2O_3-YF_3 quaternary system.

1.2 Organization

The present thesis comprises the following chapters:

In chapter 2, thermodynamic optimization employing CALPHAD technique is explained. All of the thermodynamic models are introduced to describe the solid and liquid phases in the MgO-MgF_2-Y_2O_3-YF_3 system.

Chapter 3 covered the literature review, phase diagram experiments, and thermodynamic optimization results of the binary Y_2O_3-YF_3 binary system. The materials preparation, experimental method, and characterization techniques which is used to identify the phase diagram of the Y_2O_3-YF_3 system are discussed. The critical evaluation of the previous literatures and thermodynamic optimization process of the binary systems is also described in detail.

In chapter 4, the phase diagram experiment and thermodynamic optimization results of the MgO-MgF_2-Y_2O_3-YF_3 system is presented. The previous studies conducted phase diagram experiment of the MgO-MgF_2, MgF_2-YF_3, and MgO-Y_2O_3 systems were described evaluated. The materials preparation, experimental method, and characterization techniques which is used to define the phase diagram of the MgO-MgF_2-Y_2O_3-YF_3 system are covered.

The summary of the work completed in the present study is presented in the conclusion.

Chapter 2. Thermodynamic Optimization and the CALculation of PHAse Diagrams (CALPHAD) Methodology

2.1 Thermodynamic Optimization

The main purpose of CALPHAD thermodynamic optimization is to construct a thermodynamic database from which the Gibbs energy, enthalpy, entropy, heat capacity, and other properties of a particular system can be calculated. All relevant thermodynamic properties and phase diagram data are collected and critically evaluated by considering experimental errors to establish the thermodynamic database. The thermodynamic concept is used to resolve discrepancies between various experimental data. After determined a system of interest, thermodynamic database is developed from a lower order system (unary and binary) to a high order systems (ternary, quaternaty, …).

The following are the procedures for thermodynamic optimization

1. Select the system of industrial interest

2. Collect experimental data from related literature

   - Thermodynamic data: calorimetric data (heat capacity, enthalpy of formation and mixing), phase equilibria between solid, liquid, and gas, chemical potential (EMF measurement, Knudsen cell measurements), etc. Data related to the multicomponent system can be used to predict the thermodynamic properties of the low-order system using interpolation or extrapolation.

- Crystal structure data: crystal structure data of solid phases (useful in determining solid solutions)

- Evaluate the reliability of all data: Experiments designed to generate data for the same purpose may differ from one another within allowable experimental error range. Besides that, thermodynamic property data and equilibrium experiment data may be conflicting. All experimental data must be sorted and evaluated with their experimental procedure, conditions and analytical methods to solve those problems.

3. Equilibrium experiments and thermodynamic property measurements can be performed if no data is available or the data is unreliable.
   Systematic analogy with the data can also be employed to predict unknown data.

4. An appropriate thermodynamic model needs to be determined to accurately reflect the Gibbs energy of the phases. The solution model should describe the structure of the solution. If the thermodynamic model is appropriate, it can predict the thermodynamic properties and thermodynamic properties in the multicomponent system.

5. The thermodynamic model parameters of each phase are optimized. Thermodynamic optimization was carried out using FactSage™ (version 8.0) thermochemical software. [1] The optimization of parameters were continued so that they can correctly calculate and reproduce all reliable experimental data. It is preferred to minimize the number of model parameters not to cause issues in the multicomponent system.

6. The established thermodynamic database is used to conduct complex predictions and thermodynamic calculations. Predictions of multicomponent systems can be performed for industrial applications.

2.2 Thermodynamic Models

Thermodynamic optimization should be performed by using a thermodynamic model which can appropriately describe the structure of the phase. By using appropriate model, thermodynamic properties and phase equilibria can be defined with a limited number of parameters. Furthermore, the thermodynamic model has a significant impact on the prediction ability of the model in higher order systems. Thus, it is very crucial to choose proper thermodynamic model.

2.2.1 Stoichiometric Compounds

The Gibbs energy of a stoichiometric compound is represented as follows:

$$G_T^o = H_T^o - TS_T^o \qquad (1)$$

$$H_T^o = \Delta H_{298.15\,K}^o + \int_{298.15\,K}^{T} C_p dT \qquad (2)$$

$$S_T^o = S_{298.15\,K}^o + \int_{298.15K}^{T} \frac{C_p}{T} dT \qquad (3)$$

where $\Delta H^{o}_{298.15\,K}$ is the standard enthalpy of formation at 298.15K, $S^{o}_{298.15\,K}$ is the standard entropy at 298.15 K, and C_p is the heat capacity of a compound that is temperature dependent. G^{o}_{T} , H^{o}_{T}, and S^{o}_{T} are the molar Gibbs energy, enthalpy, and entropy of a stoichiometric compound at the absolute temperature T, respectively.

2.2.2 Liquid Solution

The molar Gibbs energy of a pure liquid component A can be expressed as below:

$$g^{o}_{A} = h^{o}_{A} - Ts^{o}_{A}$$

where g^{o}_{A}, h^{o}_{A}, and s^{o}_{A} are the standard molar Gibbs energy, enthalpy, and entropy at absolute temperature T, respectively.

When two components A and B are mixed, the Gibbs energy of the solution is determined by the interaction between A and B as below:

$$G^{m} = (n_A g^{o}_{A} + n_B g^{o}_{B}) - T\Delta S^{config} + \Delta G^{E}$$

in which G^{m} is the Gibbs energy of the solution, n_i is the number of moles of the constituent, i, ΔS^{config} is the configurational entropy, and ΔG^{E} is the excess Gibbs energy which denotes the mixing enthalpy and non-configurational entropy resulting from the interaction between solutions.

$$\Delta G^{E} = (n_A + n_B) g^{E}$$

$$g^{E} = \sum \Delta g^{ij}_{AB} \frac{n^{i}_{A} n^{j}_{B}}{(n_A + n_B)^{i+j}}$$

$$\Delta g_{AB}^{ij} = a + bT + cT^2 + \cdots$$

in which Δg_{AB}^{ij} is an excess interaction parameter term.

2.2.2.1 Ideal Solution and Bragg-Williams Random Mixing Model

If there is no interaction between the solution A and B, they are randomly mixed, which makes the ΔG^E to be zero and ΔS^{config} to be ideal mixing entropy.

$$G^m = (n_A g_A^o + n_B g_B^o) - T\Delta S^{config}$$

$$\Delta S^{config} = -R(n_A lnX_A + n_B lnX_B)$$

Similarly, the liquid solutions are randomly mixed in the Bragg-Williams Random Mixing Model while enthalpy of mixing and non-configurational entropy exist, which makes ΔS^{config} to be expressed as ideal solution while ΔG^E is not zero.

2.2.2.2 Modified Quasichemical Model (MQM)

When a liquid solution significantly differs from an ideal solution, the configurational entropy no longer approaches ideal mixing entropy. This happens in a solution with a strong short range ordering and it is necessary to use absurdly high excess interaction parameters to optimize the solution. It is much harder to conduct good estimation in the multicomponent system due to that kind of high excess interaction parameter. The Modified Quasichemical Model (MQM) was established to represent the Gibbs energy of liquid solution that deviates from a ideal solution. [2]

The MQM describes binary liquid solution by considering short-range ordering of the second-nearest neighbors (SNN) of cations with O^{2-} in oxide melt and that of anions in molten oxy-fluoride solution. The quasi-chemical reaction can be expressed as

$$(A-A)+(B-B)=2(A-B);\ \Delta g_{AB}$$

where A and B are cations in oxide melt like Mg^{2+} and Y^{3+} or O^{2-} and F^{-} in molten oxy-fluoride. $(i-j)$ describes a pair of two cations sharing a common oxygen anion or anions sharing a common cation. Δg_{AB} is the Gibbs energy of the above pair-exchange reaction. The Gibbs energy of the binary liquid solution can be expressed as

$$G^m=(n_A g_A^o+n_B g_B^o)-T\Delta S^{conf}+\frac{n_{AB}}{2}\Delta g_{AB}$$

in which n_i and g_i^o are the number of moles and molar Gibbs energy of the constituent i, respectively. n_{AB} is the moles of $(A-B)$ pair existing at the equilibrium. ΔS^{conf} is the configurational entropy which considers the short-range ordering by the random arrangement of the $(A-A)$, $(B-B)$, and $(A-B)$ pairs.

The configurational entropy can be expressed as

$$\Delta S^{config}=-R(n_A lnX_A+\ n_B lnX_B)-R\left[n_{AA}\ln\left(\frac{X_{AA}}{Y_A^2}\right)+\ n_{BB}\ln\left(\frac{X_{BB}}{Y_B^2}\right)+n_{AB}\ln\left(\frac{X_{AB}}{2Y_AY_B}\right)\right]$$

$$X_A=\frac{n_A}{n_A+n_B}=1-X_B$$

$$X_{ij}=\frac{n_{ij}}{n_{AA}+n_{AB}+n_{BB}}$$

$$Y_A=\frac{Z_A n_A}{Z_A n_A+Z_B n_B}=X_{AA}+\frac{X_{AB}}{2}=1-Y_B$$

where n_i and X_i are the number of moles and site fraction of i in solution, respectively. X_{ij} is pair fraction of $(i-j)$ pair, Y_i is the coordination-equivalent fraction of i, and Z_i is the coordination number of i. Then

$$Z_A n_A = 2n_{AA} + n_{AB}$$

$$Z_B n_B = 2n_{BB} + n_{AB}$$

Δg_{AB} can be described with functions of temperature and pair fractions as

$$\Delta g_{AB} = \Delta g_{AB}^{o} + \sum_{i \geq 1} g_{AB}^{i0} X_{AA}^{i} + \sum_{j \geq 1} g_{AB}^{0j} X_{BB}^{j}$$

in which Δg_{OF}^{o}, g_{OF}^{i0}, and g_{OF}^{0j} are the model parameters which can be functions of temperature. The interaction parameters can be optimized to reproduce the phase diagram and thermodynamic property data.

2.2.2.3 Modified Quasichemical Model for reciprocal system

The Modified Qusichemical Model can be expanded to reciprocal system with two sublattice quadruplet approximation by considering first-nearest-neighbor (FNN) short range ordering (SRO) between sublattices and second-nearest-neighbor (SNN) SRO within a sublattice.[3] When the solution consists of A and B cations and X and Y anions, the liquid solution is made up of the following two sublattices : $(A,\ B)[X,\ Y]$. This reciprocal ionic system applied in the present study is presented in Figure 2.1 by a schematic composition square. The following two reactions are crucial in describing the model.

(i) The exchange reaction among the pure liquid components

For example, the following equation can express the exchange reaction in the A, B // X, Y reciprocal system.

: $A_{1/q_A}X_{1/q_X}(l) + B_{1/q_B}Y_{1/q_Y}(l) = A_{1/q_A}Y_{1/q_Y}(l) + B_{1/q_B}X_{1/q_X}(l);\quad \Delta g_{AB/XY}^{exchange}$

The first-nearest-neighbor (FNN) cation-anion short-range-ordering (SRO) in the oxy-fluoride melts is determined by this equation.

(ii) The second-nearest-neighbor (SNN) pair exchange reactions between cations and between anions.

$(A-X-A)+(B-X-B)=2(A-X-B)\,;\ \Delta g_{AB/XX}$

$(A-Y-A)+(B-Y-B)=2(A-Y-B)\,;\ \Delta g_{AB/YY}$

$(X-A-X)+(Y-A-Y)=2(X-A-Y)\,;\ \Delta g_{AA/XY}$

$(X-B-X)+(Y-B-Y)=2(X-B-Y)\,;\ \Delta g_{BB/XY}$

The second-nearest-neighbor (SNN) SRO between cations and anions is explained by the equation above. The thermodynamic modeling must account for the coupling of the FNN SRO and SNN SRO and the detailed mathematical explanation of the model can be found in Pelton et al. The Gibbs energy of the solution can be expressed as below:

$$G = (n_{AA/XX}g_{AA/XX} + n_{BB/XX}g_{BB/XX} + n_{AA/YY}g_{AA/YY} + n_{BB/YY}g_{BB/YY}) + (n_{AB/XX}g_{AB/XX} + n_{AB/YY}g_{AB/YY} + n_{AA/XY}g_{AA/XY} + n_{BB/XY}g_{BB/XY}) + n_{AB/XY}g_{AB/XY} - T\Delta S^{config} \qquad (9)$$

where $n_{ij/kl}$ and $g_{ij/kl}$ are the number of moles and the molar Gibbs energy of the ij/kl quadruplets, respectively. ΔS^{config} is the configurational entropy of mixing obtained by randomly distributing the quadruplets over the sublattices.

To describe the structure of melt, the FNN and SNN coordination numbers of each cation and anion are assigned.

The Gibbs energies of unary quadruplets at the four corners of the square in Figure 2.1 are derived from that of pure liquid component.

$$g_{AA/XX} = \left(\frac{2q_A}{Z^A_{AA/XX}}\right) g^o_{A_{1/q_A}X_{1/q_X}} = \left(\frac{2q_X}{Z^X_{AA/XX}}\right) g^o_{A_{1/q_A}X_{1/q_X}}$$

where Z_i is the SNN coordination number of i cation, q_i is the ionic charge of i, and g^o_j is the standard molar Gibbs energy of pure liquid j. $g^o_{A_{1/q_A}X_{1/q_X}}$ is the standard Gibbs energy of the pure component per charge equivalent.

The Gibbs energies of the binary quadruplets ($g_{AB/XX}$, $g_{AB/YY}$, $g_{AA/XY}$, and $g_{BB/XY}$) at the edge of the square in Figure 2.1 are calculated using the Gibbs energies of the SNN pair exchange reaction in the binary system as follow:

$$(AA/XX) + (BB/XX) = 2(AB/XX);\ \Delta g_{AB/XX}$$

$$2g_{AB/XY} = g_{AA/XX} + g_{BB/XX} + \Delta g_{AB/XY}$$

where $\Delta g_{AB/XY}$ is an model parameter which can be functions of temperature.

Then, the standard molar Gibbs energy of the AB/XX quadruplets can be expressed as

$$2g_{AB/XX} = \left(\frac{Z^A_{AA/XX}}{Z^A_{AB/X}}\right) g_{AA/XX} + \left(\frac{Z^B_{BB/XX}}{Z^B_{AB/X}}\right) g_{BB/XX} + \Delta g_{AB/XX}$$

In the same way, the standard Gibbs energy of all other quadruplets which is related to the second-nearest-neighbor (SNN) pair exchange reactions can be calculated.

The Gibbs energy $g_{AB/XY}$which is in the center of Figure 2.1 is equal to the weighted average of $g_{AB/XX}$, $g_{AB/YY}$, $g_{AA/XY}$, and $g_{BB/XY}$ as specified in Pelton et al. [3]

$$g_{AB/XY} = \left(\frac{q_X}{Z^X_{AB/XY}} + \frac{q_Y}{Z^Y_{AB/XY}}\right)^{-1} \left(\frac{q_X Z^A_{AA/XX}}{2Z^A_{AB/XY} Z^X_{AB/XY}} \cdot g_{AA/XX} + \frac{q_X Z^B_{BB/XX}}{2Z^B_{AB/XY} Z^X_{AB/XY}} \cdot g_{BB/XX}\right.$$

$$\left. + \frac{q_Y Z^A_{AA/YY}}{2Z^A_{AB/XY} Z^Y_{AB/XY}} \cdot g_{AA/YY} + \frac{q_Y Z^B_{BB/YY}}{2Z^B_{AB/XY} Z^Y_{AB/XY}} \cdot g_{BB/YY}\right)$$

$$+\frac{1}{4}\left(\frac{Z^X_{AB/XX}}{Z^X_{AB/XY}} \cdot \Delta g_{AB/XX} + \frac{Z^Y_{AB/YY}}{Z^Y_{AB/XY}} \cdot \Delta g_{AB/YY} + \frac{Z^A_{AA/XY}}{Z^A_{AB/XY}} \cdot \Delta g_{AA/XY} + \frac{Z^B_{BB/XY}}{Z^B_{AB/XY}}\right.$$

$$\left. \cdot \Delta g_{BB/XY}\right) + \Delta g_{AB/XY}$$

ΔS^{config} is determined by randomly distributing all quadruplets over quadruplet positions but there is no accurate mathematical expression for this so Pelton et al. assumed that ΔS^{config} is equal to $-R\sum n_{ij/kl} ln X_{ij/kl}$ where $X_{ij/kl}$ is the quadruplet fractions. Thus, ΔS^{config} can be expressed as

$$-\Delta S^{config} = (n_A ln X_A + n_B ln X_B + n_X ln X_X + n_Y ln X_Y) + \left(n_{A/X} ln \frac{X_{A/X}}{Y_A Y_X} + n_{B/X} ln \frac{X_{B/X}}{Y_B Y_X} + \right.$$

$$\left. n_{A/Y} ln \frac{X_{A/Y}}{Y_A Y_Y} + n_{B/Y} ln \frac{X_{B/Y}}{Y_B Y_Y}\right) + \left(n_{AA/XX} ln \frac{X_{AA/XX}}{X^4_{A/x}/Y^2_A Y^2_X} + \right.$$

$$\cdots + n_{AB/XX} ln \frac{X_{AB/XX}}{2X^2_{A/x} X^2_{B/X}/Y_A Y_B Y^2_X} + n_{AA/XY} ln \frac{X_{AA/XY}}{2X^2_{A/x} X^2_{A/Y}/Y^2_A Y_X Y_Y} +$$

$$\left. \cdots + n_{AB/XY} ln \frac{X_{AB/XY}}{4X_{A/X} X_{B/X} X_{A/Y} X_{B/Y}/Y_A Y_B Y_X Y_y}\right)$$

2.2.3 Solid Solution

In the present study, solid solutions including cubic-Y_2O_3 (*c*-Y_2O_3), hexagonal-Y_2O_3(*h*-Y_2O_3) and hexagonal-YF_3(*h*-YF_3) were described based on their crystal structure and phase diagram data. The detailed crystal structure and explanation of every phase will be covered later. The

Bragg-Williams random mixing model is also employed to assess the solid solution in the same way that it can be used to liquid solution which is described in 2.2.2.1.

2.2.3.1 Compound Energy Formalism

The Y_2O_3 solution phases have been optimized using the Compound Energy Formalism (CEF). [4] The CEF is adjusted based on the crystal structure of the solid solution. For example, if we consider a solid solution which may be described by the formula, $(A,B)_i(C,D)_j$, in which A and B are mixed on the first sublattice and C and D on the second. The end-members compounds can be represented by the combination of species from each sublattice such as A_iC_j, A_iD_j, B_iC_j, and B_iD_j. Then, the Gibbs energy of the solution can be defined on the basis of the Gibbs energy of end members, $g^o_{A_iC_j}$, $g^o_{A_iD_j}$, $g^o_{B_iC_j}$, and $g^o_{B_iD_j}$. The Gibbs energy of the solution (per formula mole) is expressed as below:

$$G = y_A y_C g^o_{A_iC_j} + y_A y_D g^o_{A_iD_j} + y_B y_C g^o_{B_iC_j} + y_B y_D g^o_{B_iD_j}\, iRT(y_A ln y_A + y_B ln y_B) \\ + jRT(y_C ln y_C + y_D ln y_D) + \left(\sum_{k=C,D} y_A y_B y_k L_{AB:k} + \sum_{k=A,B} y_k y_C y_D L_{k:CD} \right)$$

in which y_i is the site fractions of component i and $L_{ij:k}$ and $L_{k:ij}$represent excess interaction parameter between i,j, and k. The CEF is based on the premise that the components in each sublattice are randomly distributed. The Gibbs energies of end members define interactions between elements in different sublattices, and excess parameter terms describe interactions between elements in the same sublattice, which can be a constant or extended to the function of temperature.

2.2.4 Metallic and Gas Phases

The Gibbs energy of solid Y and Mg from FactSage FactPS database were used to calculate the end members of solid solutions. FactSage FactPS database is also applied to obtain the Gibbs energy of all gas species.

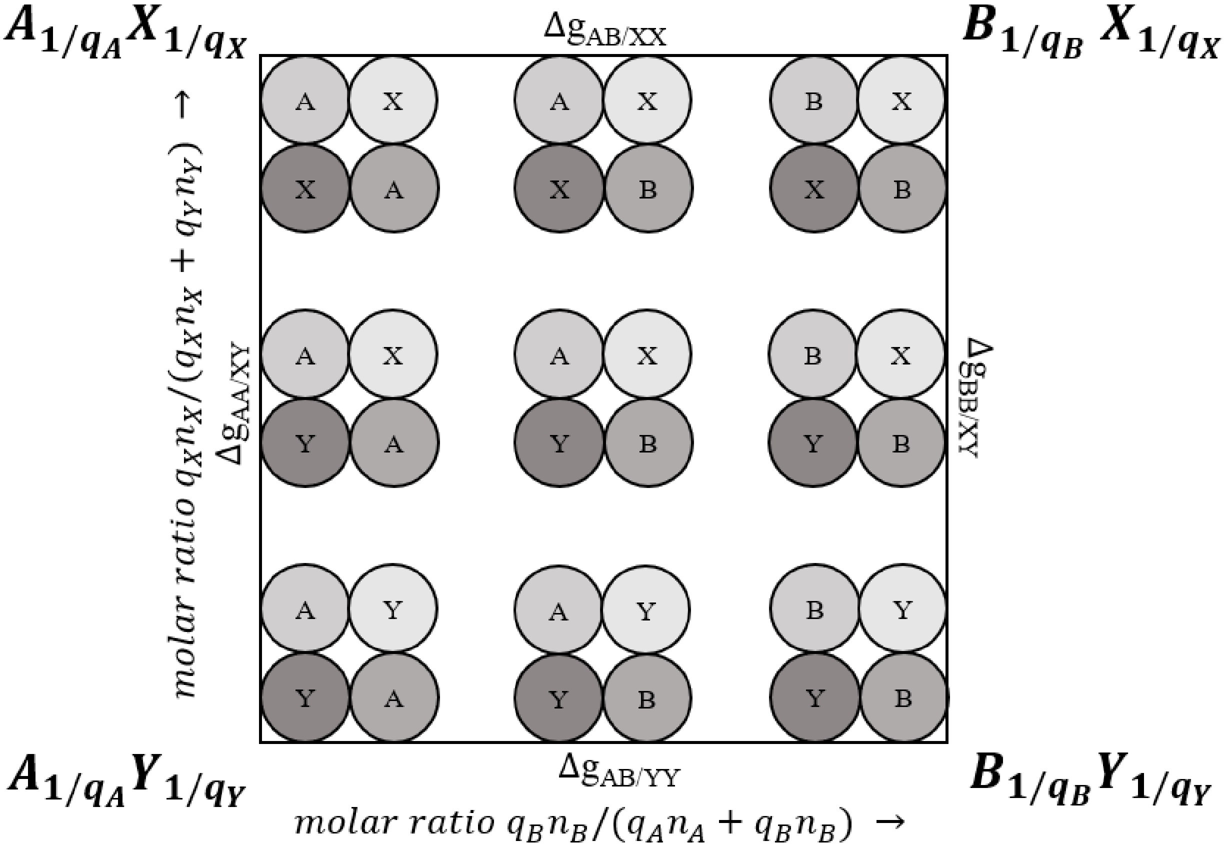

Figure 2.1 Schematic representation of the quadruplets in the A, B // X, Y melt.

Chapter 3. Key Phase Diagram Experiments and the Thermodynamic Optimizations of the Y_2O_3-YF_3 Binary Systems

The Chapter 3 covered the article which is published in Journal of European Ceramic Society as “ Phase diagram study and thermodynamic optimization of the Y_2O_3-YF_3 system” by Baek and Jung. [5]

3.1 Introduction

In the semiconductor manufacturing process, AlN is widely used as a ceramic heater material because it has similar thermal expansion properties to silicon wafer and is resistant to plasma etching. However, when it is exposed to a high temperature fluorocarbon plasma gas, AlN can react with fluorine radicals and ions to form aluminum fluoride (AlF_3) layer. Because AlF_3 sublimates and deposits on the inner wall of a plasma etching chamber, it becomes a source of contaminated particles in the process. Due to the stringent anti-contamination protocols of semiconductor production, this can cause serious problem in yield.[6, 7] In addition, the AlF_3 can damage AlN heater which leads to a decrease in its electrical and mechanical strength. To minimize the degradation of AlN heater during a plasma etching and cleaning process, Y_2O_3 coating has been adopted, but is known to be insufficient in high temperature high power plasma processes.[8] Consequently, $Y_xO_yF_z$ (YOF) layer coating has gained attention because yttrium oxyfluoride (YOF) may slow down the reaction with the fluorocarbon plasma gas.[9, 10] For example, Shiba et al.[11] reported that the surface crystallinity of YOF film was not changed by fluorine gas, while Y_2O_3 film was affected by fluoride penetration.

To understand the thermal stability and corrosion behavior of Y_2O_3 and YOF materials under fluorocarbon plasma gas atmosphere, accurate thermodynamic knowledge on the Y_2O_3-YF_3 system is essential. Despite its importance, the phase diagram and thermodynamic property data for the Y_2O_3-YF_3 system are very limited in the literature. Regarding the thermodynamic properties, the Gibbs energies of YOF [12], and vernier phases ($Y_4O_3F_6$, and $Y_7O_6F_9$) [13, 14] have been studied. However, the available data are quite inconsistent each other. The available phase diagram data are only limited in the YF_3 rich region. The melting temperatures of YOF and vernier phases, homogeneity ranges of solid phases, and liquidus in the binary system have never been studied.

As part of a long-term research project to search new ceramic heater and coating materials for high operation temperature, a consistent set of thermodynamic databases covering a wide range of oxy-carbide-nitride-fluoride systems is currently being developed. In the present study, the thermodynamic database for the Y_2O_3-YF_3 system was developed. Since no reliable phase diagram data are available, phase equilibrium experiments were conducted. Based on new experimental phase diagram data and critical evaluation of thermodynamic property data in the literature, the thermodynamic modeling of the binary Y_2O_3-YF_3 system was carried out using the CALculation of PHAse Diagram (CALPHAD) method. As applications of the thermodynamic database, the vaporization pressures of fluorides in the Y_2O_3-YF_3 system and metastable solubility of fluorine in solid Y_2O_3 phase were calculated. All thermodynamic calculations in the present study were performed using the FactSage^{TM} thermochemical software.[1, 15, 16]

3.2 Literature review of the Y_2O_3-YF_3 system

The most well determined intermediate compound in the Y_2O_3-YF_3 system is a stoichiometric YOF oxyfluoride phase. X-ray diffraction and electron microscopy were used to characterize the accurate structure of YOF, and it was concluded that it has a rhombohedral crystal structure (pseudo cubic fluorite structure) at room temperature.[17-20] Differential thermal analysis (DTA) was employed to determine the polymorphic transition of YOF from rhombohedral to cubic structure at 833-843 K.[21, 22] The other intermediate phases in the Y_2O_3-YF_3 system are vernier phases, $Y_xO_{x-1}Y_{x+2}$ ($4 \leq x \leq 7$~8), in which several compounds are densely present. According to Mann et al.[23, 24], the structure of vernier phases are in forms of one-dimensional intergrowth of orthorhombic unit cell. More recently, Skolis et al.[14] studied the composition range of vernier phases by measuring electromotive force at 1150-1350 K and reported that vernier phases existed at 62 to 67 mol % of YF_3, which corresponds to $Y_7O_6F_9$ and $Y_4O_3F_6$ composition. Sobolev et al.[25] investigated phase relations in the YF_3 rich region ($YF_3 \geq 94$ mol %) using thermal analysis technique, and reported the eutectic reaction between YF_3 solid solution and vernier phase at 1401 K. No phase diagram study has been performed above 1450 K. Melting temperatures of YOF and vernier phases are unknown, and no liquidus information in the YF_3 rich region has been reported except the eutectic reaction between vernier phase and YF_3. In summary, the phase diagram information of the Y_2O_3-YF_3 system is still quite scarce.

Thermodynamic properties of YOF and vernier phases were studied by the electromotive force (emf) method. Levitskii and Balak [12] determined the Gibbs energy of YOF phase using two different cell configurations with a CaF_2 electrolyte. Vintonyak et al.[13] investigated the Gibbs energies of reactions involving vernier phases ($Y_4O_3F_6$ and $Y_7O_6F_9$) using a CaF_2 electrolyte, and derived the Gibbs energies of vernier phases based on the reported Gibbs energy data of YOF by Levitskii and Balak.[12] Similarly, Skolis and Pashina [14] investigated the Gibbs energies of YOF, and vernier phases using emf technique. However, due to the complexities of the emf cell configurations used in the experiments [13, 14] the accuracy of the reported thermodynamic data of vernier phases are highly dependent on the assumed chemical reactions and the Gibbs energy of YOF phase. This will be discussed later in section 5.3.

3.3 Phase diagram experiments

3.3.1 Starting materials

Starting materials were made of mechanical mixtures of pure Y_2O_3 (Sigma Aldrich; 99 wt.% purity), and YF_3 (Alfa Aesar; >99.99 wt.% purity) powders. The commercial YOF powders (IONES, Korea) were also used in the preparation of starting materials. The purities of all the powders were checked by Bruker D8 Advance multi-purpose XRD analyses in the Research Institute of Advanced Materials (RIAM) at Seoul National University (SNU). The starting mixtures were then stored in C_6H_{12} cyclohexane to prevent moisture pick-up and were dried in vacuum at 348 K before their usages.

The dried starting materials were put in sealed Pt capsules in air condition for the annealing experiments at high temperatures and differential thermal analysis (DTA) experiments. The sealed Pt crucibles can prevent the vaporization loss of YF_3 during high temperature annealing process. The Pt crucibles were made from Pt tube with 3.3 mm outer diameter, 0.3 mm wall thickness and about 10 mm in length. Each capsule contained about 15~20 mg of starting material mixture.

3.3.2 Differential thermal analysis (DTA)

DTA experiments were performed using the NETSCH STA 449 F5 equipment. Temperature calibrations were conducted using many standard materials such as Ag_2SO_4, $BaCO_3$, $C_7H_6O_2$, $C_{12}H_{10}$, CsCl, $CaMgSi_2O_6$, K_2CrO_4, $KClO_4$, and $RbNO_3$. A sealed Pt capsule containing sample was placed inside DTA alumina crucible for the thermal analysis. The samples were heated and cooled at 10 K/min in an argon atmosphere with 20 mL/min flow rate. Two cycles of heating and cooling analysis were typically performed for each sample. Thermo-gravity analysis (TGA) was also carried out simultaneously to confirm no weight loss by evaporation.

3.3.3 Quenching experiments

Quenching experiments were conducted in a vertical tube furnace equipped with $Pt_{30}Rh$-Pt_6Rh (type B) thermocouples. The furnace temperature was maintained within ± 3 K at the target temperature using a PID controller. The sealed Pt capsules containing samples were hanged in an alumina tube using a Pt wire and annealed at target temperature. Then, the samples were dropped and quenched in cold water. After the quenching experiments, weight change of Pt capsule was checked to confirm no evaporation loss or hydration of the samples in water quenching process. Chemical equilibration was ascertained by the homogeneity in each phase composition throughout the quenched sample. Only the samples with no bursting of the Pt capsule were used in the present study.

3.3.4 Phase Characterization

After the quenching experiments, the samples were cast in epoxy and polished using a diamond-based lapping oil as the polishing media to avoid any moisture pick-up. After, the samples were cleaned in an ultrasonic bath of cyclohexane and then carbon coated. Phase characterization was conducted by JEOL-8530F electron probe microanalysis (EPMA) in the National Center for Inter-university Research Facilities (NCIRF) at SNU. The EPMA phase composition analysis was performed using 15 kV accelerating voltage and 10 nA beam current. Beam diameters (1~3 μm) were set according to the size of each phase. YOF sample (annealed at 1973 K for 1 hr; sample #1 in Table 3.1) was employed in this study as an internal standard for the elemental compositions of Y, O and F. Phases in ground samples were also identified by XRD (Bruker D8 Advance) method with Cu-Kα source (λ = 1.54 Å). All peaks of the XRD scan were identified with powder diffraction files (PDF) from the International Center for Diffraction Data using Bruker AXS DIFFRAC.EVA software.

3.4 Thermodynamic models

3.4.1 Stoichiometric compounds

The Gibbs energy of a stoichiometric compound can be expressed as below:

$$G_T^o = H_T^o - TS_T^o \quad (1)$$

$$H_T^o = \Delta H_{298.15\,K}^o + \int_{298.15\,K}^{T} C_p dT \quad (2)$$

$$S_T^o = S_{298.15\,K}^o + \int_{298.15K}^{T} \frac{C_p}{T} dT \quad (3)$$

in which $\Delta H^{o}_{298.15\,K}$ is the standard enthalpy of formation of a compound at 298.15 K, $S^{o}_{298.15\,K}$ is the standard entropy at 298.15 K, and C_p is the heat capacity of a compound which is a function of temperature.

The Gibbs energies of solid cubic, hexagonal, and liquid Y_2O_3 were taken from the previous study of rare earth sesquioxides by our group.[26] The Gibbs energies of solid orthorhombic, hexagonal and liquid YF_3 were taken from the FactSage FactPS database [1, 15, 16], originated from the thermodynamic data compilation by Barin.[27] The Gibbs energies of YOF and vernier phases were optimized in the present study.

3.4.2 Liquid solution

The Modified Quasichemical Model (MQM) [2], which takes into account the short-range ordering of the second-nearest neighbors of anions in a molten yttrium oxy-fluoride solution, was used to describe the liquid solution. According to MQM, the quasi-chemical reaction in the Y_2O_3-YF_3 melt can be expressed as

$$(O-O)+(F-F)=2(O-F);\ \Delta g_{OF} \qquad (4)$$

where $(i-j)$ describes a pair of two anions sharing a common yttrium cation, $(i-\mathrm{Y}-j)$. Δg_{OF} is the Gibbs energy of the above pair-exchange reaction. It can be described with functions of temperature and pair fractions as:

$$\Delta g_{OF} = \Delta g_{OF}^{o} + \sum_{i\geq 1} g_{OF}^{i0} X_{OO}^{i} + \sum_{j\geq 1} g_{OF}^{0j} X_{FF}^{j} \quad (5)$$

in which X_{ij} is a pair fraction of $(i-j)$ pair, and Δg_{OF}^{o}, g_{OF}^{i0}, and g_{OF}^{0j} are the model parameters which can be functions of temperature. The parameters can be optimized to reproduce the phase diagram data.

The Gibbs energy of the binary liquid solution can be expressed as

$$G^{m} = \left(n_{Y_2O_3} G_{Y_2O_3}^{o} + n_{YF_3} G_{YF_3}^{o}\right) - T\Delta S^{conf} + \frac{n_{OF}}{2} \Delta g_{OF} \quad (6)$$

In Equation (6), n_i and G_i^{o} are the number of moles and molar Gibbs energy of the constituent i, respectively. n_{ij} is the moles of $(i-j)$ pair existing at the equilibrium. ΔS^{conf} is the configurational entropy which considers the short-range ordering by the random arrangement of the pairs. It should be noted that the ΔS^{conf} in the MQM is a function of Δg_{OF}.

In the MQM, the coordination number of each cation and anion is also assigned to represent the structure of melt. In the present study, the coordination numbers of Y^{3+}, O^{2-} and F^{-} were set to be 2.066, 1.377, and 0.689, respectively, to keep the consistency with the previous study. [28] The details of the MQM can be found elsewhere.[2]

3.4.3 Solid solutions

The solid solutions that have been confirmed in the present experimental study are cubic-

Y_2O_3 and hexagonal-YF_3 solid solutions. Considering the existence of a cubic-Y_2O_3 solution, a hexagonal-Y_2O_3 solution above 2600 K was also assumed.

3.4.3.1 Cubic-Y_2O_3 and hexagonal-Y_2O_3 solutions

As no structure information how YF_3 dissolves in Y_2O_3 crystal has been known, it is rather arbitrary to model the Y_2O_3 solution. For example, we can simply treat the solution using a random mixing model of $YO_{1.5}$ and YF_3, or describe it by introducing more specific sublattice structure, if necessary, including vacancy. As depicted in Figure 3.1, the unit cell of Y_2O_3 cubic bixbyite structure has two Y atoms in the center of cubic cells (8b and 24d), 12 oxygen atoms on the corners (‘a’ sites for oxygen), and 4 vacancies (Va) on the corners (‘b’ sites for vacancy).[29] When YF_3 dissolves in Y_2O_3, it can be assumed that F enters both oxygen and vacancy sites by replacing O and Va. Then, we could assume the Y_2O_3 solid solution to be $(Y^{3+})_2[O^{2-},F^-]_3^a[Va,F^-]_1^b$ where a and b represent oxygen and vacancy sites, respectively. Three sublattice Compound Energy Formalism (CEF) is then used to describe the Gibbs energy of the Y_2O_3 solid solution:

$$G^m = y_O^a y_{Va}^b G^o_{Y_2O_3Va_1(0)} + y_O^a y_F^b G^o_{Y_2O_3F_1(1-)} + y_F^a y_{Va}^b G^o_{Y_2F_3Va_1(3+)} + y_F^a y_F^b G^o_{Y_2F_3F_1(2+)} + 3RT(y_O^a ln y_O^a + y_F^a ln y_F^a) + RT\left(y_{Va}^b ln y_{Va}^b + y_F^b ln y_F^b\right) + g^{ex} \quad (7)$$

where y_i^a and y_i^b are site fractions of i in ‘a’ and ‘b’ anion sites, respectively, and g^{ex} is excess interaction parameter between species in anion sites. The main parameters of the model are the Gibbs energies of hypothetical end-members, $G^o_{Y_2i_3j_1}$. In the present study, the Gibbs energy of $Y_2F_3Va_1(3+)$ was set to equal to the sum of the molar Gibbs energies of metallic Y and h-YF_3. Then, it was possible to determine the Gibbs energy of $\mathrm{Y_2O_3F_1(1-)}$ and $\mathrm{Y_2F_3F_1(2+)}$ considering the charge neutrality to form YOF and reciprocal relation as below:

$$2G^{o}_{YOF} = \frac{2}{3}G^{o}_{\mathrm{Y_2O_3F_1(1-)}} + \frac{1}{3}G^{o}_{\mathrm{Y_2F_3F_1(2+)}} + 3RT\left(\frac{2}{3}ln\frac{2}{3} + \frac{1}{3}ln\frac{1}{3}\right) \qquad (8)$$

$$G^{o}_{Y_2O_3Va_1(0)} + G^{o}_{\mathrm{Y_2F_3F_1(2+)}} = G^{o}_{\mathrm{Y_2O_3F_1(1-)}} + G^{o}_{Y_2F_3Va_1(3+)} \qquad (9)$$

The Gibbs energy of $\mathrm{Y_2O_3Va_1(0)}$ end-member in Y_2O_3 structure, $G^{o}_{Y_2O_3Va_1(0)}$, is $G^{o}_{Y_2O_3(s)}$ and that of YOF, G^{o}_{YOF}, is a model parameter which can be determined to be G^{o}_{YOF} = $G^{o}_{YOF(s)}$ + (a + bT).

In order to reproduce the solubility of YF_3 in solid cubic-Y_2O_3, in the present study, G^{o}_{YOF} was optimized and no g^{ex} parameter was necessary. Similar parameters were taken for the hexagonal-Y_2O_3 solution because of no experimental data are available.

3.4.3.2 Hexagonal-YF_3 solution

There is a small solubility of Y_2O_3 in solid hexagonal-YF_3 (h-YF_3), but the dissolution mechanism is not well known. It might be possible to use a solid solution structure like $(Y^{3+})[F^-, O^{2-}, Va]_3$ for YF_3 solid solution. However, because it was found that a thermodynamic model with this solid solution structure overestimated the configurational entropy of YF_3 solid solution, it required an excess interaction parameter containing temperature dependent term of as large as about +600 T (J/mol) in order to reproduce the Y_2O_3 solubility in YF_3 solution and eutectic temperature involving YF_3 phase. This will be discussed later in section 5.3. Therefore, in the present study, one sublattice random mixing model was used for h-YF_3 solution considering YF_3 and $YO_{1.5}$ as a solution species to reduce the mixing entropy of the solution. That is, the Gibbs energy of hexagonal-YF_3 solid solution is described by:

$$G^m = X_{YF_3} G^o_{YF_3(H)} + X_{YO_{1.5}} G^o_{YO_{1.5}(H)} + RT\left(X_{YF_3} lnX_{YF_3} + X_{YO_{1.5}} lnX_{YO_{1.5}}\right) + \sum_i \sum_j q^{ij}_{YF_3:YO_{1.5}} (X_{YF_3})^i (X_{YO_{1.5}})^j \qquad (10)$$

in which $G^o_{YF_3(H)}$ and $G^o_{YO_{1.5}(H)}$ are the molar Gibbs energy of h-YF_3, and hypothetical $YO_{1.5}$ with h-YF_3 crystal structure. In the present study, $G^o_{YO_{1.5}(H)}$ and $q^{ij}_{YF_3:YO_{1.5}}$ were optimized to describe the solution.

3.5 Experimental results and thermodynamic optimization

Figure 3.2 shows the optimized calculated phase diagram of the Y_2O_3-YF_3 system along with the present experimental data. All the phase diagram experimental results in the present study are summarized in Tables 3.1 and 3.2. The Gibbs energies of all the compounds and model parameters of solutions in the Y_2O_3-YF_3 system are summarized in Tables 3.3 and 3.4, respectively.

3.5.1 Yttria phases (c-Y_2O_3, and h-Y_2O_3) and Yttrium oxyfluoride (YOF)

Yttrium oxyfluoride (YOF) sample was annealed at 1973 K for 1 hr, and its microstructure is presented in Figure 3.3 (a). From the EPMA results of 20 random points, an uniform composition of YOF phase (50.20 ± 0.4 mol % YF_3) was confirmed. The microstructure of the YOF powder showed very slow sintering process at 1973 K, which means that the melting of YOF would be much higher than 1973 K. Unfortunately, because the maximum furnace temperature we could employ in the present study was 1973 K, the higher temperature experiments could not be carried out. However, from the liquidus determined in the YF_3 rich region, the melting temperature of YOF phase could be estimated to be 2829 K, as shown in Figure 3.2. Sample #1 was analyzed by DTA to measure the polymorphic transition temperature of YOF. As shown in Figure 3.3 (b), the transition was recorded at 846 K which is similar to 833 and 843 K reported in the previous studies. [21, 22]

Yttria has two polymorphs stable at 1 atm total pressure. Cubic Y_2O_3 (c-Y_2O_3) is stable at room temperature, and it changes to hexagonal Y_2O_3 (h-Y_2O_3) at 2600 K. Then, melting occurs at 2703 K [26]. In order to determine the solubility of YF_3 to Y_2O_3, several samples containing Y_2O_3 and YOF were annealed at 1773 to 1923 K for 24 hr to168 hr (see the samples #2 to #5). For example, the BSE image by EPMA of the sample #4 annealed at 1923 K are presented in Figure 3.4 (a). The melting temperatures of both Y_2O_3 and YOF phase are above 2700 K, no large crystals were grown during the solid state sintering even at 1923 K for 168 hr. Under the BSE mode, the brightness between Y_2O_3 and YOF phase was less distinguishable, so that it was rather hard to directly identify two phases. Therefore, EPMA compositional mappings were also carried out to identify the phases. The exact compositions of Y_2O_3 and YOF phase were detected by EPMA with 1~3 μm beam diameter.

In general, the solubility of YF_3 in Y_2O_3 are consistent in the samples #2 to #5, while the composition of YOF varied a lot with a large scatter. In the case of sample #4 annealed at 1923 K for 168 hr, for example, the solubility of YF_3 in Y_2O_3 phase was consistently 5.76 ± 1.38 mol %. The solubility of Y_2O_3 in YOF phase varied largely depending on temperature and annealing time. In fact, EPMA compositional mapping results showed that the size of YOF was rather too small to analyze its composition accurately, and the EPMA point analyses of YOF were always interrupted by the surrounding Y_2O_3 phase. XRD phase analyses confirmed that the samples between Y_2O_3 and YOF were composed of only Y_2O_3 and YOF phase. Therefore, considering the uncertainty in the composition analysis, YOF phase was treated in this study as a stoichiometric compound.

3.5.2 Vernier phases and Yttrium oxyfluoride (YF_3)

Skolis et al.[14] reported that there are many vernier phases existing at composition between 62 and 67 mol % of YF_3 ($Y_xO_{x-1}Y_{x+2}$, $4 \leq x \leq 7$). However, their decomposition temperatures have not been investigated. As an attempt to determine the decomposition (melting) temperatures of vernier phases and liquidus composition in the YF_3 rich region, samples with mixture of YF_3 and YOF were prepared and annealed at 1373 K to 1973 K (samples #7 to #9). The BSE images of several key samples are presented in Figure 3.4. Sample of 0.6 mol fraction YF_3 (sample #6) was annealed at 1873 K for 2 hr and a large crystal of $Y_7O_6F_9$ was synthesized, as shown in Figure 3.4 (b). The composition of the $Y_7O_6F_9$ crystalline phase was confirmed by both EPMA and XRD analysis. Figures 3.4 (c) and (d) show the quenched microstructures of the samples with 0.7 mol fraction YF_3 annealed at 1523 K (sample #7) and 0.8 mol fraction YF_3 annealed at 1423 K (sample #11). In both samples, an assemblage of liquid and $Y_4O_3F_6$ phase was observed, which means the composition range of vernier phases are less than 0.7 mol fraction YF_3. XRD analysis confirmed the existence of $Y_4O_3F_6$ phase. The vernier phases in the YF_3 rich region determined in the present study agrees well with the result of Skolis et al.[14] No attempt was made in the present study to determine the stoichiometries of all vernier phases between $Y_7O_6F_9$ and $Y_4O_3F_6$.

Samples of 0.75 mol fraction YF_3 (samples #8 and 9) were annealed at 1923 K and 1973 K. As can be seen in Figure 3.4 (e) for sample #9 annealed at 1973 K, the quenched microstructure shows large $Y_4O_3F_6$ crystals surrounded by liquid phase. That is, the decomposition temperature of $Y_4O_3F_6$ compound should be higher than 1973 K. The liquidus composition of $Y_4O_3F_6$ at 1973 K (sample #9) was 94.1 ± 5.9 mol % YF_3. The large scatters in liquid composition can be easily understood due to a quenched crystal formation in liquid phase during quenching process. The concentrations of YF_3 in liquid phase in equilibrium with $Y_4O_3F_6$ phase at 1523 K (sample #7) and 1423 K (sample #11) were 96.9 ± 3.2 and 98.4 ± 3.3 mol %, respectively. In order to determine the liquidus composition of $Y_4O_3F_6$ more accurately, a large amount of liquid phase in the quenched sample would be more ideal. Therefore, the sample with 0.9 mol fraction YF_3 was prepared and annealed at 1773 K (sample #13), and the liquid composition was determined to be 97.2 ± 1.1 mol % YF_3. These liquidus data are consistent each other. As shown in Figure 3.2, a very steep liquidus of $Y_4O_3F_6$ phase was confirmed in the present experiments.

Orthorhombic-YF_3 (*o*-YF_3) stable at room temperature transforms to hexagonal form (*h*-YF_3) at 1350 K, and melts at 1428 K [10-12]. Sobolev et al. [25] performed the thermal analysis experiments in the composition range between 94 and 100 mol % YF_3, and reported the eutectoid and eutectic reactions between vernier phase and *h*-YF_3 solid solution at 1328 K and 1401 K, respectively. They also found another thermal peaks (at about 1368 K) between thsese invariant reactions, but could not identify them properly. In order to re-investigate these invariant reactions, DTA experiments were performed for the samples with 75, 80 and 95 mol % YF_3, and the results are plotted in Figure 3.5. As can be seen in the DTA curves, the transition temperatures in heating and cooling cycles were rather largely different. In the present study, the transitions recorded in the heating curves were adopted because of a possible supercooling of the samples in the cooling process. Considering that the starting materials were the mixtures of YOF and YF_3, the results obtained in the second heating curves were more weighted. In the sample with 75 mol % YF_3, transitions were recorded at 1330, 1376 and 1394 K, while the transitions in the 80 mol % YF_3 sample were 1327, 1372 and 1390 K and the transitions in the 95 mol % YF_3 sample were 1330, 1377 and 1397 K, respectively. It should be noted that transitions at 1327-1330 K in all samples were very intensive. The transition peak at 1390-1397 K was also strong in all samples, although the one in 75 and 80 mol % YF_3 samples was superimposed by another peak. The prolonged peaks at 1327-1330 K and 1390-1397 K over about 10 K (a broad peak rather than a sharp peak) could happen because of the nature of YF_3 solid solution phase. Because the phase transition involving solid solution can happen within a certain range of temperatures rather than a discrete temperature, the thermal peak recorded in DTA can be rather broadened. The transitions at 1327-1330 K and 1390-1397 K were identified as the eutectoid and eutectic reactions based on the transition of pure YF_3 phase and equilibration results of samples #10 and 12 explained below. The present results are consistent with the reports by Sobolev et al.[25] The middle peak at 1372-1375 K, similar to the unidentified transition by Sobolev et al.[25] at 1368 K, was strong in 75 and 80 mol % YF_3 samples but weak at 95 mol % YF_3 sample, which indicated that this transition would be related to $Y_4O_3F_6$ vernier phase. No phase transition was reported for $Y_4O_3F_6$ vernier phase previously.

In order to determine the homogeneity range of *h*-YF_3 solid solution, two samples with 0.8 and 0.9 mol fraction YF_3 (samples #10 and #12, respectively) were annealed at 1373 K for 24 hr, and the BSE images of the quenched samples are presented in Figures 3.6 (a) and (b). In the sample #10, both $Y_4O_3F_6$ and YF_3 phase were identified. The composition of *h*-YF_3 phase was 97.8 ± 7.1 mol % YF_3, of which scatters would result from the counts of background $Y_4O_3F_6$ phase because of a small area of YF_3 phase. In the sample #12, a large grain of YF_3 phase was developed. It was difficult to find $Y_4O_3F_6$ phase on the EPMA sample surface (this could happen because of a small phase fraction of $Y_4O_3F_6$ phase), but XRD analysis confirmed the existence of both $Y_4O_3F_6$ and YF_3 phases in sample #12. The composition of YF_3 was analyzed more accurately to be 96.7 ± 1.6 mol % YF_3 in sample #12. That is, the solubility of Y_2O_3 in *h*-YF_3 solid solution was determined to be 3.3 ± 1.6 mol %. The present result is similar to that of Sobolev et al.[25] (less than 2 mol %, indirectly estimated from their DTA results).

Solubility of Y_2O_3 in *o*-YF_3 was reported to be zero in the previous study by Sobolev et al.[25] based on their DTA results, so no attempt was made to determine the homogeneity range of *o*-YF_3 in the present study.

3.5.3 Thermodynamic optimization of the Y_2O_3-YF_3 system

YOF and two vernier phases ($Y_7O_6F_9$ and $Y_4O_3F_6$) were considered as intermediate stoichiometric compounds in the present Y_2O_3-YF_3 system. In reality, there seems to be at least 4 stoichiometric compounds in the vernier phase region, $Y_xO_{x-1}Y_{x+2}$, $4 \leq x \leq 7$. But only $Y_7O_6F_9$ and $Y_4O_3F_6$ were considered in the present study because their thermodynamic properties have been studied [13, 14] and they represent the boundary compositions of vernier phases. Solid Y_2O_3 phases (*c*- and *h*-Y_2O_3) were considered to have limited solubilities of YF_3. Solid *h*-YF_3 phase (high temperature hexagonal YF_3) was also considered to form a narrow solid solution by dissolving Y_2O_3, while *o*-YF_3 phase (low temperature orthorhombic YF_3) was treated as a stoichiometric compound. For the accurate thermodynamic description of the Y_2O_3-YF_3 system, the thermodynamic properties of YOF phase and vernier phases were optimized. Then, based on the phase diagram experimental data in the present study, the thermodynamic modelings of all other phases including liquid solution were performed. The optimized phase diagram of the Y_2O_3-YF_3 system along with the experimental data is presented in Figure 3.2.

Levitskii and Balak [12] performed the emf measurement for the $Y_{2-x}O_{3-3x}F_{3x}$ (x = 0.1 ~ 0.48) samples using the following two cell configurations at 960-1465 K:

Cell-A: (-) O_2, Pt | CaO, CaF_2 || CaF_2 || $Y_{2-x}O_{3-3x}F_{3x}$ | Pt, O_2 (+)
Cell-B: (-) O_2, Pt | $Y_{2-x}O_{3-3x}F_{3x}$ || CaF_2 || $CaZrO_3$, $(CaO)_{0.18}(ZrO_2)_{0.82}$, CaF_2 | Pt, O_2 (+)

The samples of $Y_{2-x}O_{3-3x}F_{3x}$ (x = 0.1 ~ 0.48) should be all ‘Y_2O_3+YOF’ mixtures. In both cells, oxygen partial pressures were fixed at 10^{-5} Pa and $1\sim10^2$ Pa. The difference of F_2 partial pressures were measured by emf technique to determine the Gibbs energy of YOF phase. In the analysis of the Cell-B, the emf results of their former study [30] on the equilibration of ‘CaO+$CaZrO_3$+$(CaO)_{0.18}(ZrO_2)_{0.82}$’ were used. It should be noted that the emf values for all

$Y_{2-x}O_{3-3x}F_{3x}$ samples were the same regardless of sample compositions, but varied with temperature. Although Levitskii and Balak [12] mentioned that both cells gave almost identical results for the following reaction, we preferred to use only Cell-A data because the $(CaO)_{0.18}(ZrO_2)_{0.82}$ solid solution in Cell-B can be transformed to ZrO_2 solid solution + $CaZrO_3$ phase at 1320 K [31] :

$$2YOF(s) + CaO(s) = Y_2O_3(s) + CaF_2(s) \tag{11}$$

$$\Delta G_T^o = (-66{,}459 \pm 1{,}949) + (21.748 \pm 1.563) * \mathrm{T}\ (\mathrm{J/mol}) \tag{12}$$

According to the present phase diagram data, the solubility of YF_3 in Y_2O_3 is less than 2.5 mol % at the experimental temperatures of Levitskii and Balak [12], which can be ignored in the analysis (Even it is considered, it would change the entropy term of Eq. (12) by maximum about +0.2 J/mol-K by assuming the ideal solution of Y_2O_3). Considering the Gibbs energies of pure CaO, CaF_2, Y_2O_3, and YF_3 used in the present study [15, 16, 26], the Gibbs energy for the formation of YOF were re-calculated in the temperature range between 960 and 1465 K in order to keep the internal consistency:

$$1/3\ Y_2O_3(s) + 1/3\ YF_3(s) = YOF(s) \tag{13}$$

$$\Delta G_T^o = -(10{,}098 \pm 974) - (14.979 \pm 0.781) * T\ (\mathrm{J/mol}) \text{ at 960-1465K} \tag{14}$$

Considering that the Cell-B also requires the same conversion as Cell-A, the final Gibbs energy of formation of YOF from the Cell-B should be similar to that of the Cell-A in Eq. (12). It should be noted that the Gibbs energy of YOF phase derived in the present study (see Eq. (14)) is more negative than the value by Levitskii and Balak [12], which would result from the difference in the standard Gibbs energies of CaO, CaF_2, Y_2O_3 and YF_3 used in the conversion.

A similar emf study was performed by Skolis and Pashina [14] to determine the Gibbs energy of YOF phase. They employed the emf cell of 'O_2, Pt | Y_2O_3, YOF || CaF_2 || YOF, $Ca_{0.9}Y_{0.1}O_{2.1}$ | Pt, O_2' and from the emf value for the reaction involving the equilibration of two solid solutions '$Ca_{0.9}Y_{0.1}F_{2.1}$ + $Y_{0.18}Zr_{0.91}O_{2.09}$', they derived the Gibbs energy of formation of YOF, $\Delta G_T^o = -0.4 - 19.5\,T$ (J/mol), which is about 4 to 5 kJ/mol more positive than the values in Eq.(14) at the experimental temperature of 1150-1350 K. Unfortunately, as no thermodynamic data for $Ca_{0.9}Y_{0.1}F_{2.1}$ and $Y_{0.18}Zr_{0.91}O_{2.09}$ solid solutions are available and their thermodynamic reactions could change the emf values, it is hard to evaluate the accuracy of the experimental results by Skolis and Pashina.[14]

Considering that YOF phase is very stable to high temperature, we can easily expect that the enthalpy of formation of YOF from Y_2O_3 and YF_3 be a quite negative. In addition, because the emf reaction by Levitskii and Balak [12] is more straightforward, compared to that of Skolis and Pashina [14], less error could be involved in the analysis of the experimental data of Levitskii and Balak. Therefore, the Gibbs energy data of YOF by Levitskii and Balak (re-calculated in Eq. (14)) was considered in the present optimization to be more accurate than the result of Skolis and Pashina.

Vintonyak et al.[13] performed the emf experiments for vernier phases, $(Y_2O_3)_{0.41}(YF_3)_{0.59}$ and $(Y_2O_3)_{0.35}(YF_3)_{0.65}$ using a CaF_2 electrolyte. To calculate the Gibbs energy of vernier phases, that of YOF by Levitskii and Balak [12] was used. In the present study, the Gibbs energies of $(Y_2O_3)_{0.41}(YF_3)_{0.59}$ and $(Y_2O_3)_{0.35}(YF_3)_{0.65}$ were re-calculated based on the optimized Gibbs energy of YOF above in Eq. (14). Skolis and Pashina [14] also performed the emf measurement for the vernier phases $Y_7O_6F_9$ and $Y_4O_3F_6$ similar to the work by Vintonyak et al.[13] In the derivation of the Gibbs energies of vernier phases, the Gibbs energy of YOF was required. Based on the new optimized data of YOF in Eq. (14), the results of Skolis and Pashina [14] were also re-calculated in the present study.

All the thermodynamic data for the formation of YOF and vernier phases from Y_2O_3 and YF_3 by Levitskii and Balak [12], Vintonyak et al.[13], and Skolis and Pashina [14] are plotted in Figure 3.7. Both the original Gibbs energy data in the literature and the re-evaluated data in the present study for YOF phase are presented in Figure 3.7 (a) for the comparison purpose. The Gibbs energy of formation of YOF calculated in the present study well reproduces the re-evaluated experimental data of Levitskii and Balak [12]. Because of no heat capacity data available for YOF and $Y_7O_6F_9$ and $Y_4O_3F_6$ vernier phases, the Neumann-Kopp rule [32] was used to obtain their heat capacities from those of cubic-Y_2O_3 and orthorhombic-YF_3. The optimized $\Delta H^o_{298.15K}$ and $S^o_{298.15K}$ of YOF phase in this study are also compared in Figures 3.7 (b) and (c) with the re-evaluated experimental data of Levitskii and Balak. The optimized enthalpy and entropy of formation for 1 mol of YOF are -11.07 kJ/mol and 14.2 J/mol, respectively. It should be noted that the values at 0.5 mol fraction of YF_3 in Figures 3.7 (b) and (c) are corresponding to 1.5 mol of YOF. The formation enthalpies and entropies of $Y_7O_6F_9$ and $Y_4O_3F_6$ vernier phases are more scattered as can be seen in Figure 3.7 (b) and (c). The experimental data plotted in the figures are re-evaluated data using the Gibbs energy of YOF in Eq. (14), as mentioned above.

In the present study, $\Delta H^{o}_{298.15K}$ and $S^{o}_{298.15K}$ of vernier phases were optimized considering those of YOF phase and phase diagram data. That is, both $\Delta H^{o}_{298.15K}$ and $S^{o}_{298.15K}$ of vernier phases were set to be similar values as those of YOF phase and adjusted to make sure that both vernier phases were stable from room temperature to above 1973 K. YOF phase has phase transition from low temperature rhombohedral form to high temperature cubic form at 846 K. The emf experimental data of YOF phase in Figure 3.7 are for high temperature cubic-YOF phase. As no direct thermodynamic data for the rhombohedral-YOF phase have been determined, the transition enthalpy of YOF phase from rhombohedral to cubic structure at 846 K was arbitrary assumed to be 5 kJ/mol, and Cp of rhombohedral YOF phase was assumed to be the same as that of cubic-YOF phase in the present thermodynamic optimization. Then, $\Delta H^{o}_{298.15K}$ and $S^{o}_{298.15K}$ of rhombohedral-YOF phase could be determined from the optimized data of cubic-YOF phase. As observed in the present DTA results, $Y_4O_3F_6$ vernier phase shows phase transition at 1371 K. Considering the transition temperature, we could tell that the emf data for $Y_4O_3F_6$ phase in the literature [13, 14] were mostly for low temperature form of $Y_4O_3F_6$. Therefore, the thermodynamic properties of high temperature form of $Y_4O_3F_6$ phase was evaluated by assuming the enthalpy of transition of 5 kJ/mol at 1371 K. The optimized thermodynamic properties of all intermediate phases are listed in Table 3.3.

Based on the phase diagram data in the present study, the thermodynamic model parameters for Y_2O_3 and YF_3 solid solutions were determined. As explained in section 4.3, the solid solution of cubic-Y_2O_3 was described using the CEF with $(Y)_2[O,F,]_3[Va,F]_1$ structure. After assuming $G^{o}_{Y_2F_3Va_1(3+)} = G^{o}_{Y(hcp)} + G^{o}_{YF_3(hexagonal)}$, the Gibbs energy of YOF in Y_2O_3 solution was determined in order to reproduce the present solubility data of YF_3 in Y_2O_3

solution at 1773-1923 K. No excess interaction parameter was introduced. Because no phase diagram data are available for hexagonal-Y_2O_3 solution stable above 2600 K, the same model parameters as those of cubic-Y_2O_3 solution were assumed for hexagonal-Y_2O_3 solution. As can be seen in the phase diagram, the model parameters can reproduce the experimental homogeneity range of cubic-Y_2O_3 solution well. The predicted solubility of YF_3 in Y_2O_3 increases with temperature and the maximum solubility is predicted to be 9.14 mol % at eutectic temperature of 2467 K.

The hexagonal YF_3 (*h*-YF_3) solid solution was rather difficult to describe in the present study. The melting temperature of pure hexagonal YF_3 is 1428 K. The eutectic temperature of L → *h*-YF_3 solid solution + HT_$Y_4O_3F_6$ was experimentally determined to be about 1398.5 ± 1.5 K, which is 29.5 K lower than the melting temperature of pure YF_3. The eutectoid reaction for *h*-YF_3 solid solution → *o*-YF_3 + LT_$Y_4O_3F_6$ was recorded at 1328.5 ± 1.5 K, which is also lower than the orthorhombic to hexagonal transition of pure YF_3 at 1350 K. From the thermodynamic viewpoint, this decrease in melting temperature of YF_3 solid solution indicates that the mixing entropy of YF_3 solution is similar to or lower than that of liquid solution. If the mixing entropy of solid solution is higher than that of liquid solution, in general, the melting temperature can increase with increasing of foreign species in solid solution. As discussed in section 4.3.2, therefore, a simple random mixing model with assumption of YF_3 and $YO_{1.5}$ species was employed to describe YF_3 solution rather than more complex solid solution structure involving vacancy. The optimized model parameters are listed in Table 3.4. The calculated solubility limit (1.178 mol % Y_2O_3) from the present model is similar to the experimental data, while the calculated eutectic and eutectoid temperature are about 11.5 K and 9.5 K, respectively, higher than the experimental data.

Liquid Y_2O_3-YF_3 solution was described by MQM. In general, the experimental liquidus data in the YF_3 rich region were used to estimate the melting temperate of YOF phase. Then, the MQM parameters were optimized to reproduce these liquidus data:

$$\Delta g_{OF} = -31690 + 30T - 18000\, x_{FF}^2 \text{ (J/mol)} \qquad (15)$$

A temperature dependent term in Δg_{OF}^o was necessary to reproduce the melting temperature of YOF phase, and a negative parameter of X_{FF}^2 was introduced to better reproduce the steep liquidus in the YF_3 rich region. The predicted melting temperature of YOF, $Y_7O_6F_9$, and $Y_4O_3F_6$ from the present thermodynamic modeling are 2829, 2303, and 2116 K, respectively. The eutectic temperature in the Y_2O_3 rich region is predicted to be 2467 K. All the predicted invariant reactions in the binary system are summarized in Table 3.5.

3.6 Chemical reaction of Y_2O_3 in plasma etching and cleaning process

AlN is a common material for ceramic heater in semiconductor industry. In the plasma etching and cleaning process, fluorine containing gas is typically applied. Fluorine gas can react with AlN to form AlF_3, which can damage AlN heater material and contaminate the chamber by evaporation. The vapor pressures of AlF_3 at 873, 923 and 973 K are calculated in Figure 3.8. In the calculations, thermodynamic data of solid and gas phases related to AlF_3 were taken from FactPS database [1, 15, 16, 33]. For example, the calculated vapor pressure of AlF_3 is about $10^{-6.57}$ atm at 923 K. In comparison, the vapor pressure of Y_2O_3-YF_3 system including YOF phase is also calculated in Figure 3.8. The vapor pressure of YOF in equilibrium with Y_2O_3 is calculated to be about $10^{-18.12}$ atm at 923 K, and that of YF_3 is about $10^{-14.04}$ atm at the same temperature. It becomes more volatile as the composition of fluoride increases in the Y_2O_3-YF_3 system, but is still much less volatile than AlF_3. Based on this simple thermodynamic equilibrium calculation result, it can be said that Y_2O_3 or YOF ceramic heater material can be much resistant than Al_2O_3 material to the chemical corrosion in the plasma etching and cleaning condition.

Several studies have carried out to compare the chemical reactions of Y_2O_3, YOF and YF_3 materials with fluorine containing gas [10, 11, 34], and degradation in the subsequent sputtering process [10, 34]. According to XPS analysis, it was shown that fluorine penetrated deeply into Y_2O_3 materials under various gas conditions (Ar-NF_3, Ar-CF_4, and Ar-CHF_3) relevant to plasma etching and cleaning process. But no significant change was observed for YOF materials under the same gas conditions. When the fluorine penetrated Y_2O_3 material was subsequently exposed in the sputtering process, its corrosion was much significant than YOF due to the evaporation of fluorine. So far, no exact mechanism of fluorine penetration to Y_2O_3 under F containing gas condition has been revealed.

In the present phase diagram study, we found that noticeable amount of YF_3 can dissolve into cubic-Y_2O_3 most probably due to its crystal structure. As mentioned in section 4.3.1, the cubic-Y_2O_3 has a bixbyite crystal structure which has many oxygen vacancy sites. In this study, $(Y^{3+})_2[O^{2-},F^-]_3\ [Va,F^-]_1$ structure was used to explain the dissolution of fluorine in Y_2O_3. In comparison, YOF has a fluorite structure which has no vacancy site and its stoichiometry is well kept in theY_2O_3-YF_3 system.

In order to simulate the fluorine dissolution in Y_2O_3 in plasma etching and cleaning process, thermodynamic calculations between Y_2O_3 and gas phase were conducted at 923 K. Figure 3.9 shows the calculated equilibrium composition changes of gas phases starting with 0.5Ar-0.5NF_3, 0.5Ar-0.5CF_4, and 0.5Ar-0.5CHF_3 in mol. As can be seen, except CF_4 gas species, NF_3 and CHF_3 gas species can be self-decomposed with increasing temperature:

$$NF_3 \rightarrow 1/2\ N_2 + 3/2\ F_2 \qquad (16)$$

$$CHF_3 \rightarrow HF + 1/9\ C_6F_6 + 1/3\ CF_4 \qquad (17)$$

These decomposed gas species can react with Y_2O_3 at the etching and cleaning processes. Although 923 K can be reasonably high temperature for chemical equilibration of gas phase, it would be still relatively low temperature for the equilibrium chemical reaction involving solid phase. Therefore, metastable reactions between solid Y_2O_3 and gas phase without forming other crystalline phases could happen. In order to simulate this metastable reaction, stable solid phases such as YOF, vernier phases, and YF_3 were suppressed in the present thermodynamic calculations and only the dissolution of fluorine into Y_2O_3 was allowed by the reaction with gas phase. In the full equilibrium condition, YOF phase can be formed after a certain amount of fluorine dissolution into Y_2O_3 phase. The calculated composition changes of solid Y_2O_3 after the reactions with Ar-NF_3, Ar-CF_4, and Ar-CHF_3 are presented in Figure 3.10.

When the gases are reacted with Y_2O_3, the following reactions can happen at the surface of Y_2O_3:

NF_3 containing gas: $0.5NF_3 + 1Y_2O_3(s) \rightarrow 0.75O_2 + 0.5YF_3\text{-}0.5Y_2O_3(s.s)$ (18)

CF_4 containing gas: $0.5CF_4 + 1Y_2O_3(s) \rightarrow 0.5CO_2 + 0.67YF_3\text{-}0.67Y_2O_3(s.s.)$ (19)

CHF_3 containing gas: $0.5CHF_3 + 1Y_2O_3(s) = 0.5CO + 0.25H_2 + 0.5YF_3\text{-}0.75Y_2O_3(s.s.)$ (20)

That is, oxygen atoms in Y_2O_3 are replaced by fluorine atoms in all the reactions because the Gibbs energy of YF_3 formation reaction is in general very negative. For example, the ΔG_f^o of the following reaction below 1000 K is:

$$Y_2O_3(s) + 3\ F_2(g) = 2\ YF_3(s) + 3/2\ O_2(g) \qquad (21)$$

$$\Delta G_f^o = -1{,}493{,}023 + 199.24T\ \text{(J/mol)} \qquad (22)$$

Regardless of the gas type, nearly all the F available from gas can be dissolved to Y_2O_3 due to very strong negative reaction Gibbs energy in Eq. (22). As shown in Figure 3.10, once the concentration of F in Y_2O_3 surface becomes high by the surface reaction with F containing gas phase, F diffusion can happen into Y_2O_3, which can explain the deep penetration of F in Y_2O_3. In order to mimic the diffusion of F into Y_2O_3, the amount of fluorine containing gas species (NF_3, CF_4, and CHF_4) was changed in the calculations. As can be seen in Figure 3.10, the amount of F (mol fraction of F, F/(O+F)) in Y_2O_3 decreases linearly with decreasing the partial pressure (mol fraction) of fluorine containing gas species, NF_3, CF_4, and CHF_3. This F dissolved in Y_2O_3 solid seems to physically weaken Y_2O_3, and cause more physical damage in the subsequent plasma deposition process [10, 34].

On the other hand, YOF is a stoichiometric compound which has no excess F solubility. Therefore, when YOF reacts with F containing gas phases, the surface layer of YOF will transform to the reaction product such as vernier phase ($Y_4O_3F_6$ and $Y_7O_6F_9$) or YF_3. Once this reaction product layer is formed, further direct chemical reaction between Y_2O_3 and gas phase will not happen and the chemical reaction will be controlled by the reaction between YOF and surface reaction product. This kind of solid interfacial reaction can be very slow at temperature below 1000 K. In the deposition condition, thin surface reaction product layer could be broken. In general, therefore, the corrosion of YOF can be less significant than that of Y_2O_3 in a plasma deposition-etching-cleaning process.

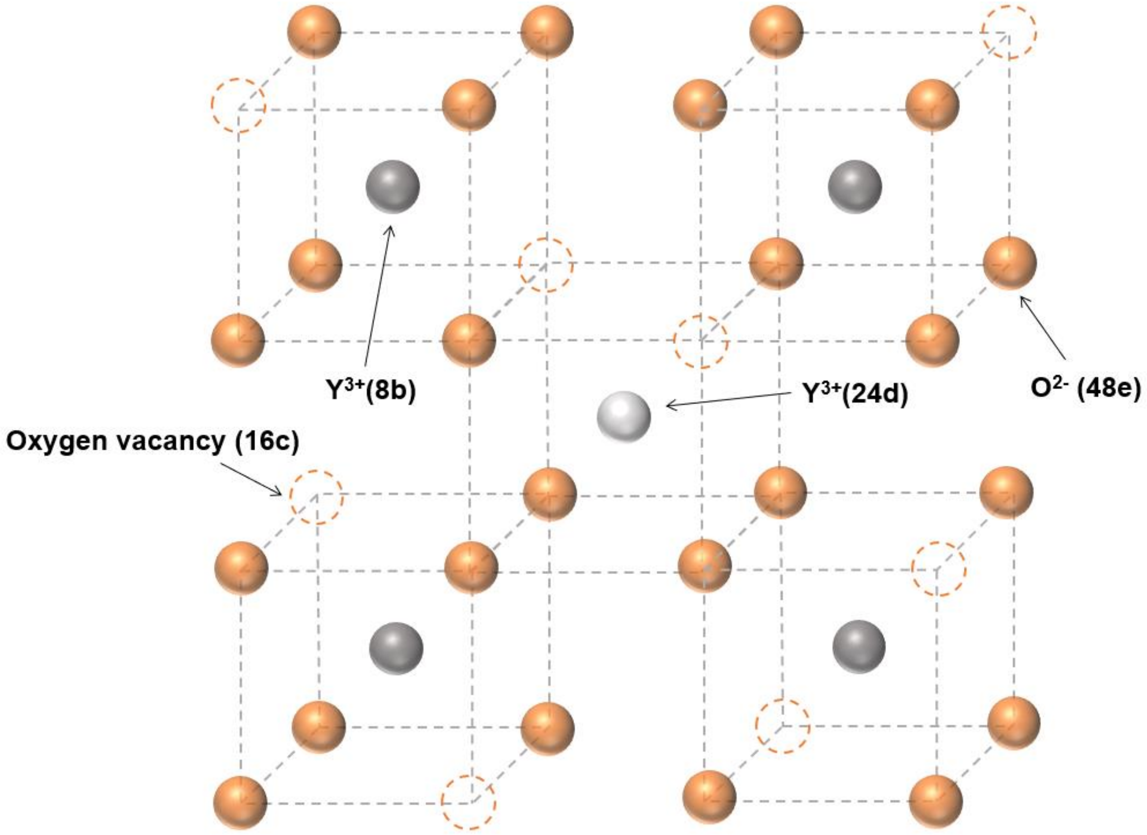

Figure 3.1 The crystal structure of cubic-Y2O3 phase (bixbyite crystal structure) [29].

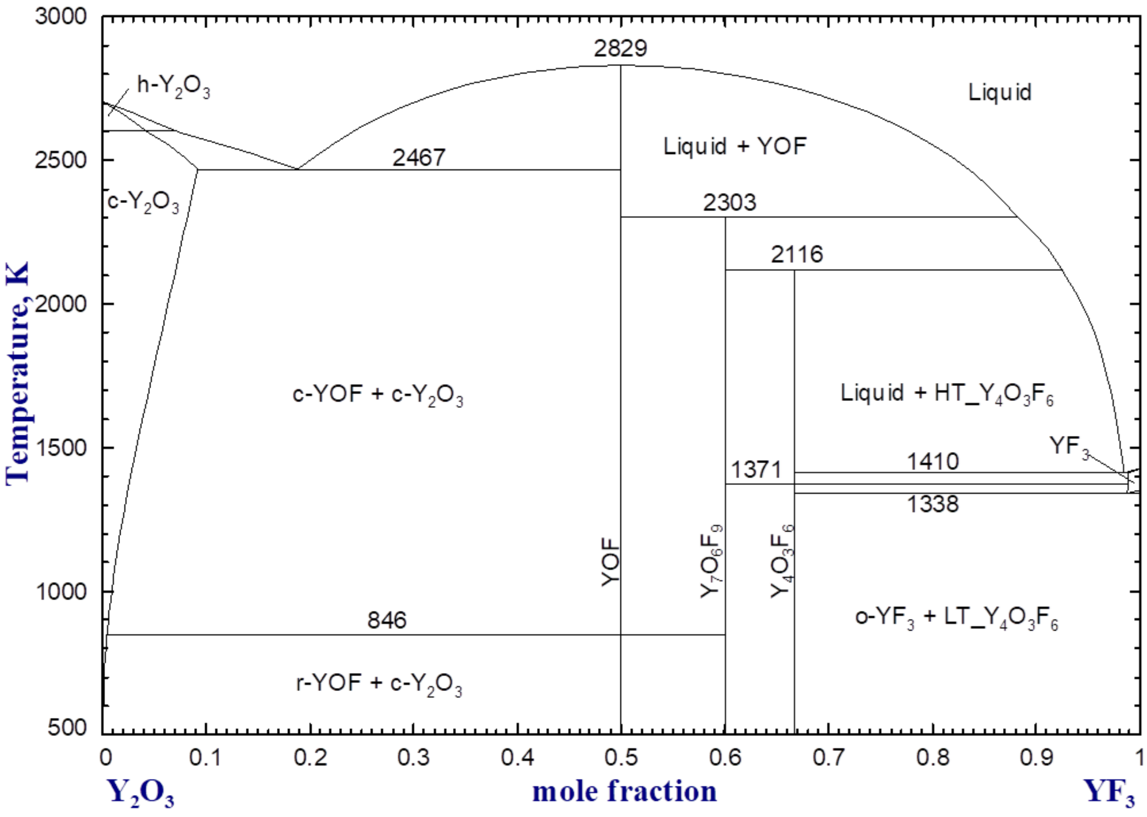
3000
2500
2000
1500
1000
500
Temperature, K
0
0.1
0.2
0.3
0.4
0.5
0.6
0.7
0.8
0.9
1
Y_2O_3
mole fraction
YF_3
2829
h-Y_2O_3
Liquid
Liquid + YOF
2467
c-Y_2O_3
2303
2116
c-YOF + c-Y_2O_3
Liquid + HT_$Y_4O_3F_6$
YF_3
1371
1410
1338
YOF
$Y_7O_6F_9$
$Y_4O_3F_6$
o-YF_3 + LT_$Y_4O_3F_6$
846
r-YOF + c-Y_2O_3

(a)

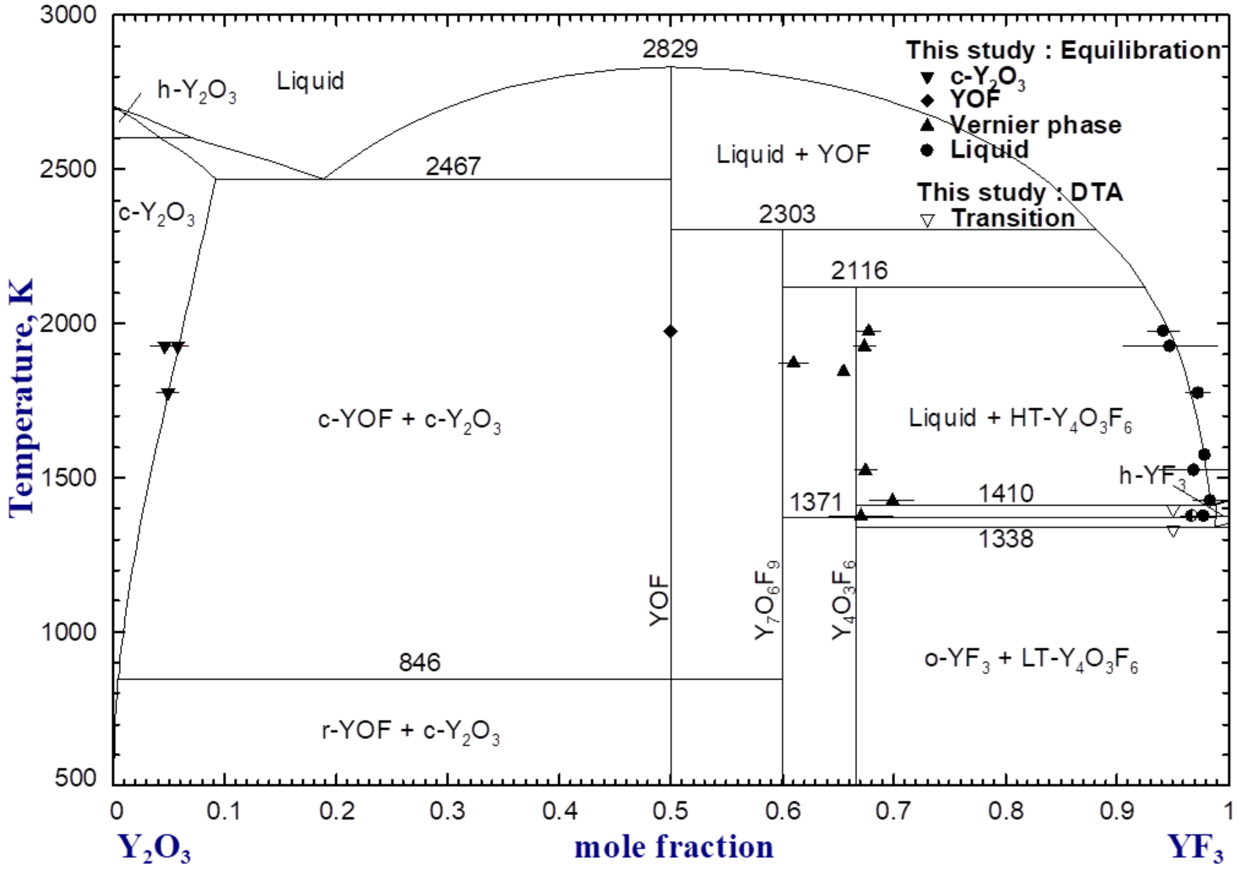
Temperature, K
3000
2500
2000
1500
1000
500
0
0.1
0.2
0.3
0.4
0.5
0.6
0.7
0.8
0.9
1
Y_2O_3
mole fraction
YF_3
This study : Equilibration
▼ c-Y_2O_3
◆ YOF
▲ Vernier phase
● Liquid
This study : DTA
▽ Transition
h-Y_2O_3
Liquid
2829
2467
Liquid + YOF
2303
2116
c-Y_2O_3
c-YOF + c-Y_2O_3
Liquid + HT-$Y_4O_3F_6$
h-YF_3
1410
1371
1338
YOF
$Y_7O_6F_9$
$Y_4O_3F_6$
846
o-YF_3 + LT-$Y_4O_3F_6$
r-YOF + c-Y_2O_3

(b)

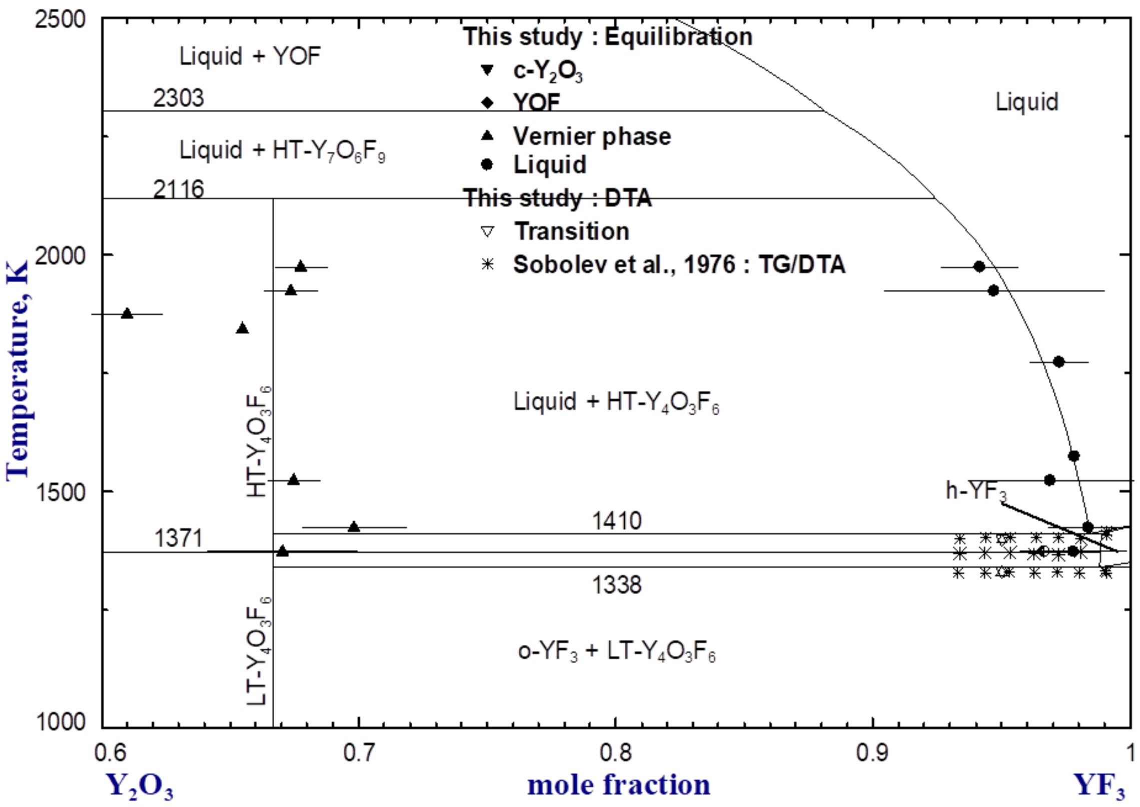

(c)

Figure 3.2 Calculated optimized phase diagram of the Y_2O_3-YF_3 system in the present study along with experimental data.

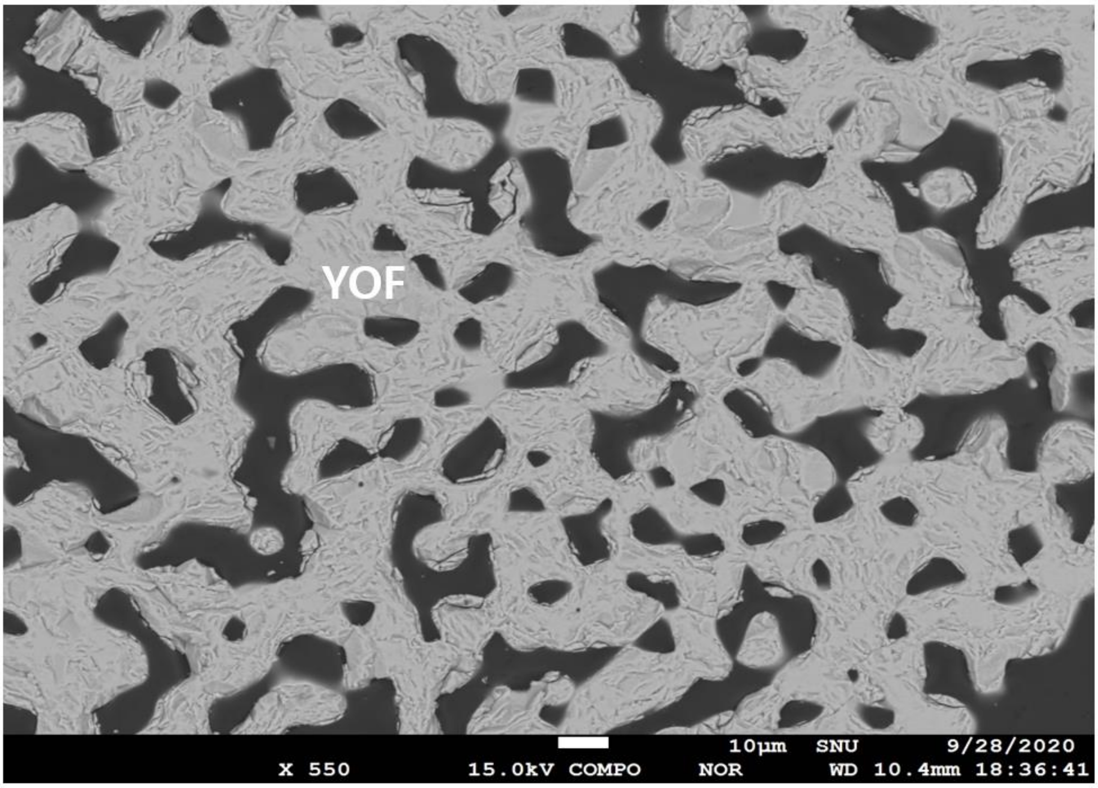

(a)

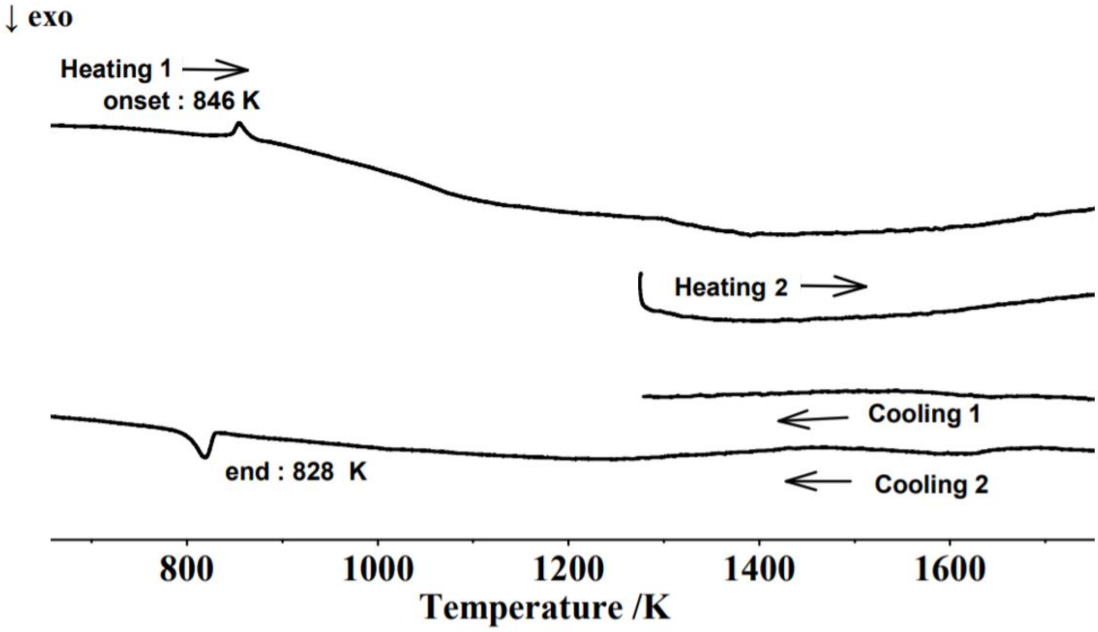

(b)

Figure 3.3 Experimental results of YOF sample (sample #1). (a) EPMA BSE image of the quenched sample at 1973 K, and (b) DTA result.

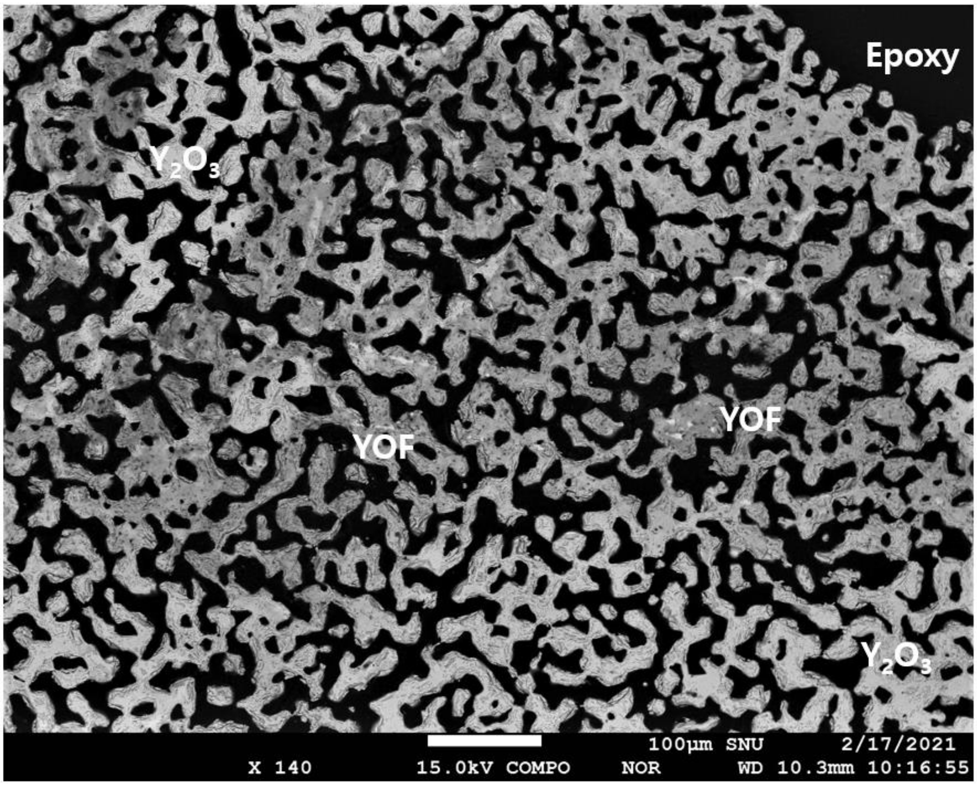
Epoxy
Y2O3
YOF
YOF
Y2O3
100μm SNU 2/17/2021
X 140 15.0kV COMPO NOR WD 10.3mm 10:16:55

(a)

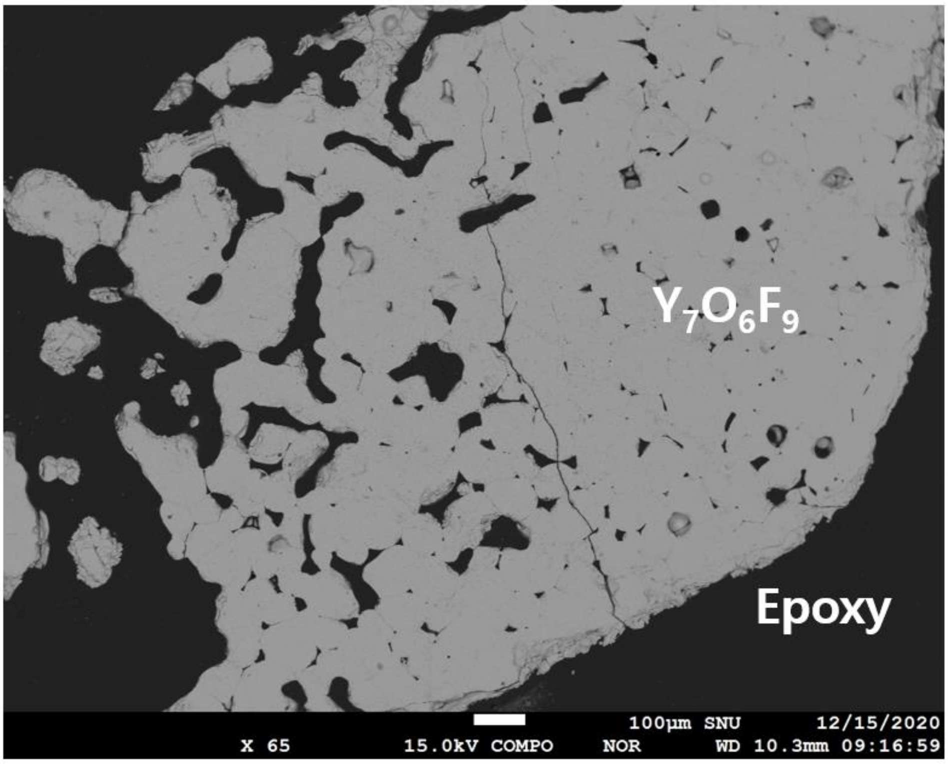
Y7O6F9
Epoxy
100μm SNU 12/15/2020
X 65 15.0kV COMPO NOR WD 10.3mm 09:16:59

(b)

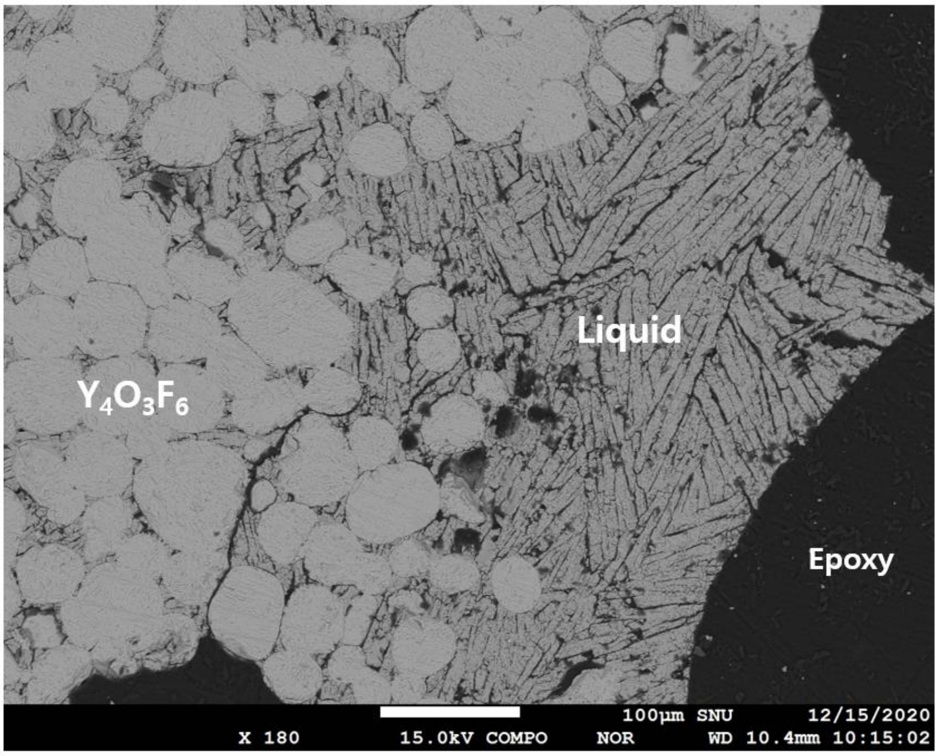
Liquid
$Y_4O_3F_6$
Epoxy
100µm SNU 12/15/2020
X 180 15.0kV COMPO NOR WD 10.4mm 10:15:02

(c)

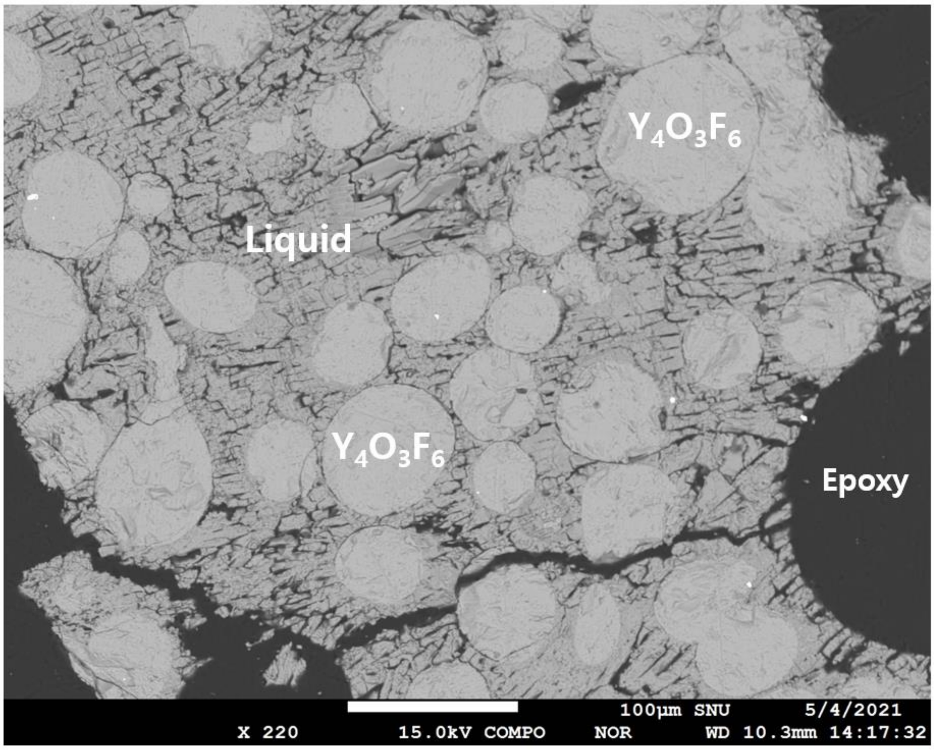
$Y_4O_3F_6$
Liquid
$Y_4O_3F_6$
Epoxy
100µm SNU 5/4/2021
X 220 15.0kV COMPO NOR WD 10.3mm 14:17:32

(d)

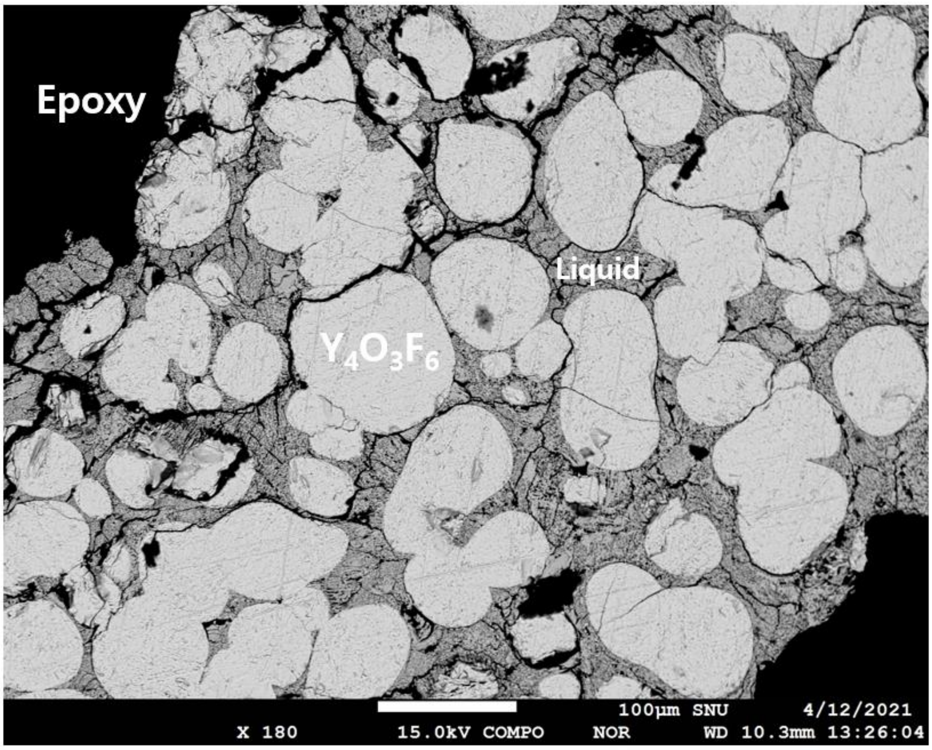

(e)

Figure 3.4 EPMA BSE images of the quenched samples. (a) sample #4, (b) #6, (c) #7, (d) #11 and (e) #9.

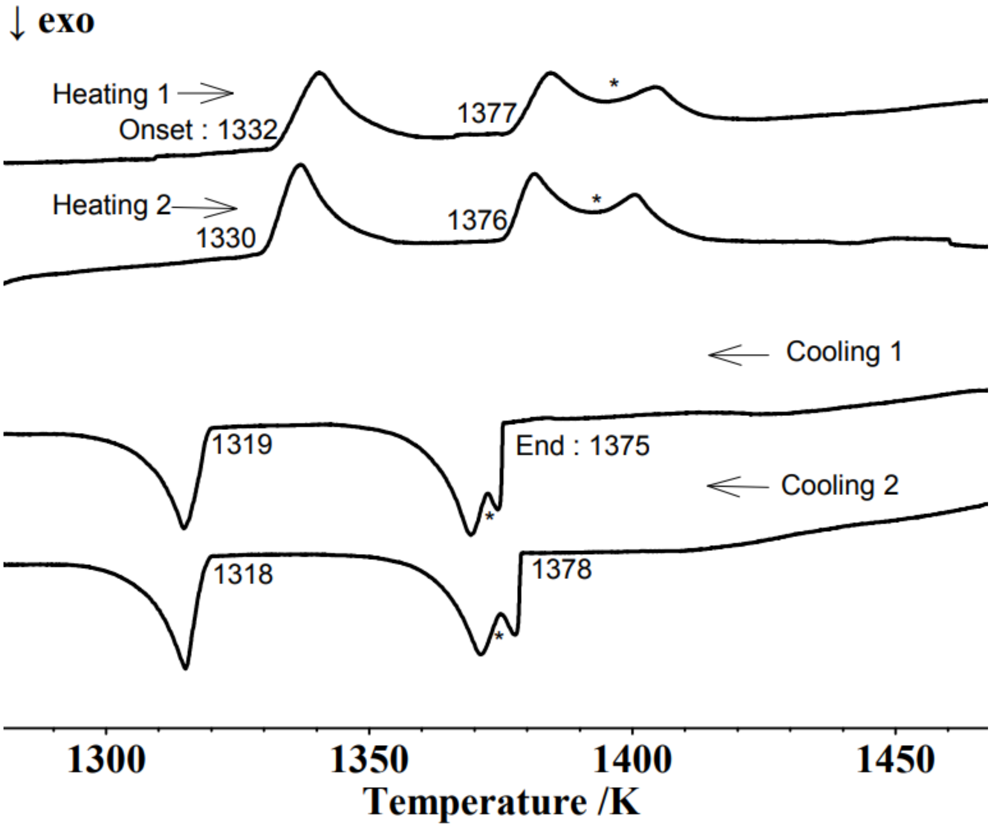
↓ exo
Heating 1
Onset : 1332
1377
*
Heating 2
1330
1376
*
Cooling 1
1319
End : 1375
*
Cooling 2
1318
1378
*
1300
1350
1400
1450
Temperature /K

(a)

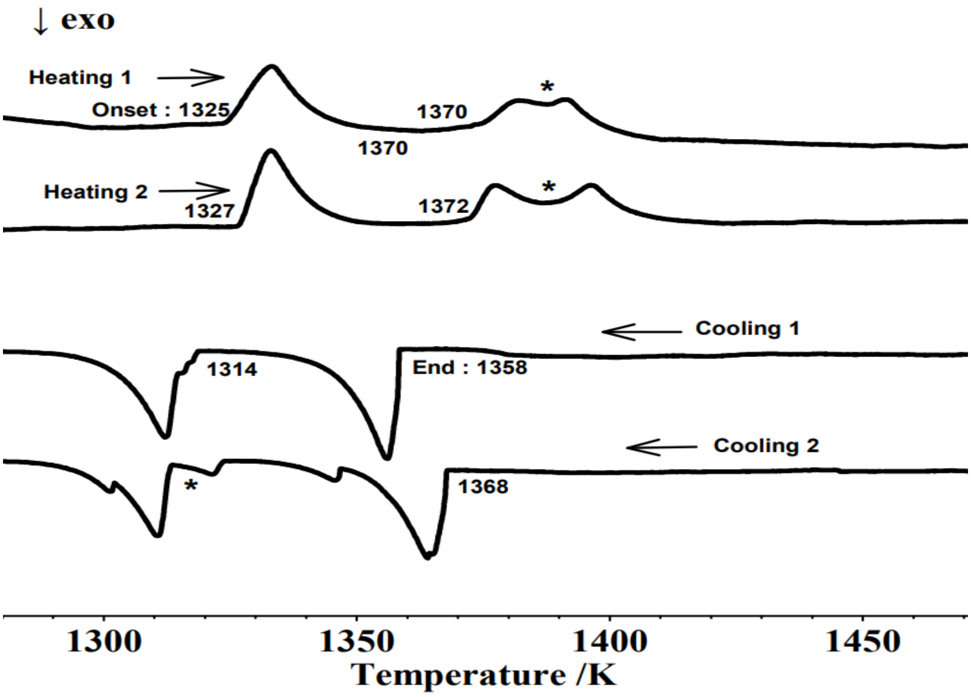
↓ exo
Heating 1
Onset : 1325
1370
*
1370
Heating 2
1327
1372
*
Cooling 1
1314
End : 1358
Cooling 2
*
1368
1300
1350
1400
1450
Temperature /K

(b)

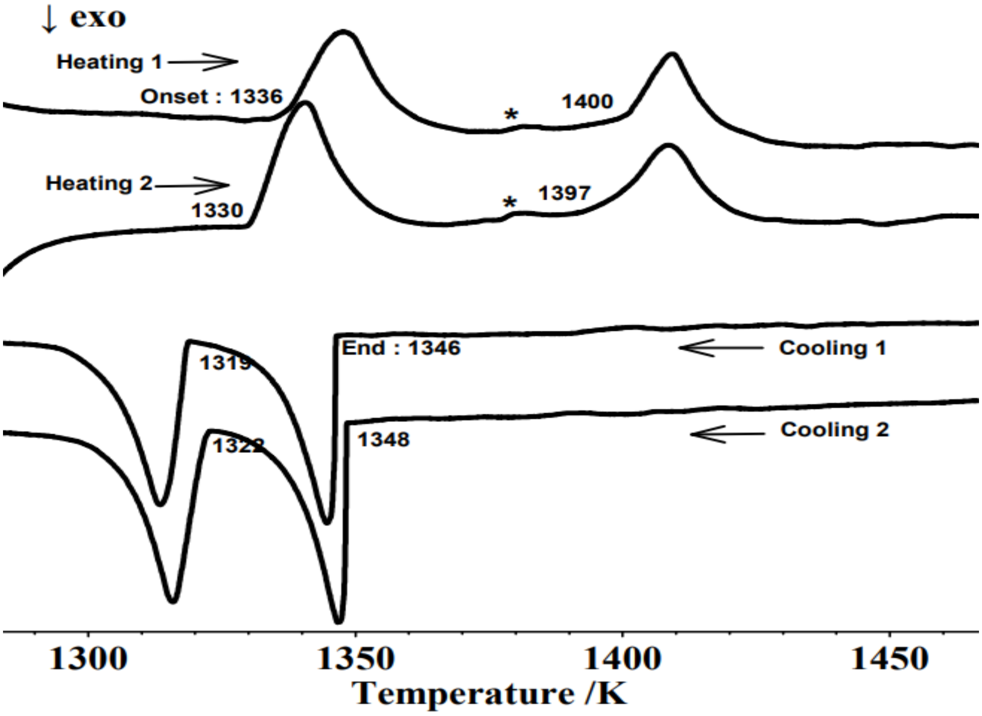

(c)

Figure 3.5 DTA results for the samples of (a) 0.5 YOF + 0.5 YF_3, (b) 0.4 YOF + 0.6 YF_3 and (c) 0.1 YOF + 0.9 YF_3 in mol fraction.

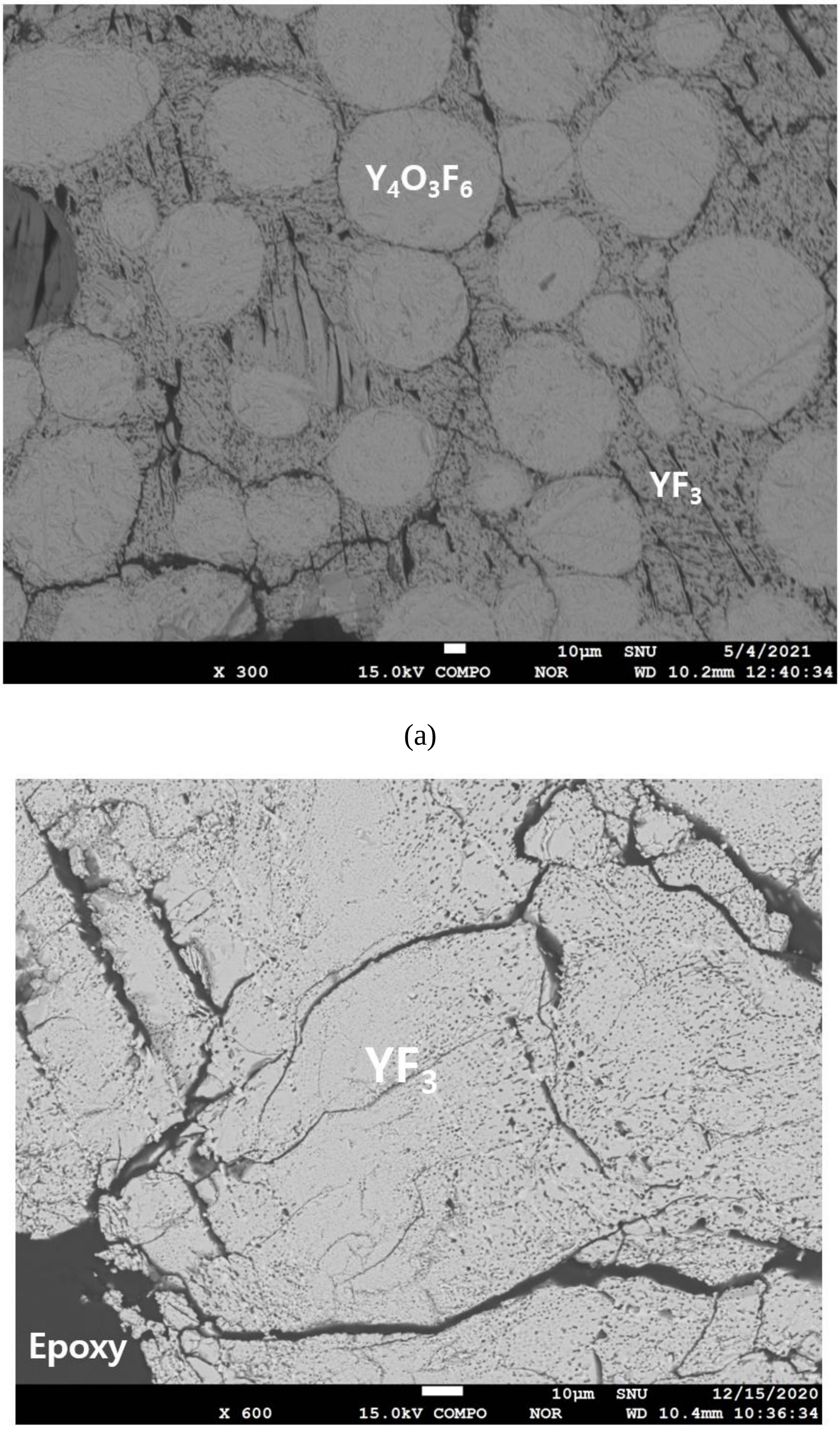

(a)

(b)

Figure 3.6 EPMA BSE images of the quenched samples in the YF_3-rich region. (a) sample #10 and (b) sample #12.

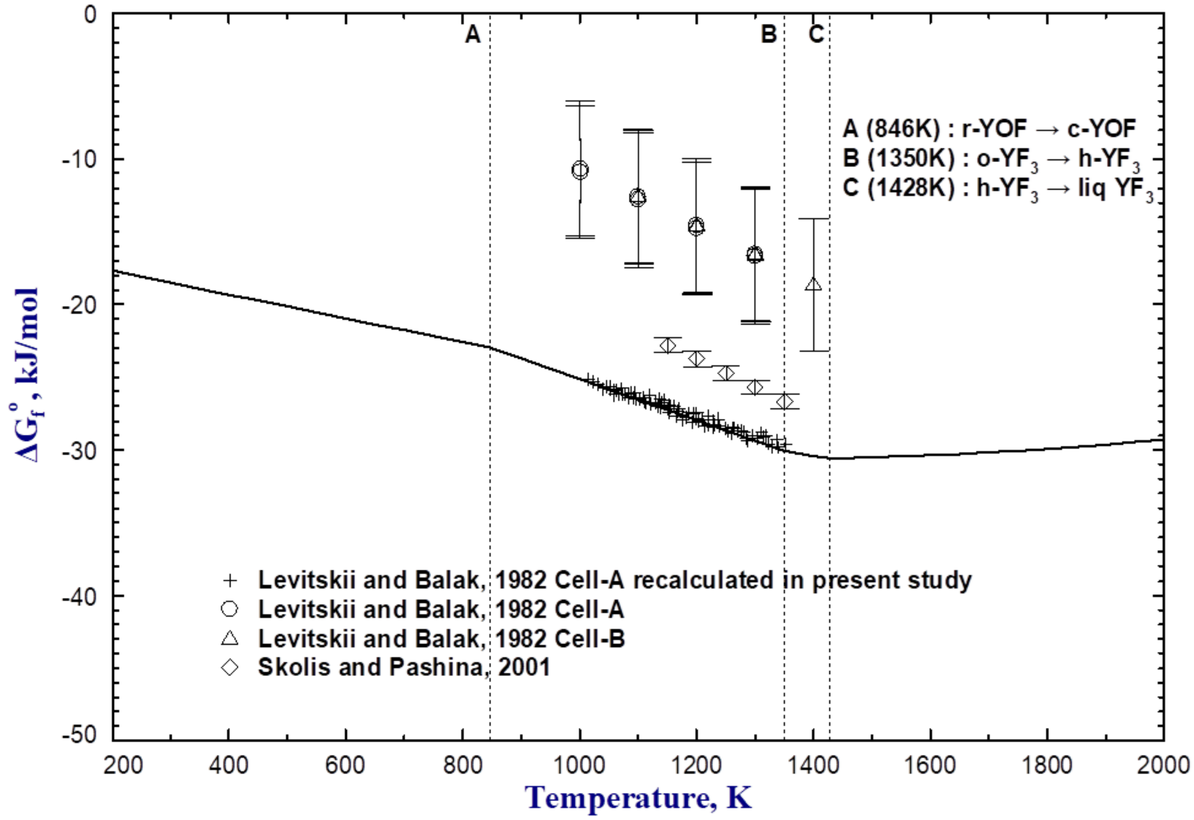
ΔG$_f^o$, kJ/mol
Temperature, K
0
-10
-20
-30
-40
-50
200
400
600
800
1000
1200
1400
1600
1800
2000
A
B
C
A (846K) : r-YOF → c-YOF
B (1350K) : o-YF$_3$ → h-YF$_3$
C (1428K) : h-YF$_3$ → liq YF$_3$
+ Levitskii and Balak, 1982 Cell-A recalculated in present study
○ Levitskii and Balak, 1982 Cell-A
△ Levitskii and Balak, 1982 Cell-B
◇ Skolis and Pashina, 2001

(a)

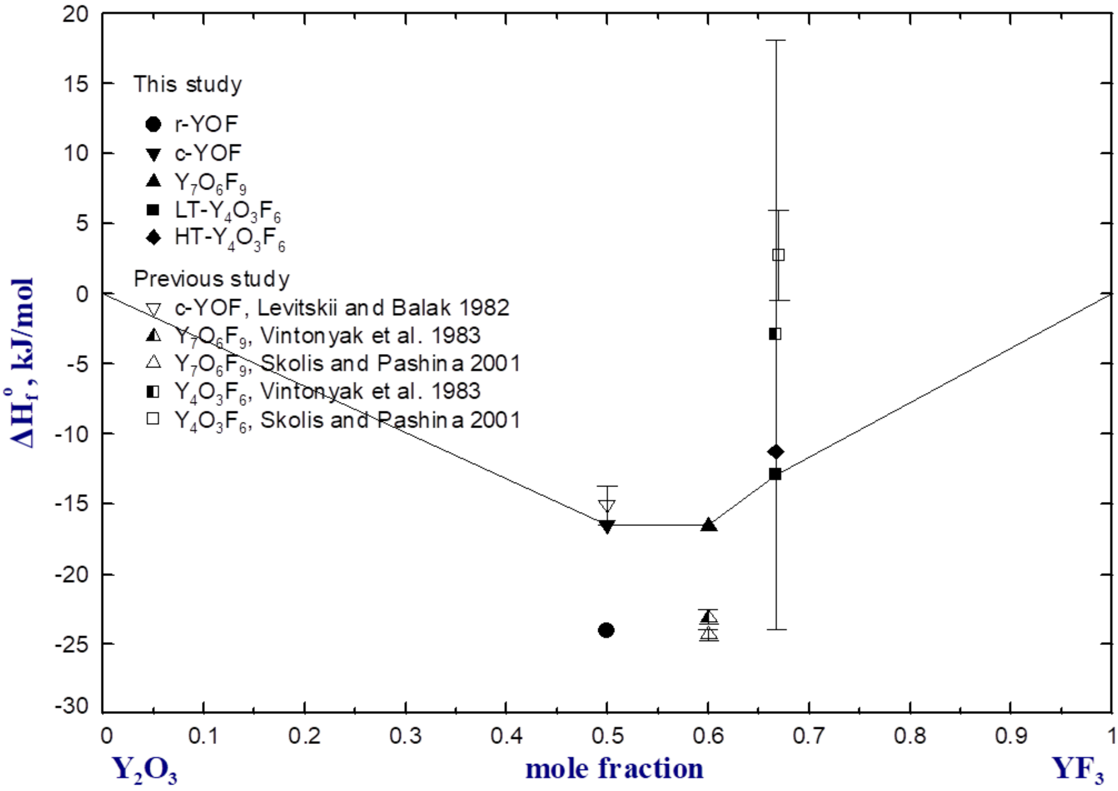
ΔH$_f^o$, kJ/mol
mole fraction
Y$_2$O$_3$
YF$_3$
20
15
10
5
0
-5
-10
-15
-20
-25
-30
0
0.1
0.2
0.3
0.4
0.5
0.6
0.7
0.8
0.9
1
This study
● r-YOF
▼ c-YOF
▲ Y$_7$O$_6$F$_9$
■ LT-Y$_4$O$_3$F$_6$
◆ HT-Y$_4$O$_3$F$_6$
Previous study
▽ c-YOF, Levitskii and Balak 1982
Y$_7$O$_6$F$_9$, Vintonyak et al. 1983
△ Y$_7$O$_6$F$_9$, Skolis and Pashina 2001
Y$_4$O$_3$F$_6$, Vintonyak et al. 1983
□ Y$_4$O$_3$F$_6$, Skolis and Pashina 2001

(b)

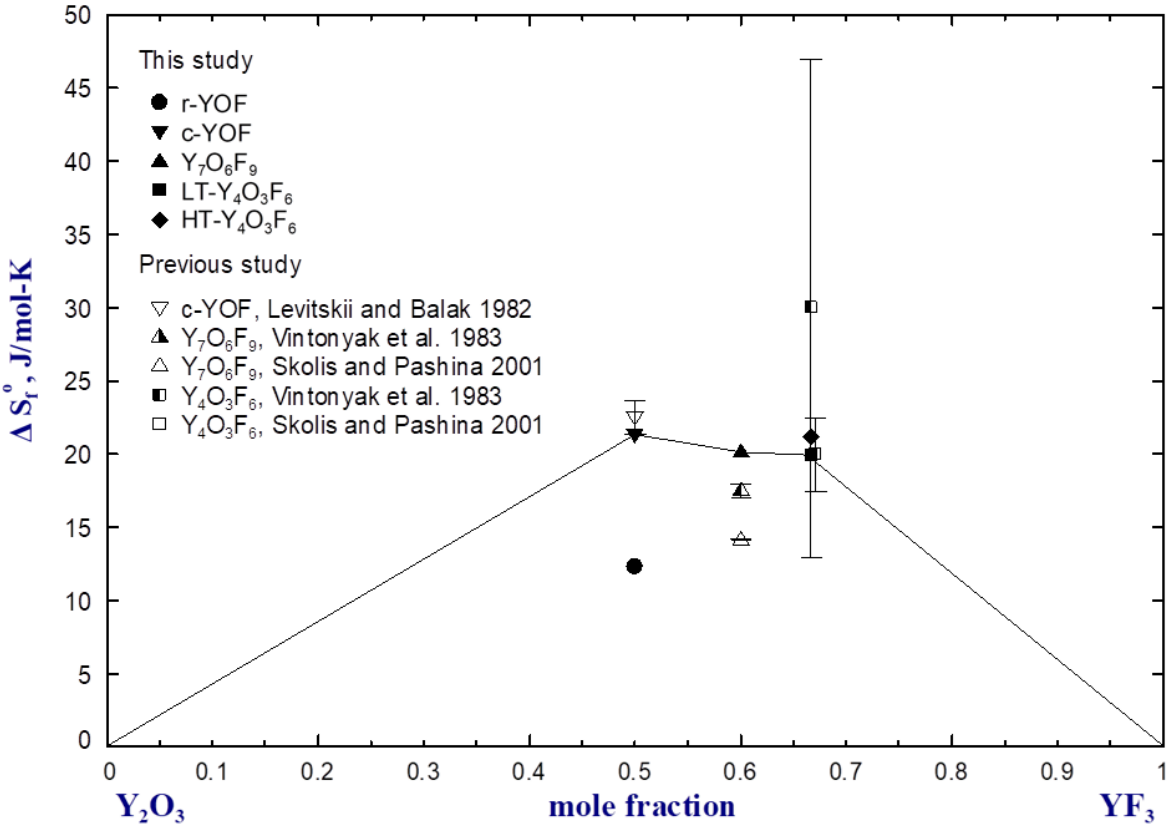

(c)

Figure 3.7 The optimized thermodynamic properties calculated in the present study compared with the experimental data in literature [12-14]. (a) Gibbs Energy of formation of YOF ($1/3Y_2O_3 + 1/3YF_3 = YOF$), (b) the enthalpy and (c) entropy of formation of YOF and vernier phases at 298 K.

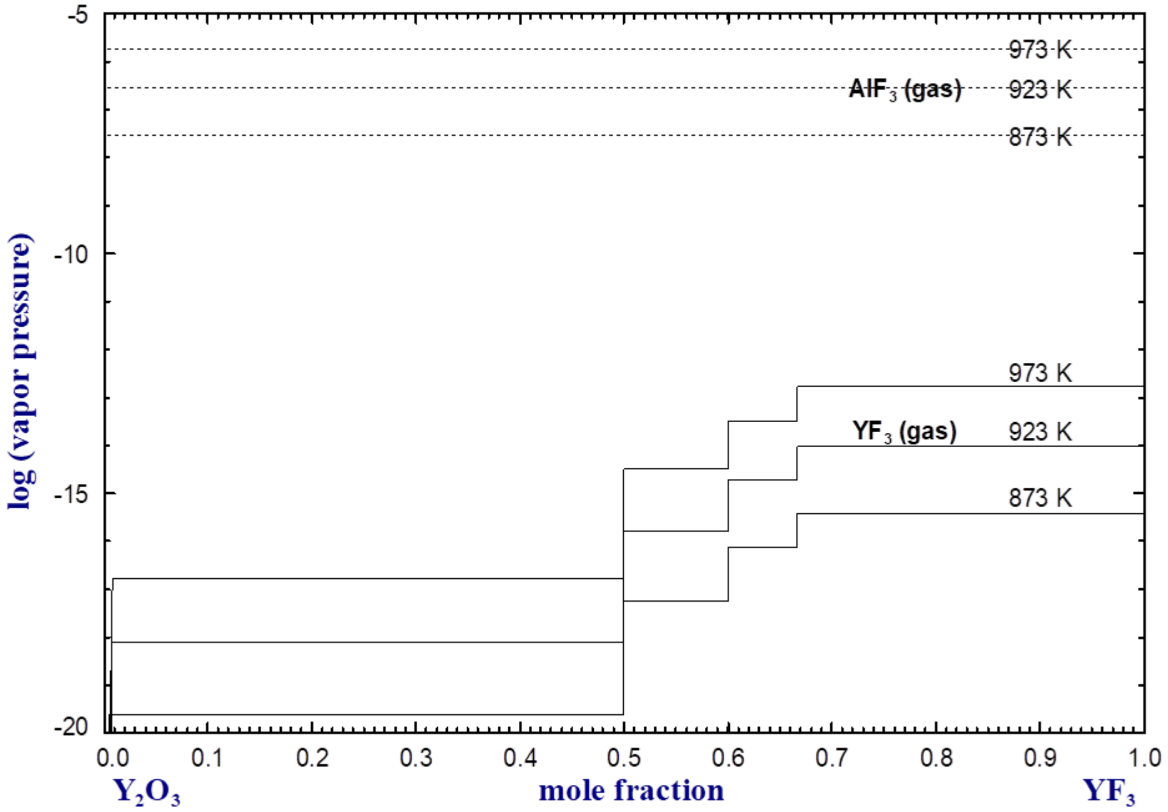

Figure 3.8 Calculated vapor pressures of YF_3(g) in the binary Y_2O_3-YF_3 system at 873, 923, and 973 K, in comparison with the vapor pressure of AlF_3 (g) in equilibrium with solid AlF_3.

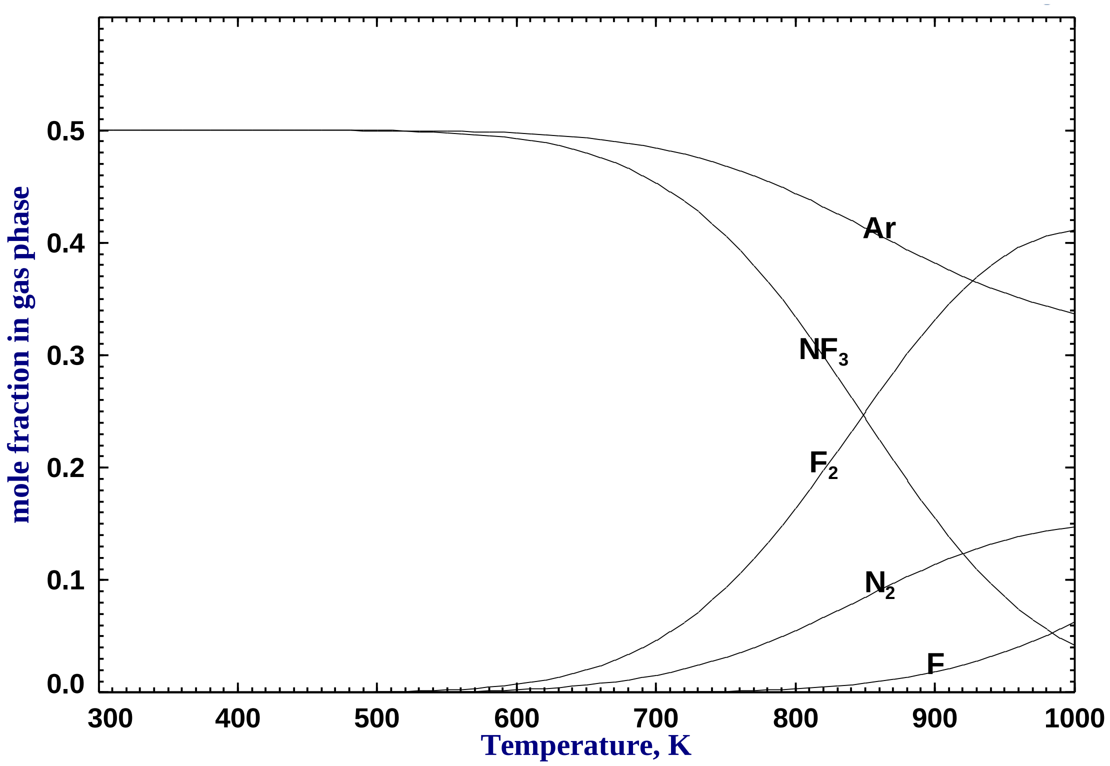
mole fraction in gas phase
0.0
0.1
0.2
0.3
0.4
0.5
Temperature, K
300
400
500
600
700
800
900
1000
Ar
NF$_3$
F$_2$
N$_2$
F

(a)

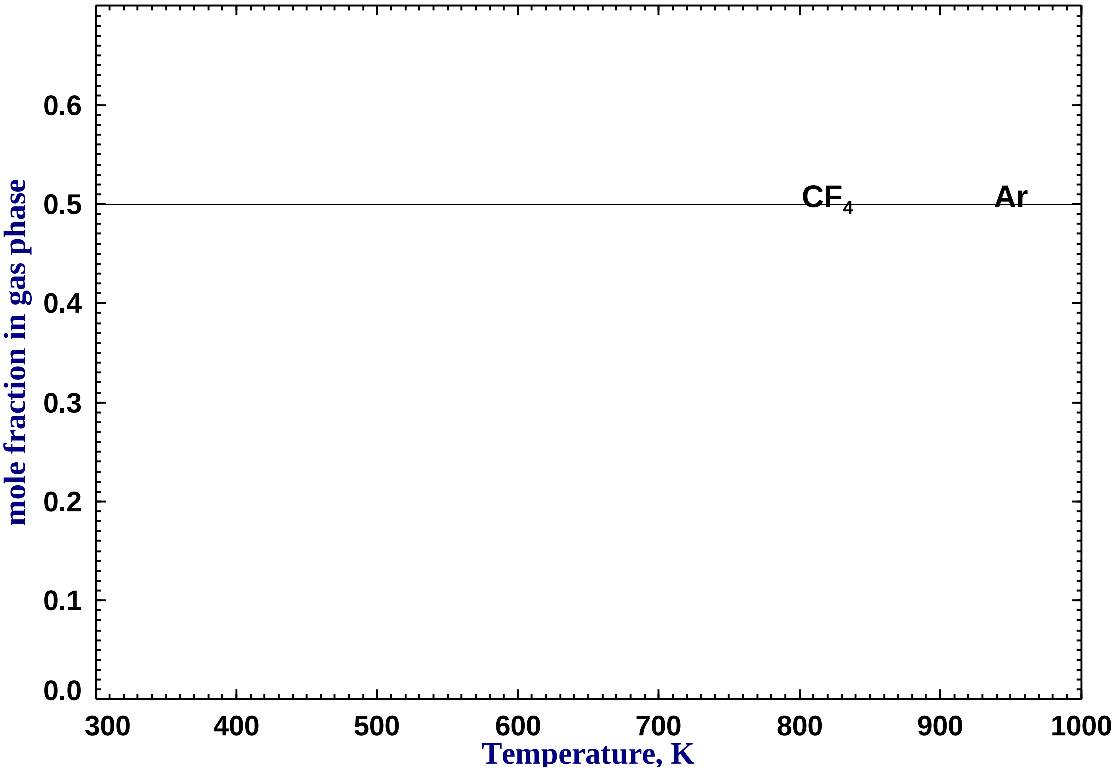
mole fraction in gas phase
0.0
0.1
0.2
0.3
0.4
0.5
0.6
Temperature, K
300
400
500
600
700
800
900
1000
CF$_4$
Ar

(b)

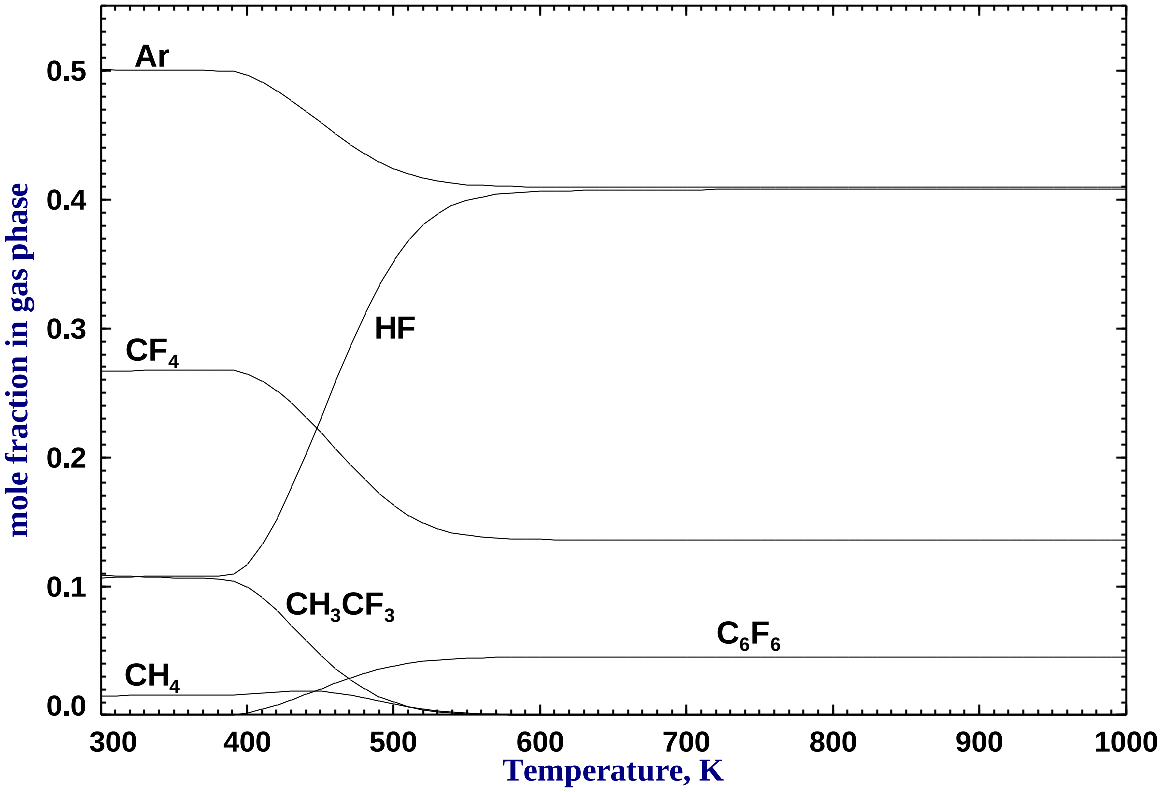

(c)

Figure 3.9 Dissociation of fluorine containing gas species with temperature. (a) 0.5 NF_3 + 0.5Ar, (b) 0.5 CF_4 + 0.5 Ar, and (c) 0.5 CHF_3 + 0.5 Ar in mol fraction. In the calculations, no solid phase was assumed.

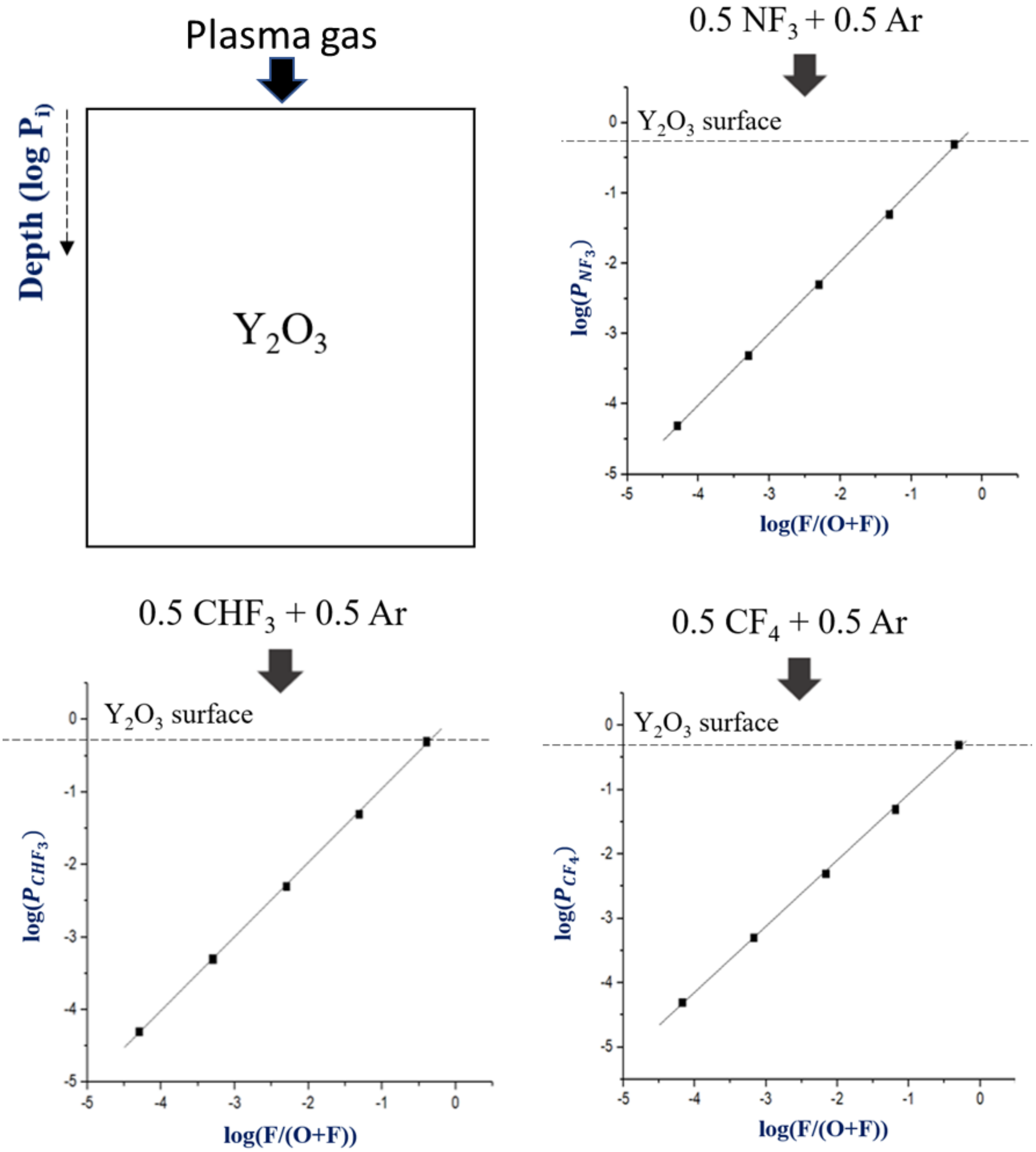

Figure 3.10 Predicted maximum solubility of YF_3 in solid Y_2O_3 crystal in equilibrium with fluorine containing gas species at 923 K. All other solid phases were suppressed in the calculations.

Table 3.1 Summary of the equilibration and quenching experimental results in the present study.

Sample	Starting composition (mol fraction)		T (K)	Duration (hrs)	Phase (XRD/ EPMA)	Composition						
	Y_2O_3	YF_3				# of analyses	Y (wt.%) (2σ)	O (wt.%) (2σ)	F (wt.%) (2σ)	Total (wt.%) (2σ)	Y_2O_3 (mol fr.) (2σ)	YF_3 (mol fr.) (2σ)
#1	0.5	0.5	1973	1	YOF	8	70.59 (2.99)	12.83 (1.87)	15.26 (0.86)	98.68 (1.42)	0.4980 (0.0054)	0.5020 (0.0054)
#2	0.75	0.25	1773	24	Y_2O_3	4	76.69 (2.57)	20.53 (3.14)	1.23 (0.35)	98.45 (4.72)	0.9517 (0.0105)	0.0483 (0.0105)
					YOF	5	71.75 (1.00)	15.19 (2.67)	13.44 (1.68)	100.38 (3.53)	0.5633 (0.0417)	0.4367 (0.0417)
#3	0.75	0.25	1923	24	Y_2O_3	5	76.33 (2.36)	20.19 (1.82)	1.46 (0.30)	97.98 (1.15)	0.9424 (0.0101)	0.0576 (0.0101)

					YOF	7	73.02 (1.94)	14.78 (2.07)	11.39 (1.16)	99.19 (1.64)	0.6072 (0.0280)	0.3928 (0.0280)
#4	0.75	0.25	1923	168	Y_2O_3	11	79.01 (1.41)	18.55 (1.27)	1.41 (0.35)	98.96 (1.09)	0.9424 (0.0138)	0.0576 (0.0138)
					YOF	6	73.86 (2.04)	14.36 (2.01)	10.48 (1.49)	98.70 (2.02)	0.6268 (0.0436)	0.3732 (0.0436)
#5	0.60	0.40	1923	168	Y_2O_3	10	78.18 (2.03)	19.66 (1.20)	1.15 (0.32)	98.99 (2.18)	0.9541 (0.0123)	0.0459 (0.0123)
					YOF	8	73.04 (3.26)	13.89 (2.97)	13.78 (2.74)	100.71 (3.18)	0.5457 (0.0498)	0.4543 (0.0498)
#6	0.40	0.60	1873	2	$Y_7O_6F_9$	9	71.06 (1.46)	9.42 (0.68)	18.84 (0.86)	99.32 (1.43)	0.3902 (0.0138)	0.6098 (0.0138)
#7	0.30	0.70	1523	2	$Y_4O_3F_6$	5	69.23 (1.60)	8.01 (0.24)	21.37 (0.78)	98.61 (1.93)	0.3256 (0.0101)	0.6744 (0.0101)
					Liquid	5	61.28 (3.61)	0.83 (0.51)	36.46 (4.53)	98.58 (2.37)	0.0314 (0.0322)	0.9686 (0.0322)

#8	0.25	0.75	1923	24	$Y_4O_3F_6$	3	70.39	8.36	21.88	100.63	0.3265	0.6735
							(1.51)	(0.38)	(0.77)	(0.54)	(0.0103)	(0.0103)
					Liquid	12	60.52	1.76	35.25	97.54	0.0529	0.9471
							(3.95)	(2.41)	(3.41)	(3.39)	(0.0428)	(0.0428)
#9	0.25	0.75	1973	1	$Y_4O_3F_6$	4	70.15	7.39	21.11	98.65	0.3226	0.6774
							(0.59)	(0.43)	(2.37)	(2.16)	(0.0409)	(0.0409)
					Liquid	6	63.06	1.47	34.86	99.40	0.0586	0.9414
							(1.56)	(2.14)	(3.80)	(3.57)	(0.0589)	(0.0589)
#10	0.20	0.80	1373	24	$Y_4O_3F_6$	4	69.95	8.06	21.26	99.27	0.3298	0.6702
							(0.68)	(1.21)	(1.36)	(1.45)	(0.0294)	(0.0294)
					YF_3	4	61.07	0.62	37.44	99.13	0.0221	0.9779
							(4.42)	(0.91)	(7.81)	(3.08)	(0.0710)	(0.0710)
#11	0.20	0.80	1423	24	$Y_4O_3F_6$	5	68.11	7.93	22.76	98.81	0.3019	0.6981
							(1.28)	(1.41)	(2.23)	(2.96)	(0.0201)	(0.0201)
					Liquid	5	57.93	1.21	38.33	97.47	0.0163	0.9837
							(3.73)	(0.93)	(3.81)	(2.53)	(0.0334)	(0.0334)

#12	0.10	0.90	1373	24	$Y_4O_3F_6$		Not analyzed					
					YF_3	6	61.94 (1.23)	1.01 (0.66)	36.89 (1.65)	99.83 (2.74)	0.0335 (0.0164)	0.9665 (0.0164)
#13	0.10	0.90	1773	3	$Y_4O_3F_6$		Not analyzed					
					Liquid	9	61.81 (1.61)	1.26 (0.49)	38.65 (1.51)	101.72 (1.60)	0.0276 (0.0113)	0.9724 (0.0113)

Table 3.2 Phase transitions determined by differential thermal analysis in the present study.

No.	Composition (mol fr.)		Temperature (K)		Reaction
	Y_2O_3	YF_3	1st heating	2nd heating	
1	0.5	0.5	846		*r*-YOF → *c*-YOF
2	0.25	0.75	1332	1330	*o*-YF_3 + LT-$Y_4O_3F_6$ → *h*-YF_3 + LT-$Y_4O_3F_6$
			1377	1376	*h*-YF_3 + LT-$Y_4O_3F_6$ → *h*-YF_3 + HT-$Y_4O_3F_6$
			1397	1394	*h*-YF_3 + HT-$Y_4O_3F_6$ → liquid + HT-$Y_4O_3F_6$
3	0.2	0.8	1325	1327	*o*-YF_3 + LT-$Y_4O_3F_6$ → *h*-YF_3 + LT-$Y_4O_3F_6$
			1370	1372	*h*-YF_3 + LT-$Y_4O_3F_6$ → *h*-YF_3 + HT-$Y_4O_3F_6$
			1388	1390	*h*-YF_3 + HT-$Y_4O_3F_6$ → liquid + HT-$Y_4O_3F_6$
4	0.05	0.95	1336	1330	*o*-YF_3 + LT-$Y_4O_3F_6$ → *h*-YF_3 + LT-$Y_4O_3F_6$
			1378	1377	*h*-YF_3 + LT-$Y_4O_3F_6$ → *h*-YF_3 + HT-$Y_4O_3F_6$
			1400	1397	*h*-YF_3 + HT-$Y_4O_3F_6$ → liquid + HT-$Y_4O_3F_6$

* *o*-YF_3 and *h*-YF_3 represent orthorhombic and hexagonal YF_3, respectively. HT and LT represent high temperature and low temperature phases.

Table 3.3 Optimized Gibbs energies of the stoichiometric compound per formula.

Compound	$\Delta H^{o}_{298.15}$ (kJ/mol)	$S^{o}_{298.15}$ (J/mol·K)	Cp (J/mol·K)	Ref
r-YOF	-1233.129	70.806	$75.220 + 0.007\text{T} - 1.061\ \times\ 10^{6}\ \text{T}^{-2} - 5.773\ \times 10^{-7}\text{T}^{2} - 28.790\ \times \text{T}^{-0.5}$ (298 – 1000 K) $72.453 + 0.008\text{T} - 4.934\ \times\ 10^{5}\ \text{T}^{-2} - 5.773\ \times 10^{-7}\text{T}^{2}$(1000 – 1350 K) $74.236 + 0.007\text{T} - 4.934\ \times\ 10^{5}\ \text{T}^{-2} - 5.773\ \times 10^{-7}\text{T}^{2}$ (1350 – 3000 K)	This Work
c-YOF	-1228.129	76.808	$75.220 + 0.007\text{T} - 1.061\ \times\ 10^{6}\ \text{T}^{-2} - 5.773\ \times 10^{-7}\text{T}^{2} - 28.790\ \times \text{T}^{-0.5}$ (298 – 1000 K) $72.453 + 0.008\text{T} - 4.934\ \times\ 10^{5}\ \text{T}^{-2} - 5.773\ \times 10^{-7}\text{T}^{2}$(1000 – 1350 K) $74.236 + 0.007\text{T} - 4.934\ \times\ 10^{5}\ \text{T}^{-2} - 5.773\ \times 10^{-7}\text{T}^{2}$ (1350 – 3000 K)	This Work

c-YOF	−1228.129	76.808		[12]
$Y_7O_6F_9$	−9103.400	565.000	$562.418 + 0.040T - 8.066 \times 10^6 T^{-2} - 3.464 \times 10^{-6} T^2 - 259.110 \times T^{-0.5}$ (298 – 1000 K)	This Work
			$537.518 + 0.052T - 2.961 \times 10^6 T^{-2} - 3.464 \times 10^{-9} T^2$(1000 – 1350 K)	
			$553.568 + 0.040T - 2.961 \times 10^6 T^{-2} - 3.464 \times 10^{-6} T^2$ (1350 – 3000 K)	
$Y_7O_6F_9$	−9136.018	551.637		[13]
$Y_7O_6F_9$	−9151.278	527.936		[14]
LT-$Y_4O_3F_6$	−5408.399	336.270	$336.759 + 0.020T - 4.884 \times 10^6 T^{-2} - 1.732 \times 10^{-6} T^2 - 172.740 \times T^{-0.5}$ (298 – 1000 K)	This Work
			$320.159 + 0.028T - 1.480 \times 10^6 T^{-2} - 1.732 \times 10^{-6} T^2$(1000 – 1350 K)	
			$330.859 + 0.020T - 1.480 \times 10^6 T^{-2} -$	

			$1.732 \times 10^{-6}\mathrm{T}^{2}$ (1350 – 3000 K)	
HT-$Y_4O_3F_6$	−5403.399	339.917	$336.759 + 0.020\mathrm{T} - 4.884 \times 10^{6}\,\mathrm{T}^{-2} - 1.732 \times 10^{-6}\mathrm{T}^{2} - 172.740 \times \mathrm{T}^{-0.5}$ (298 – 1000 K) $320.159 + 0.028\mathrm{T} - 1.480 \times 10^{6}\,\mathrm{T}^{-2} - 1.732 \times 10^{-6}\mathrm{T}^{2}$(1000 – 1350 K) $330.859 + 0.020\mathrm{T} - 1.480 \times 10^{6}\,\mathrm{T}^{-2} - 1.732 \times 10^{-6}\mathrm{T}^{2}$ (1350 – 3000 K)	This Work
LT-$Y_4O_3F_6$	−5378.383	366.410		[13]
LT-$Y_4O_3F_6$	−5351.754	336.334		[14]
c-Y_2O_3	-1932.800	99.130	$114.559 + 0.020\mathrm{T} - 1.480 \times 10^{6}\,\mathrm{T}^{-2} - 1.732 \times 10^{-6}\mathrm{T}^{2}$ (298 – 3000 K)	[26]
h-Y_2O_3	-1906.412	109.279	$114.559 + 0.020\mathrm{T} - 1.480 \times 10^{6}\,\mathrm{T}^{-2} - 1.732 \times 10^{-6}\mathrm{T}^{2}$ (298 – 3000 K)	[26]

l-Y_2O_3	-1862.777	125.422	$114.559 + 0.020T - 1.480 \times 10^6\,T^{-2} - 1.732 \times 10^{-6}T^2$ (298 – 3000 K)	[26]
o-YF_3	-1718.369	88.701	$111.100 - 1.702 \times 10^6\,T^{-2} - 86.370 \times T^{-0.5}$ (298 – 1000 K)	[27]
			$102.800 + 0.004T$ (1000 – 1350 K)	
h-YF_3	-1685.901	112.751	$111.100 - 1.702 \times 10^6\,T^{-2} - 86.370 \times T^{-0.5}$ (298 – 1000 K)	[27]
			$102.800 + 0.004T$ (1000 – 1100 K)	
			122.303 (1100 – 1428 K)	
l-YF_3	-1657.931	132.338	$111.100 - 1.702 \times 10^6\,T^{-2} - 86.370 \times T^{-0.5}$ (298 – 1000 K)	[27]
			$102.800 + 0.004T$ (1000 – 1200 K)	
			133.683 (1200 – 1800 K)	

* r-, c-, h-, and l-phase represent rhombohedral, cubic, hexagonal, and liquid phase, respectively. HT and LT represent high temperature and low temperature phases without specific crystal structures known.

Table 3.4 The optimized thermodynamic parameters of solid and liquid solutions in the present study.

Phase and formula	Thermodynamic parameter
Liquid	$g^{00}_{Y;O,F} = -31690 + 30 * T$
(Y)(O,F)	$g^{02}_{Y;O,F} = -18000$
c-Y_2O_3	$G^{o}_{Y_2;O_3;Va_1} = G^{o}_{Y_2O_3\#cubic}$
$(Y)_2[O,F]_3[F,Va]_1$	$G^{o}_{Y_2;F_3;Va_1} = G^{o}_{Y\#hcp} + G^{o}_{YF_3\#hexagonal}$
	$G^{o}_{Y_2;O_3;F_1} = 2G^{o}_{YOF\#cubic} - \frac{1}{3}G^{o}_{Y\#hcp} - \frac{1}{3}G^{o}_{YF_3\#hexagonal} + \frac{1}{3}G^{o}_{Y_2O_3\#cubic} + 65000 + 15.876 * T$
	$G^{o}_{Y_2;F_3;F_1} = 2G^{o}_{YOF\#cubic} + \frac{2}{3}G^{o}_{Y\#hcp} + \frac{2}{3}G^{o}_{YF_3\#hexagonal} - \frac{2}{3}G^{o}_{Y_2O_3\#cubic} + 65000 + 15.876 * T$
h-Y_2O_3	$G^{o}_{Y_2;O_3;Va_1} = G^{o}_{Y_2O_3\#hexagonal}$
$(Y)_2[O,F]_3[F,Va]_1$	$G^{o}_{Y_2;F_3;Va_1} = G^{o}_{Y\#hcp} + G^{o}_{YF_3\#hexagonal}$
	$G^{o}_{Y_2;O_3;F_1} = 2G^{o}_{YOF\#cubic} - \frac{1}{3}G^{o}_{Y\#hcp} - \frac{1}{3}G^{o}_{YF_3\#hexagonal} + \frac{1}{3}G^{o}_{Y_2O_3\#hexagonal} + 65000 + 15.876 * T$
	$G^{o}_{Y_2;F_3;F_1} = 2G^{o}_{YOF\#cubic} + \frac{2}{3}G^{o}_{Y\#hcp} + \frac{2}{3}G^{o}_{YF_3\#hexagonal} - \frac{2}{3}G^{o}_{Y_2O_3\#hexagonal} + 65000 +$

	$15.876 * T$
h-YF$_3$	$G^o_{YF_3} = G^o_{YF_3\#hexagonal}$
(YO$_{1.5}$, YF$_3$)	$G^o_{YO_{1.5}} = \frac{1}{2} G^o_{Y_2O_3\#cubic} + 2500$
	$q^{11}_{YO_{1.5};YF_3} = -75000 + 40 * T$

* c- and h-phase represent cubic and hexagonal phase, respectively.

Table 3.5 Invariant reactions in the Y2O3-YF3 system from the present thermodynamic optimization.

Reaction	Composition of the respective phases (mol % YF3)			Temperature (K)
L ↔ c-Y_2O_3 + c-YOF	18.82	9.14	50.00	2467
L ↔ c-YOF	50.00	50.00		2829
L + c-YOF ↔ $Y_7O_6F_9$	88.08	50.00	60.00	2303
L +$Y_7O_6F_9$ ↔ HT-$Y_4O_3F_6$	97.21	60.00	66.67	2116
L ↔ HT-$Y_4O_3F_6$ + h-YF_3	98.43	66.67	98.87	1410
HT-$Y_4O_3F_6$ ↔ LT-$Y_4O_3F_6$	66.67	66.67		1371
h-YF_3 ↔ LT-$Y_4O_3F_6$ + o-YF_3	98.78	66.67	100.00	1338

* o-, c-, h-, and l-phase represent orthorhombic, cubic, hexagonal, and liquid phase, respectively. HT and LT represent high temperature and low temperature phases without specific crystal structures known.

Chapter. 4 A Coupled Phase Diagram Experiment and Thermodynamic Optimization of the MgO-MgF_2-Y_2O_3-YF_3 system

4.1 Introduction

AlN ceramic heater is commonly used in semiconductor processing as it has comparable thermal expansion properties to silicon wafer. However, AlN can react with fluorine radical to form AlF_3 layer in the plasma etching process using fluorocarbon plasma gas. As AlF_3 can sublimates in the semiconductor etching and cleaning process due to its relative high vapor pressure and condensate back at low temperature zone which causes a source of contaminated particles. This can result in a significant loss in yield, since semiconductor processing must be performed under strict environmental conditions and even tiny particles can have an impact on the quality of the product [6, 7]. Due to this reason, Y_2O_3 and YOF coating are already applied in AlN heater to minimize the contamination from heater materials, and even Y_2O_3-MgO coating is currently investigated for high temperature semiconductor etching process [8, 11, 35, 36]. In order to understand the chemical reaction of the Y_2O_3-MgO coating under fluorine containing gas environment, the thermodynamic and phase diagram information of the (Mg,Y//O,F) reciprocal system (MgO-Y_2O_3-MgF_2-YF_3 system) is essential. Y_2O_3 based ceramics are also widely used for high temperature refractory and coating materials. For sintering Y_2O_3 based ceramics, alkali and alkali-earth fluoride additives can be used to accelerate the sintering of yttria by forming liquid phase at grain boundary [37]. When Y_2O_3 based ceramics are exposed to slag containing MgO and fluoride, understanding of phase equilibria of the (Mg,Y//O,F) reciprocal system is necessary to interpretate the refractory corrosion mechanism.

The phase diagrams of the binary systems MgO-Y_2O_3, MgF_2-YF_3, and MgO-MgF_2 are reasonably known in the literature. The details will be discussed below. The present authors performed the phase diagram study and thermodynamic modeling of the Y_2O_3-YF_3 system containing YOF phase and present the complete thermodynamic properties and phase diagram of the system very recently [5]. However, no study has been conducted for the phase diagram and the thermodynamic properties of the MgO-Y_2O_3-MgF_2-YF_3 reciprocal system so far.

In the present study, the phase diagram of the MgO-Y_2O_3-MgF_2-YF_3 reciprocal system was experimentally determined. Thermodynamic modelings of the binary systems, MgO-Y_2O_3, MgO-MgF_2 and MgF_2-YF_3, and the Mg,Y//O,F reciprocal system were also performed using the CALculation of PHAse Diagram (CALPHAD) method. All thermodynamic calculations in the present study were performed using the FactSage^{TM} thermochemical software [15, 16].

4.2 Literature Review

4.2.1 MgO-MgF_2 system

Two experimental studies were conducted to investigate the phase diagram of the MgO-MgF_2 system. Hinz and Kunth [38] employed optical microscopic and X-ray diffraction (XRD) analysis to confirm the eutectic reaction between MgO and MgF_2 after the phase equilibrium experiment. No solution and intermediate compound were shown in the X-ray pattern. The melting temperature of MgF_2 was determined to be 1513 K. The eutectic reaction was determined to be 10 mol % of MgO at 1487 K. Berak and Tomczak [39] employed differential thermal analysis (DTA), and quenching experiment followed by optical microscopic analysis and XRD analysis for crystalline phase, and proposed the eutectic reaction at 8 mol % MgF_2 and 1499 K. In addition, the melting temperature of MgF_2 was determined to be 1533 K. Tomlinson and Welch [40] performed careful DTA experiments for the sample up to 12 mol % MgO, and determined the liquidus of MgF_2 and eutectic reaction at 8.4 mol % MgO and 1503 K. The melting temperature of MgF_2 was estimated to be 1533 K from the liquidus of MgF_2 between about 1 to 8 mol % MgO. Most recently, Sharma [41] conducted DTA and determined the eutectic reaction at 8.5 mol % of MgF_2 and 1501 K. Melting temperature of MgF_2 was also determined to be 1538 K. In summary, the reported eutectic reaction of the present system, L → MgF_2+MgO, is at 8.0-10 mol% MgO and 1487-1503 K. The accuracy of the eutectic temperature of this binary system can influence directly to the eutectic temperature in the Mg,Y//O,F reciprocal system. In order to confirm the eutectic temperature of this binary system, DTA experiment was also performed in the present study. The details are explained below.

4.2.2 MgO-Y_2O_3 system

Tresvyatsky et al.[42] determined the eutectic reaction and liquidus of the MgO-Y_2O_3 system by DTA experiment. Samples up to 0.7 mol fraction of MgO were examined in the range of temperature from 1773 to 2673 K by DTA and optical microscopic analysis. They investigated the solubility of MgO in cubic-Y_2O_3 (*c*-Y_2O_3) solid solution by X-ray diffraction and microstructure analysis, and found the solubility limit of MgO in *c*-Y_2O_3 was 7 mol % at 2373 K. The eutectic reaction was established to be at 50 mol % of MgO and 2383 K. In the present study, the thermodynamic modeling of the present system was conducted based on these experimental data by Tresvyatsky et al.[42].

4.2.3 Y_2O_3-YF_3 system

The present authors [5] performed the critical evaluation of all available phase diagram data [14-21] and thermodynamic data of YOF [12-14] in the literature. The present authors [5] also performed new phase diagram study up to 1973 K using DTA and classical quenching experiment. Based on the evaluated literature data and new phase diagram data, thermodynamic modeling of the Y_2O_3-YF_3 system was conducted to obtain the optimized thermodynamic Gibbs energies of all the phases within the system and calculate the overall phase diagram of the entire system [5].

Figure 4.1 shows the phase diagram of the Y_2O_3-YF_3 system. As can be seen, there are intermediate compounds, YOF and vernier phases ($Y_7O_6F_9$, and $Y_4O_3F_6$), stable above 1973 K. Mutual solubility between solid Y_2O_3 and YF_3 phases was also confirmed from experiments. The details can be found in reference [5].

4.2.4 MgF_2-YF_3 system

Nafziger et al.[43] and Olkhovaya et al.[44] employed XRD phase analysis and thermal analysis to obtain the phase diagram of the MgF_2-YF_3 system. No intermediate compound was found. Eutectic reaction between orthorhombic-YF_3 (*o*-YF_3) and MgF_2 occurs at 36 mol % of MgF_2 and 1237-1247 K. The solubility limit of MgF_2 in hexagonal-YF_3 (*h*-YF_3) solid solution was 6 mol % at 1333 K. In the present study, thermodynamic assessment of the MgF_2-YF_3 system was conducted based on these experimental data.

4.2.5 MgO-MgF_2-Y_2O_3-YF_3 system

There has been no experimental phase diagram investigation on the Mg, Y // O, F reciprocal system.

4.3 Phase diagram experiments

4.3.1 Starting materials

Starting materials were made by mechanical mixing of pure Y_2O_3 (Sigma Aldrich; 99 wt.% purity), YF_3 (Alfa Aesar; > 99.99 wt.% purity), MgO (Sigma Aldrich; 99 wt.% purity), and MgF_2 (Sigma Aldrich; 99.9 wt% purity) powders. MgO powder was calcinated at 1000 K for 12 hr to remove absorbed carbon dioxide. The purities of all the powders were verified by Bruker D8 Advance multi-purpose XRD analyses in the Research Institute of Advanced Materials (RIAM) at Seoul National University (SNU). No foreign peaks which refer to contamination of the mixtures were detected. The mixtures were stored in C_6H_{12} cyclohexane to prevent moisture absorption and dried in a vacuum oven at 348 K before using them.

The starting materials were placed in sealed Pt capsules for heat treatment and differential thermal analysis (DTA). The Pt capsule is a Pt tube with 4 mm outer diameter, 1 mm wall thickness and ~10mm length. Each capsule carries about 15-20 mg of the powder mixtures and was sealed using a tungsten electrode. The vaporization of fluorides during annealing experiments can be avoided by using thick Pt tube and sealing Pt crucibles.

4.3.2 Differential thermal analysis (DTA)

Differential thermal analysis (DTA) was carried out with the NETSCH STA 449 F5 equipment. The thermocouples were calibrated via the melting and the polymorphic transition temperatures of standard materials as mentioned in section 3.3.2. A completely sealed Platinum capsule was used to carry the sample was placed in the DTA alumina crucible. The samples were heated and cooled with rates of 10 K/min twice in an argon atmosphere with 20 mL/min flow rate. Thermo-gravity analysis (TGA) was conducted to check the weight loss occurred by evaporation.

4.3.3 Quenching experiments

The quenching experiments were performed by using a vertical tube furnace equipped with $Pt_{30}Rh$-Pt_6Rh (type B) thermocouples. The furnace temperature was set within ± 3 K at the target temperature by using a PID controller. The samples in the sealed Pt capsules were hanged in an alumina tube with a Pt wire and heat treated at target temperature. The samples were then dropped and quenched in cold water. After quenching, the weight change of the samples was compared to ensure that there was no evaporation loss or hydration of the sample during the water quenching experiment. Chemical equilibrium was confirmed by homogeneity of each phase composition throughout the quenched sample.

4.3.4 Phase characterization

After annealing and quenching experiments, the samples were cast in epoxy resin and polished with diamond-based lapping oil. The samples were put in the cyclohexane to clean impurities using ultrasonication and carbon coated. Phase analysis was performed by JEOL-8530F electron probe microanalysis (EPMA) in the National Center for Inter-university Research Facilities (NCIRF) at SNU. The phase composition was analyzed by using a 15kV accelerating voltage and 10nA beam current. Beam diameters (1-3 μm and 10-20 μm) were set according to the size of each phase. MgO, $Y_3Al_5O_{12}$, $(Zr,Y)O_2$, and BaF_2 samples which were provided by NCIRF were employed as standards for the elemental composition of Mg, Y, O, and F, respectively. The samples were ground and analyzed by Bruker D8 Advance XRD using Cu-Kα source (λ = 1.54 Å). All peaks of the XRD scan were identified with powder diffraction files (PDF) from the International Center for Diffraction Data using Bruker AXS DIFFRAC.EVA software.

4.4 Thermodynamic models

4.4.1 Stoichiometric compounds

The Gibbs energy of a stoichiometric compound is represented as follows:

$$G_T^o = H_T^o - TS_T^o \qquad (1)$$

$$H_T^o = \Delta H_{298.15\,K}^o + \int_{298.15\,K}^{T} C_p dT \qquad (2)$$

$$S_T^o = S_{298.15\,K}^o + \int_{298.15K}^{T} \frac{C_p}{T} dT \qquad (3)$$

where $\Delta H_{298.15\,K}^o$ is the standard enthalpy of formation at 298.15K, $S_{298.15\,K}^o$ is the standard entropy at 298.15 K, and C_p is the heat capacity of a compound that is temperature dependent.

The present study obtained the Gibbs energies of solid cubic, hexagonal, and liquid Y_2O_3 from a prior research of rare earth oxides by our group. [26] The Gibbs energies of solid orthorhombic, hexagonal, and liquid YF_3 were obtained from the FactSage FactPS database[15, 16], which was compiled using Barin's thermodynamic data. [27] The Gibbs energies of solid cubic and liquid MgO and solid tetragonal and liquid MgF_2 were also taken from the FactSage FactPS database[1, 15, 16] derived from Berman and Brown [45] and JANAF thermochemical tables, respectively. The Gibbs energies of YOF and vernier phases were taken from Baek and Jung. [5]

4.4.2 Liquid solution

The molten oxy-fluoride solution with two sublattice quadruplet approximation was described using the Modified Quasichemical Model (MQM) [3], which considers first-nearest-neighbor (FNN) short range ordering (SRO) between sublattices and second-nearest-neighbor (SNN) SRO within a sublattice. The molten oxy-fluoride is made up of the following two sublattices : (Y^{3+}, Mg^{2+})[O^{2-}, F^{-}]. This reciprocal ionic system is presented in Figure 4.2 by a schematic composition square. The following two reactions are crucial in describing the model.

(i) The exchange reaction among the pure liquid components

: $Y_2O_3(l) + 3MgF_2(l) = 2YF_3(l) + 3MgO(l); \ \ \Delta g_{YMg/OF}^{exchange}$ (4)

The first-nearest-neighbor (FNN) cation-anion short-range-ordering (SRO) in the oxy-fluoride melts is determined by this equation.

(ii) The second-nearest-neighbor (SNN) pair exchange reactions between cations and between anions.

$(Y - O - Y) + (Mg - O - Mg) = 2(Y - O - Mg)\ ;\ \Delta g_{YMg/OO}$ (5)

$(Y - F - Y) + (Mg - F - Mg) = 2(Y - F - Mg)\ ;\ \Delta g_{YMg/FF}$ (6)

$(O - Y - O) + (F - Y - F) = 2(O - Y - F)\ ;\ \Delta g_{YY/OF}$ (7)

$(O - Mg - O) + (F - Mg - F) = 2(O - Mg - F)\ ;\ \Delta g_{MgMg/OF}$ (8)

The second-nearest-neighbor (SNN) SRO between cations (equation (5) and (6)) and anions (equation (7) and (8)) is explained by the equation above.

The thermodynamic modeling must account for the coupling of the FNN SRO and SNN SRO and the detailed mathematical explanation of the model can be found in Pelton et al.[3] The Gibbs energy of the solution can be expressed as below:

$G = (n_{YY/OO}g_{YY/OO} + n_{MgMg/OO}g_{MgMg/OO} + n_{YY/FF}g_{YY/FF} + n_{MgMg/FF}g_{MgMg/FF}) +$

$(n_{YMg/OO}g_{YMg/OO} + n_{YMg/FF}g_{YMg/FF} + n_{YY/OF}g_{YY/OF} + n_{MgMg/OF}g_{MgMg/OF}) +$

$n_{YMg/OF}g_{YMg/OF} - T\Delta S^{config}$ (9)

where $n_{ij/kl}$ and $g_{ij/kl}$ are the number of moles and the molar Gibbs energy of the ij/kl quadruplets, respectively. ΔS^{config} is the configurational entropy of mixing obtained by randomly distributing the quadruplets over the sublattices.

To describe the structure of melt, the FNN and SNN coordination numbers of each cation and anion are assigned. In the present study, the coordination number of each ion in the oxy-fluoride solution was considered to be same as in the oxide solution. The SNN coordination numbers of Y^{3+}, Mg^{2+}, O^{2-}, and F^{-} were set to be 2.066, 1.377, 1.377, and 0.689, respectively, to keep the consistency with the previous study.

The Gibbs energies of unary quadruplets (Y_2O_3, MgO, YF_3, and MgF_2) at the four corners of the square in Figure 4.2 are derived from that of pure liquid oxides and fluorides.

$$g_{YY/OO} = \left(\frac{2}{Z_Y}\right) g^o_{YO_{1.5}},\ g_{YY/FF} = \left(\frac{2}{Z_Y}\right) g^o_{YF_3},\ g_{MgMg/OO} = \left(\frac{2}{Z_{Mg}}\right) g^o_{MgO},\ g_{MgMg/FF} = \left(\frac{2}{Z_{Mg}}\right) g^o_{MgF_2} \quad (10)$$

where Z_i is the SNN coordination number of i cation and g^o_j is the standard molar Gibbs energy of pure liquid j. The Gibbs energies of the binary quadruplets ($g_{YMg/OO}$, $g_{YMg/FF}$, $g_{YY/OF}$, and $g_{MgMg/OF}$) at the edge of the square in Figure 4.2 are calculated using the Gibbs energies of the SNN pair exchange reaction in the binary system. For example, in the Y_2O_3-YF_3 system:

$(YY/OO) + (YY/FF) = 2(YY/OF);\ \Delta g_{YY/OF}$ (11)

$2g_{YY/OF} = \Delta g_{YY/OF} + g_{YY/OO} + g_{YY/FF}$ (12)

where $\Delta g_{YY/OF}$ is an model parameter in paper[5] which can be functions of temperature. In the same way, the present study optimized all other SNN oxide pair exchange energies $\Delta g_{ij/kl}$. The Gibbs energy $g_{YMg/OF}$ which is in the center of Figure 4.2 is equal to the the weighted average of $g_{YMg/OO}$, $g_{YMg/FF}$, $g_{YY/OF}$, and $g_{MgMg/OF}$ as specified in Pelton et al.[3] The details of the MQM can be found elsewhere. [2, 3]

4.4.3 Solid solutions

Cubic-Y_2O_3 (*c*-Y_2O_3) and hexagonal-Y_2O_3 (*h*-Y_2O_3) which is stabilized by YF_3 and MgO, and hexagonal-YF_3 (*h*-YF_3) which is stabilized by Y_2O_3 and MgF_2 are the solid solutions that have been determined in the MgO-MgF_2-Y_2O_3-YF_3 system.

4.4.3.1 Cubic-Y_2O_3 and hexagonal-Y_2O_3 solutions

The unit cell of Y_2O_3 bixbyite structure includes two Y atoms in the center of cubic cells (8b and 24d), 12 oxygen atoms on the corners, and four vacancies (Va) on the corners as indicated in the previous study by the present authors.[5] They hypothesized that F replaces O and Va at both oxygen and vacancy sites so determined the Y_2O_3 solid solution to be $(Y^{3+})_2[O^{2-},F^-]_3^a[Va,F^-]_1^b$ where a and b represent oxygen and vacancy sites, respectively. To apply this sublattice structure to Y_2O_3 solution in the MgO-Y_2O_3 system, we consider that Mg can replace Y in the cation site and vacancy can also occupy oxygen site to keep charge neutrality. Thus, the Gibbs energy of the Y_2O_3 solid solution is defined using the three sublattice Compound Energy Formalism (CEF) with $(Y^{3+},Mg^{2+})_2^a[O^{2-},F^-,Va]_3^b[Va,F^-]_1^c$, where a, b, and c represent cation, oxygen and vacancy sites, respectively. The equation of the Gibbs energy of Y_2O_3 solution is described as below:

$$G^m = \sum_i \sum_j \sum_k y_i^a y_j^b\, y_k^c\, G_{ijk}^o + RT(\,2\sum_i y_i^a ln y_i^a + 3\sum_j y_j^b ln y_j^b \; + \; \sum_k y_k^c ln y_k^c) + g^{ex} \quad (13)$$

where y_i^a, y_j^b, and y_k^c are site fraction of i, j, and k in ‘a’, ‘b’, and ‘c’ sites, respectively, and g^{ex} is excess interaction parameter between species in each site. The Gibbs energies of the hypothetical end member, G_{ijk}^o are the main model parameters. In the present study, the Gibbs energy of end members associated to the Y_2O_3-YF_3 system were confirmed to be same as that of Baek and Jung. The Gibbs energy of $Mg_2Va_3Va_1$(4+) was assumed to be double that of metallic Mg. Then, the Gibbs energy of $Mg_2O_3Va_1$(2-) can be calculated using the charge neutrality to form MgO.

$$2G_{MgO}^o = \frac{2}{3}\, G_{Mg_2O_3Va_1(2-)}^o + \frac{1}{3}\, G_{Mg_2Va_3Va_1(4+)}^o\; 3RT\left(\frac{2}{3} ln\frac{2}{3} + \frac{1}{3} ln\frac{1}{3}\right) \quad (14)$$

The Gibbs energies of $Mg_2O_3F_1$ and $Mg_2Va_3F_1$ can be determined by the reciprocal relation as follows:

$$G_{Mg_2O_3F_1}^o + G_{Y_2O_3Va_1}^o = G_{Mg_2O_3Va_1}^o + G_{Y_2O_3F_1}^o \quad (15)$$

$$G_{Mg_2Va_3F_1}^o + G_{Mg_2O_3Va_1}^o = G_{Mg_2Va_3Va_1}^o + G_{Mg_2O_3F_1}^o \quad (16)$$

The Gibbs energies of $Mg_2F_3F_1$ and $Mg_2F_3Va_1$ can be determined by the Gibbs energy of MgF_2 and reciprocal relation as below:

$$G_{Mg_2F_3F_1}^o = 2G_{MgF_2}^o \quad (17)$$

$$G^{o}_{Mg_2F_3Va_1} + G^{o}_{Mg_2O_3F_1} = G^{o}_{Mg_2F_3F_1} + G^{o}_{Mg_2O_3Va_1} \quad (18)$$

G^{o}_{MgO} and $G^{o}_{MgF_2}$ were optimized reproduce the solubility of MgO in Y_2O_3 solid solutions and no g^{ex} was required.

4.4.3.2 Hexagonal-YF_3 solution

As explained in section 3.4.3.2, one sublattice random mixing model was used for h-YF_3 solution in the Y_2O_3-YF_3 system to reduce the mixing entropy and reproduce the experimental solubility of Y_2O_3 in YF_3 solution. To keep consistency with the previous study, the h-YF_3 solution in the MgF_2-YF_3 system was established to have one sublattice random mixing model using MgF_2 and YF_3 as solution species. The Gibbs energy of h-YF_3 solid solution is described as follows:

$$G^{m} = X_{YF_3}G^{o}_{YF_{3(H)}} + X_{YO_{1.5}}G^{o}_{YO_{1.5(H)}} + X_{MgF_2}G^{o}_{MgF_2} + RT\big(X_{YF_3}lnX_{YF_3} + X_{YO_{1.5}}lnX_{YO_{1.5}} + X_{MgF_2}lnX_{MgF_2}\big) + \sum_i \sum_j \sum_k q^{ijk}(X_{YF_3})^{i}(X_{YO_{1.5}})^{j}\,(X_{MgF_2})^{k} \quad (19)$$

where $G^{o}_{YF_{3(H)}}$, $G^{o}_{YO_{1.5\,(H)}}$, and $G^{o}_{MgF_2}$ are the molar Gibbs energy of h-YF_3, hypothetical $YO_{1.5}$, and MgF_2 with the same crystal structure as h-YF_3, respectively. The solubility was described using $G^{o}_{YO_{1.5\,(H)}}$, $G^{o}_{MgF_2}$, and q^{ijk}.

4.5 Experimental results and thermodynamic optimization

4.5.1 Binary systems

4.5.1.1 MgO-MgF_2 system

As reviewed in section 4.2.1, the MgO-MgF_2 system is a simple eutectic system. As there is still relatively large deviation in the eutectic temperature (1487 ~ 1503 K) between MgO and MgF_2 in the literature, new DTA experiment was conducted to confirm the eutectic temperature. A sample of 0.2 mol fraction MgF_2 was mixed and annealed at 1273 K for 3 hr to remove absorbed moisture. Then, the sample was sealed in Pt capsule and used for DTA experiment. The experimental result is plotted in Figure 4.3. The transition in heating cycles is recorded at 1494-1495 K, while a significant undercooling can be found in cooling cycles. Even, it is not presented here, we performed also the DTA experiment for the less dehydrated sample (sample without pre-annealing at 1273 K), and found transition temperature at 1487 K, noticeably lower than the dehydrated sample. Most probably, the moisture decreases the melting temperature of MgO-MgF_2 sample.

The calculated phase diagram of the MgO-MgF_2 system in the present study is plotted in Figure 4.4 (a) along with all the experimental data in the literature [39-42] and the present DTA data. The eutectic composition from the literature is at 8 to 10 mol % MgO, and no mutual solubility between MgO and MgF_2 has been reported. In the evaluation of the literature data, the results by Hinz and Kunth [11] was neglected because their eutectic temperature as well as their melting temperature of MgF_2 are much lower than other data. In fact, the melting temperature of MgF2 by Hinz and Kunth is 23 K lower than the reference value (1536 K) of the present study, which might happen due to the contamination of sample by moisture or carbonate ($Mg(OH)_2$ or $MgCO_3$). In the thermodynamic assessment, a small MQM parameter was optimized to reproduce the eutectic reaction and liquidus of MgF_2 within the experimental error range:

$$\Delta g_{MgMg/OF} = -4000\ (J/mol) \quad (20)$$

The eutectic reaction is calculated at 9.77 mol % of MgO and 1497 K. It should be noted that the liquid solution is very close to an ideal solution.

4.5.1.2 MgO-Y_2O_3 system

Figure 4.4 (b) shows the phase diagram of the MgO-Y_2O_3 system calculated in the present study along with all available experimental data by Tresvyatsky et al.[42] In order to reproduce the homogeneity range of c-Y_2O_3, the Gibbs energy of MgO in c-Y_2O_3 solution was optimized without any excess interaction parameter. The same Gibbs energy of MgO was applied for h-Y_2O_3. No solubility of Y_2O_3 in MgO was reported.

The MQM parameters for the liquid solution were optimized to reproduce liquidus, solidus and eutectic reaction in the system:

$$\Delta g_{MgY/OO} = 3000 + 41000 x_{YY}\ (J/mol) \quad (21)$$

All experimental data by Tresvyatsky et al.[42] are well reproduced in the present study using slightly positive MQM parameters. The eutectic point is calculated to be 51 mol % of MgO at 2402 K. The maximum solubility of MgO in Y_2O_3 is calculated to be 5.96 mol % MgO at the eutectic temperature.

4.5.1.3 Y_2O_3-YF_3 system

As mentioned above in section 3.3, the present binary system was already thermodynamically assessed by the present authors [5]. The same model parameters were adopted without any change.

4.5.1.4 MgF_2-YF_3 system

The phase diagram of the MgF_2-YF_3 system calculated from the present thermodynamic modeling study is presented in Fig. 4 (c) along with the experimental data by Nafziger et al.[43] and Olkhovaya et al.[44] The h-YF_3 solid solution dissolving MgF_2 was described by one sublattice random mixing model. The maximum solubility of MgF_2 in h-YF_3 was calculated to be 2.70 mol % at 1339 K which represents the metatectic temperature. Solid MgF_2 and o-YF_3 are stoichiometric compound in this system. The MQM parameters were optimized to reproduce the liquidus and the eutectic reaction between o-YF_3 and MgF_2.

$$\Delta g_{MgY/FF} = 14399 - 13.986T - 5000\, x_{YY}\ (J/mol) \quad (22)$$

In order to reproduce the experimental phase diagram data within an error range, temperature dependent term was necessary. The eutectic point is calculated from the present optimization to be 62.90 mol % at 1253 K.

4.5.2 Mg, Y // O, F reciprocal system

4.5.2.1 Equilibrium quenching experiments

The sample of 0.69 MgO and 0.31 YF_3 in mol fraction was annealed at 1273 K for 45 hr (sample #4) to confirm the existence of any ternary solid phase. As can be seen in Figure 4.5 (a), solid YOF and MgF_2 phases were observed. Although no MgO phase was analyzed in EPMA microstructure analysis, the existence of MgO, MgF_2, and YOF phases were confirmed by XRD analysis. The mixtures with the same composition were annealed at 1573, 1673, and 1773 K (samples #5 to 7) to confirm the eutectic point. Figure 4.5 (b) shows the microstructure of the sample #6 equilibrated at 1673 K which containing well-developed MgO, YOF and liquid phase. EPMA composition analysis of the samples #5 to 7 confirmed the existence of MgO, YOF, and liquid phases. The composition of the liquid phase in all three samples located on the line between YOF and MgF_2, and did not vary significantly with temperature. In all cases, the maximum solubility of Mg in YOF was about 1.0 wt.%. Similarly, the samples with the composition of 0.93 MgO-0.07 YF_3 (sample #1 to 3) and 0.43MgO-0.43MgF_2-0.14YF_3 (sample #8 to 10) in mol fraction were annealed at 1573, 1673, and 1773 K to get more reliable liquidus information from 1573 K to 1773 K. Figures 4.5 (c) and (d) show the microstructures of the samples #3 and #9, respectively. In these samples, as seen in the microstructures, quenched crystals were readily formed so it was difficult to analyze the composition of liquid phase. To obtain the composition of liquid phase even roughly, the EPMA beam size was increased to 10-20 μm to detect the average composition including quenched crystals. Due to the inhomogeneous distribution of quenched crystals, the error in EPMA analysis for liquid phase region was even larger than 5 wt.% for Y and F. Nevertheless, the analyses can constrain the location of the liquid co-saturated with YOF and

MgO.

The sample of 0.29 MgO-0.14 MgF_2-0.57 YF_3 in mol fraction was annealed at 1273 K for 36 hr (sample #11) and showed the existence of MgF_2, $Y_4O_3F_6$, and liquid phase as shown in Figure 4.5 (e). The compositions of both $Y_4O_3F_6$ and liquid were well determined. The samples with same composition were annealed at 1573, 1673, and 1773 K (sample #12 to 14) to determine the liquidus at each temperature. The microstructure of the sample #14 is shown in Figure 4.5 (f). The quenched crystals (a mixture of $Y_4O_3F_6$, YF_3 and MgF_2) were formed in the liquid phase region. The large beam size was again employed to roughly determine the original liquid composition.

Fig. 6 (a)-(d) show the reciprocal phase diagram calculated at 1273, 1573, 1673, and 1773 K, respectively. Binary interaction parameters between MgF_2 and YF_3 was optimized to reproduce the experimental result. The temperature dependent term was used in the equation (23) to reproduce experimental results of both binary and reciprocal system. Reciprocal interaction parameter was also employed and it will be discussed in section 4.5.2.3.

4.5.2.2 Differential thermal analysis (DTA) results

It is crucial to determine the exact eutectic reactions in the reciprocal system to represent the reliable phase diagram. Thus, DTA was conducted for the samples with the composition of 0.5YF_3-0.5MgF_2-0.02MgO and 0.8MgF_2-0.2MgO-0.033YOF in mol fraction. These two compositions were intentionally selected considering the pseudo-binary YOF-MgF_2 system; as can be seen in Y_2O_3-YF_3 system, YOF is congruent melting compound, and therefore

YOF-MgF_2 can form pseudo-binary section. The first DTA sample composition was designed to determine the eutectic reaction in the YOF-YF_3-MgF_2 system, and the other sample was in the YOF-MgO-MgF_2 system.

The DTA result of the 0.5YF_3-0.5MgF_2-0.02MgO sample showed two transition peaks, as shown in Figure 4.7 (a). The strong transition peak was recorded at 1245-1247 K which is just about 10 K below the eutectic temperature (1253 K) in the binary MgF_2-YF_3 system. Therefore, this seems to be an eutectic reaction temperature in the YOF-YF_3-MgF_2 system near 0.5YF_3-0.5MgF_2 binary side. The second transition peak was barely identified in the heating curves (a rather pro-longed and broad peak, instead of a sharp peak), while a strong peak was recorded in the cooling curves. This second peak was difficult to analyze, but it would most probably correspond to the liquidus of the sample judged from its broad peak shape. Figure 4.7 (b) shows the DTA result of the 0.8MgF_2-0.2MgO-0.033YOF sample, which includes two overlapped transition peaks. To identify the phase transition involved in two transition peaks, equilibrium experiment was conducted for the sample at 1473 K for 70 hr, and its microstructure showed three phase assemblage of ‘MgO + MgF_2 + Liquid’ (see Figure 4.8). The first transition at 1459 K seems to be the eutectic reaction of ‘Liquid → MgO + MgF_2 + YOF’, and the second transition at 1498 K (peak temperature in the heating curves and end point in the cooling curves) seems to be the liquidus of the sample.

4.5.2.3 Thermodynamic optimization

Thermodynamic modeling of the reciprocal system was performed based on the present phase diagram experimental data. In the present study, no reciprocal solid phase was confirmed in the system. Y_2O_3 and YF_3 solid solution exist in the binary systems. Other compounds like YOF, MgO, MgF_2, and vernier phases can be assumed to be stoichiometric compounds because no noticeable dissolutions of foreign elements were detected for these solid phases in the EPMA of the quenched samples. Therefore, the thermodynamic description of each solid phase from binary system can be directly used in the reciprocal system. Based on the binary optimization results, in the MgO-MgF_2-Y_2O_3-YF_3 system.

The Gibbs energy of the reciprocal liquid solution can be predicted directly from binary liquid parameters using the Modified Quasichemical Model. Without any additional parameters in liquid solution, the phase diagram was calculated and compared with the experimental data in the present study. In general, the agreement with experimental data was reasonable but a certain improvement was necessary to improve the accuracy of the calculated phase diagram at 1273, 1573, 1673, and 1773 K and eutectic reactions.

The comparison between the experimental data and calculated phase diagram is shown in Figure 4.6. All the experimental iso-thermal liquidus data are well reproduced within the experimental error limits. For this, a small reciprocal parameter was introduced:

$$\Delta g_{YMg/OF} = -48316 + 25.559T \ \ (J/mol) \qquad (23)$$

The liquidus projections of the reciprocal system is predicted from the present thermodynamic description and presented in Figure 4.9. All the invariant reactions of the reciprocal system are summarized in Table 4. Two eutectic reactions are calculated and well consistent with the DTA experimental data in the present study.

$$L \rightarrow YF_3 + MgF_2 + Y_4O_3F_6 \text{ at } 1246\text{ K} \qquad (24)$$

$$L \rightarrow YOF + MgO + MgF_2 \text{ at } 1460\text{ K} \qquad (25)$$

In addition, the following eutectic reaction was predicted from the present thermodynamic modeling.

$$L \rightarrow MgO + Y_2O_3 + YOF \text{ at } 2041 \text{ K} \qquad (26)$$

The phase diagrams of two isopleths are calculated in Figure 4.10 from the present thermodynamic models with optimized parameters. The pseudo-binary YOF-MgF_2 system is a simple eutectic system with eutectic temperature of 1475 K, as shown in Figure 4.10 (a). The phase diagram of the Y_2O_3-MgF_2 isopleth is more complex, as shown in Figure 4.10 (b). YOF phase can be formed as a preliminary phase in the MgF_2 rich region.

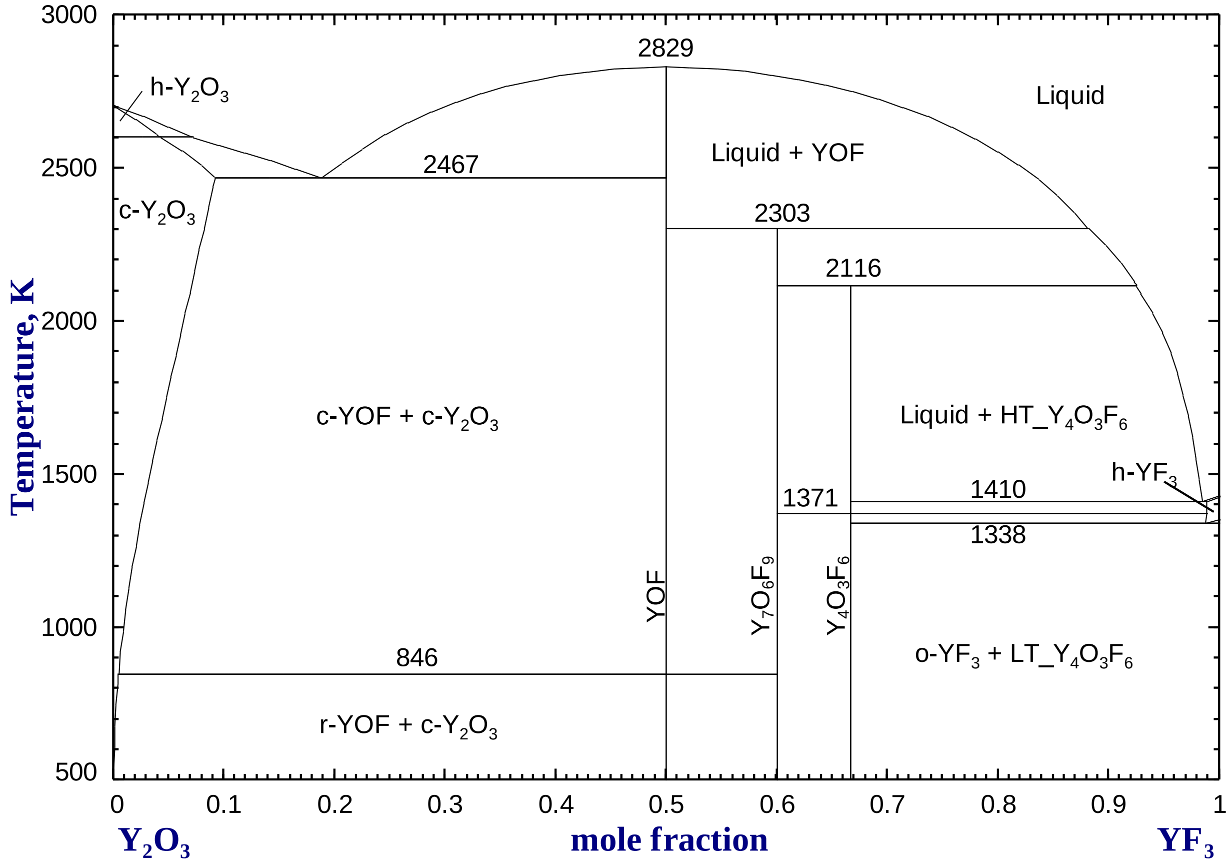

Figure 4.1 Phase diagram of the Y_2O_3-YF_3 system calculated from the thermodynamic assessment by Baek and Jung [5].

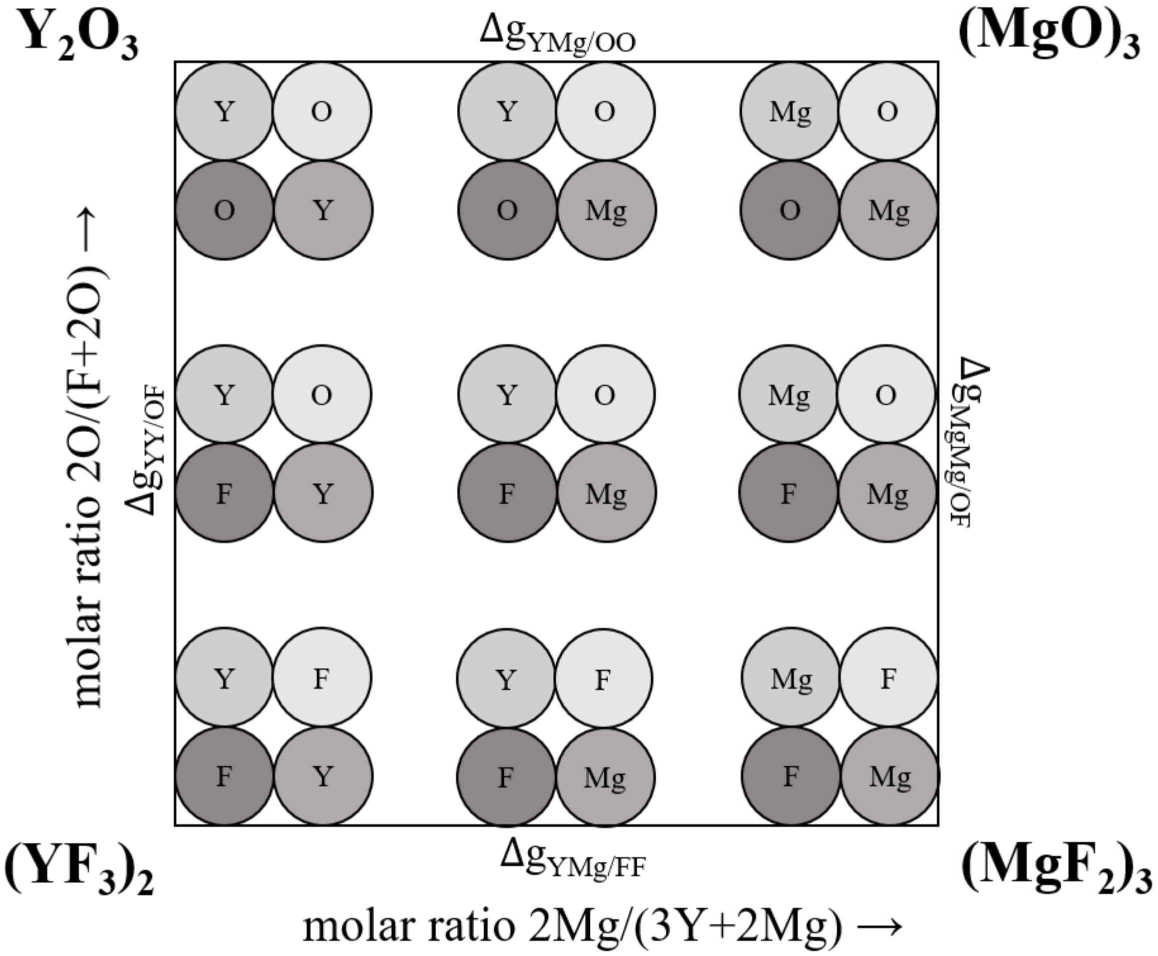

Figure 4.2 Schematic representation of the quadruplets in the MgO-MgF_2-Y_2O_3-YF_3 melt for the Modified Quasichemical Model.

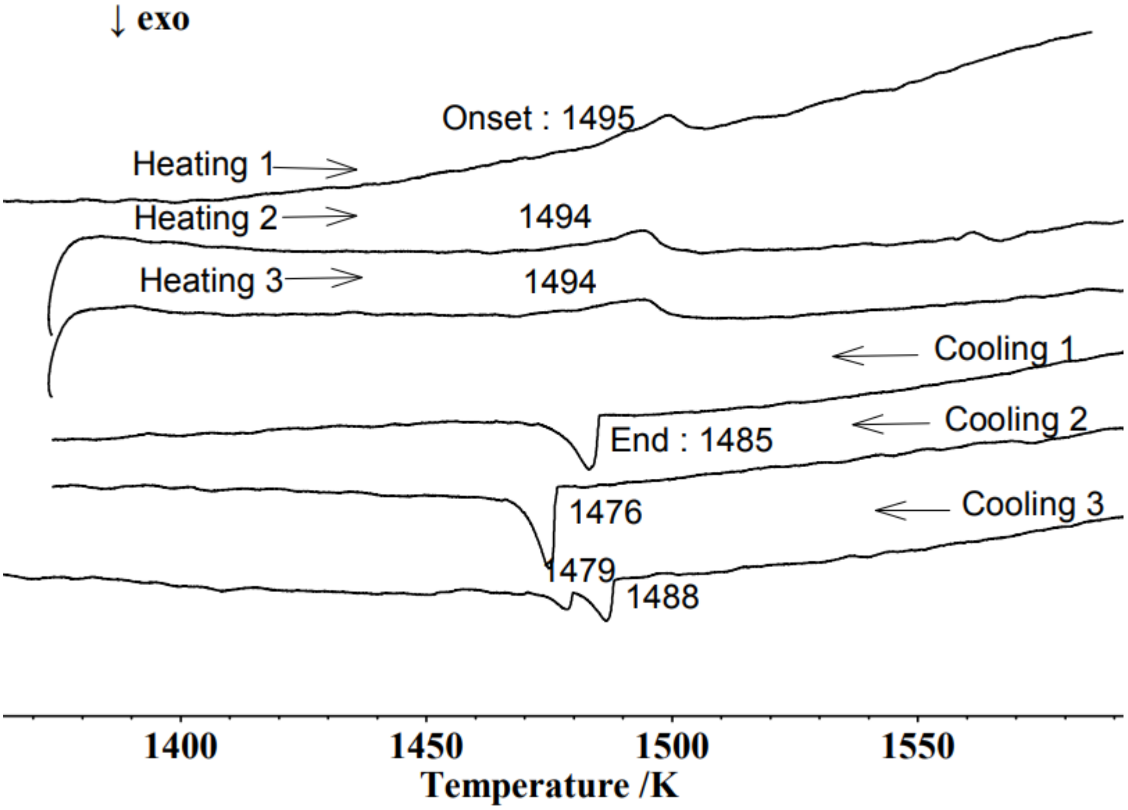

Figure 4.3 DTA results for the MgO-MgF_2 sample with 0.8 mol fraction MgO.

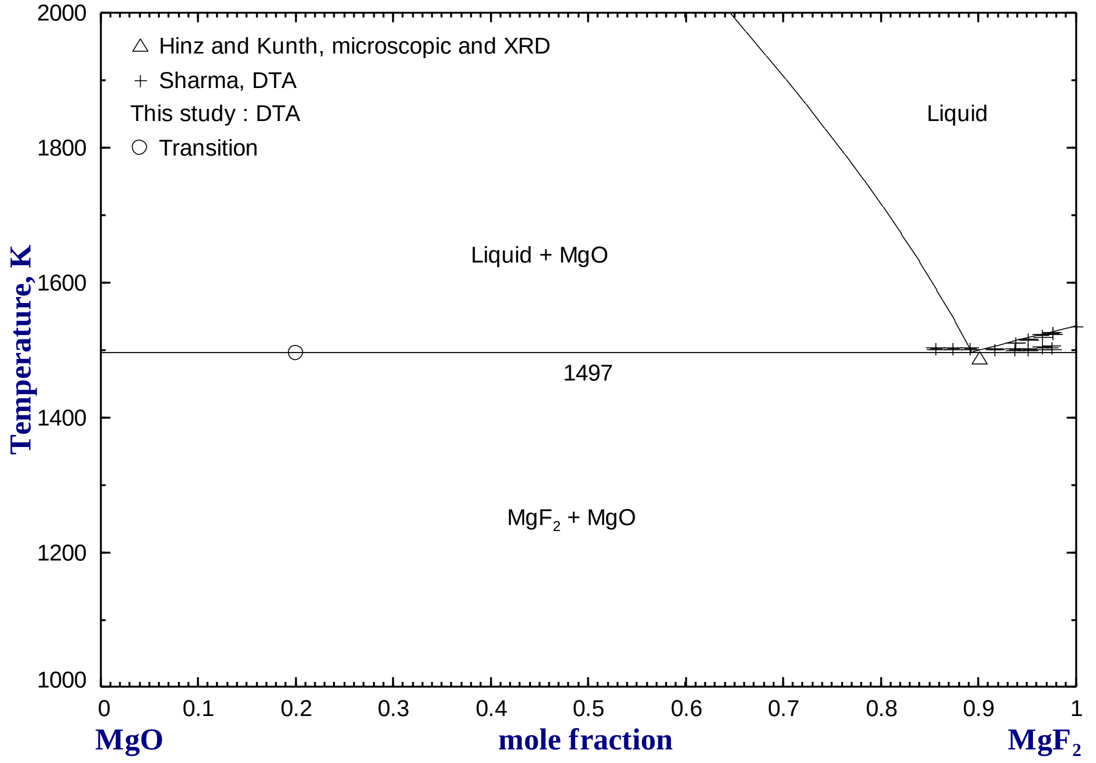
△ Hinz and Kunth, microscopic and XRD
+ Sharma, DTA
This study : DTA
○ Transition
Liquid
Liquid + MgO
1497
MgF_2 + MgO
Temperature, K
2000
1800
1600
1400
1200
1000
0
0.1
0.2
0.3
0.4
0.5
0.6
0.7
0.8
0.9
1
MgO
mole fraction
MgF_2

(a)

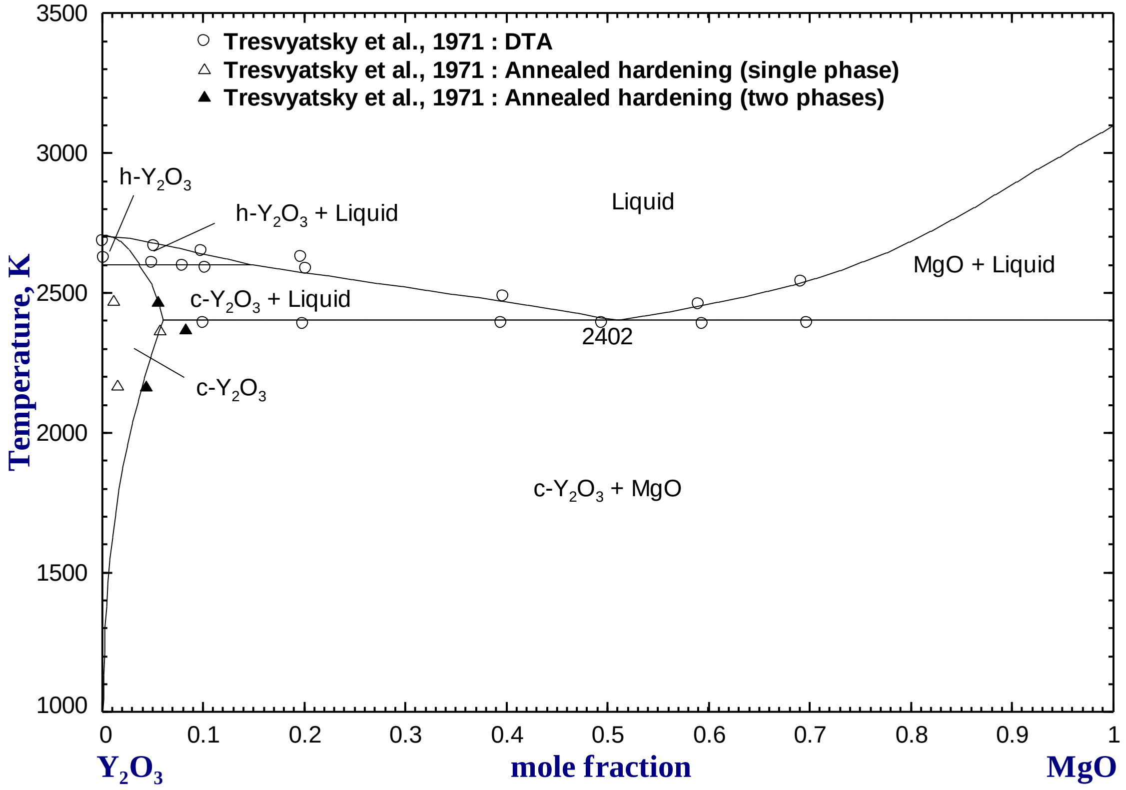
○ Tresvyatsky et al., 1971 : DTA
△ Tresvyatsky et al., 1971 : Annealed hardening (single phase)
▲ Tresvyatsky et al., 1971 : Annealed hardening (two phases)
h-Y_2O_3
h-Y_2O_3 + Liquid
Liquid
MgO + Liquid
c-Y_2O_3 + Liquid
2402
c-Y_2O_3
c-Y_2O_3 + MgO
Temperature, K
3500
3000
2500
2000
1500
1000
0
0.1
0.2
0.3
0.4
0.5
0.6
0.7
0.8
0.9
1
Y_2O_3
mole fraction
MgO

(b)

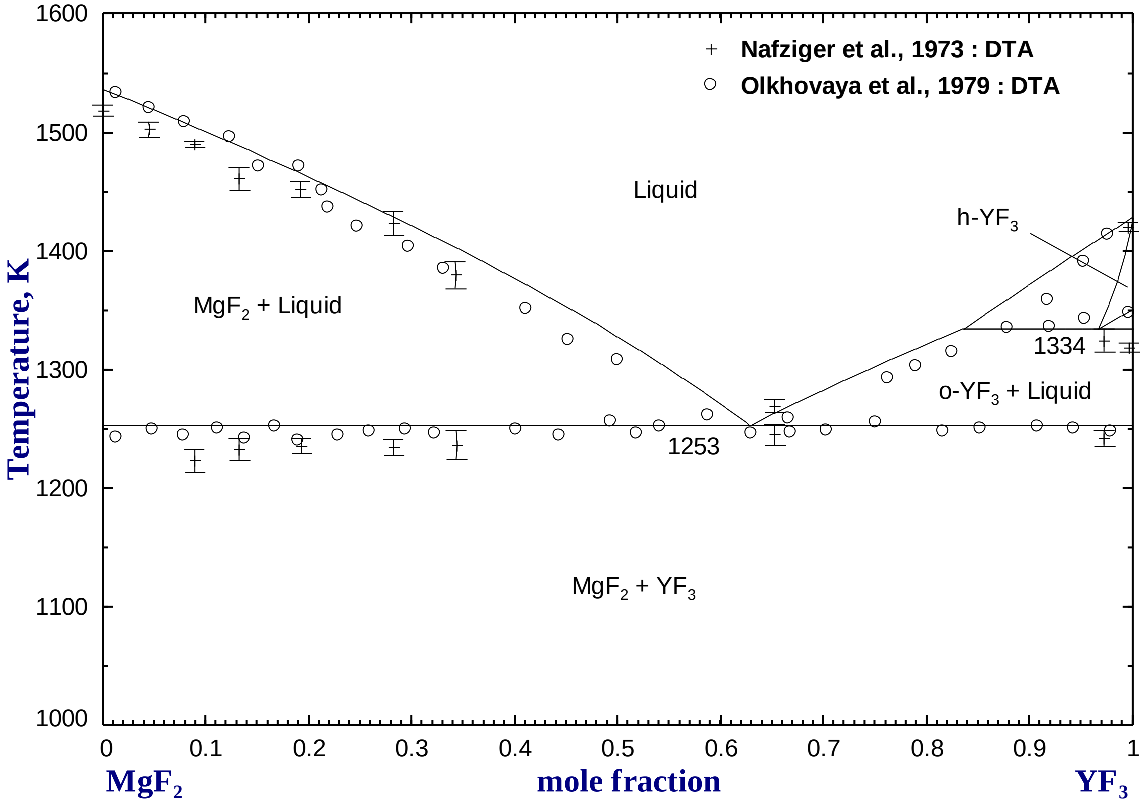

(c)

Figure 4.4 Phase diagrams of the binary systems calculated from the present thermodynamic optimization. (a) MgO-MgF_2, (b) MgO-Y_2O_3 and (c) MgF_2-YF_3.

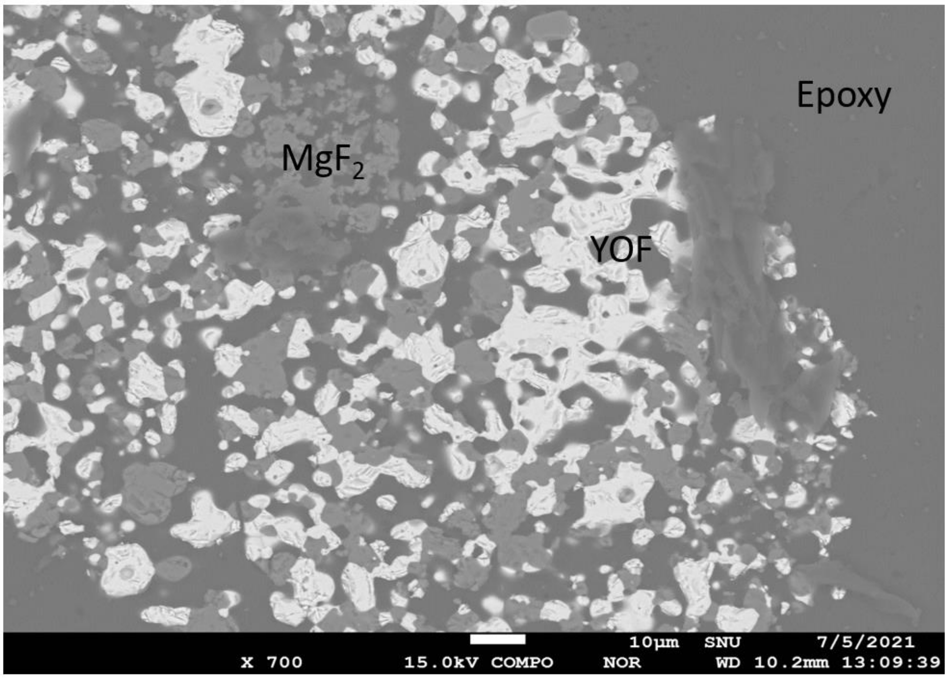
Epoxy
MgF_2
YOF
10µm SNU 7/5/2021
X 700 15.0kV COMPO NOR WD 10.2mm 13:09:39

(a)

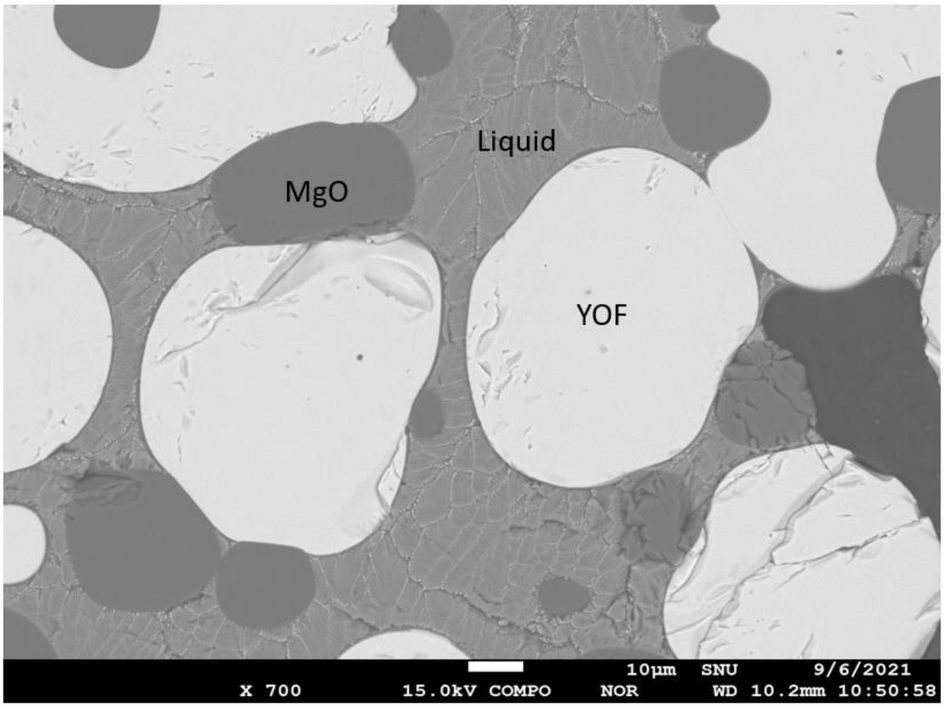
Liquid
MgO
YOF
10µm SNU 9/6/2021
X 700 15.0kV COMPO NOR WD 10.2mm 10:50:58

(b)

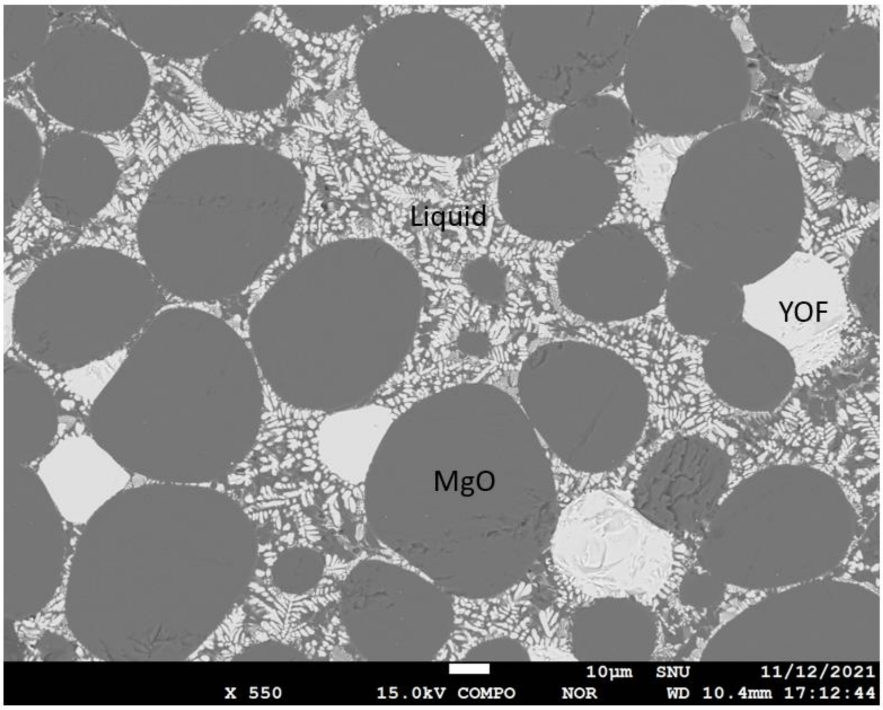
Liquid
YOF
MgO
10µm SNU 11/12/2021
X 550 15.0kV COMPO NOR WD 10.4mm 17:12:44

(c)

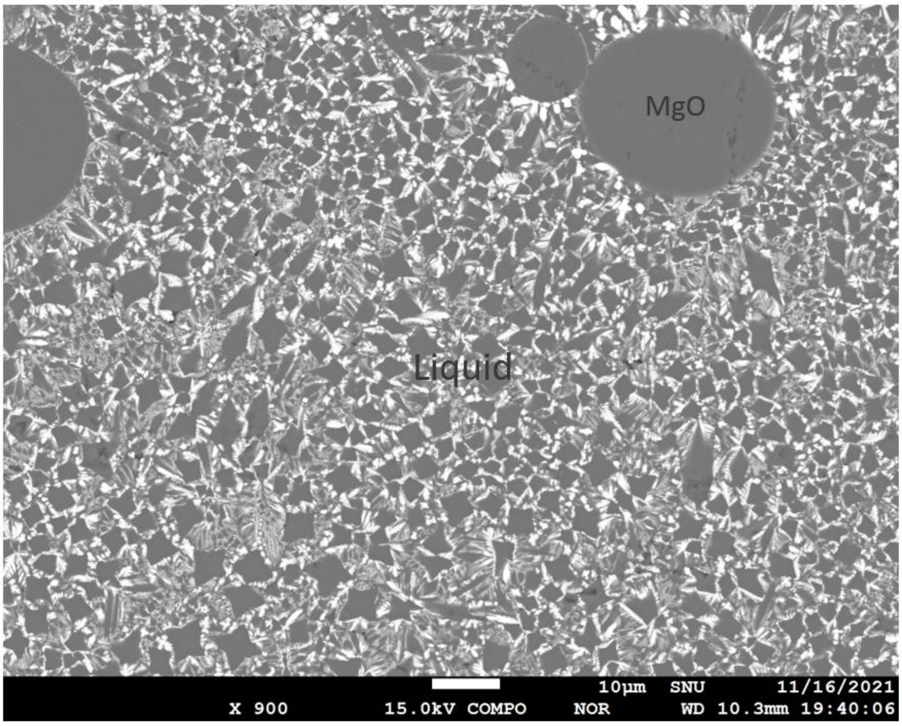
MgO
Liquid
10µm SNU 11/16/2021
X 900 15.0kV COMPO NOR WD 10.3mm 19:40:06

(d)

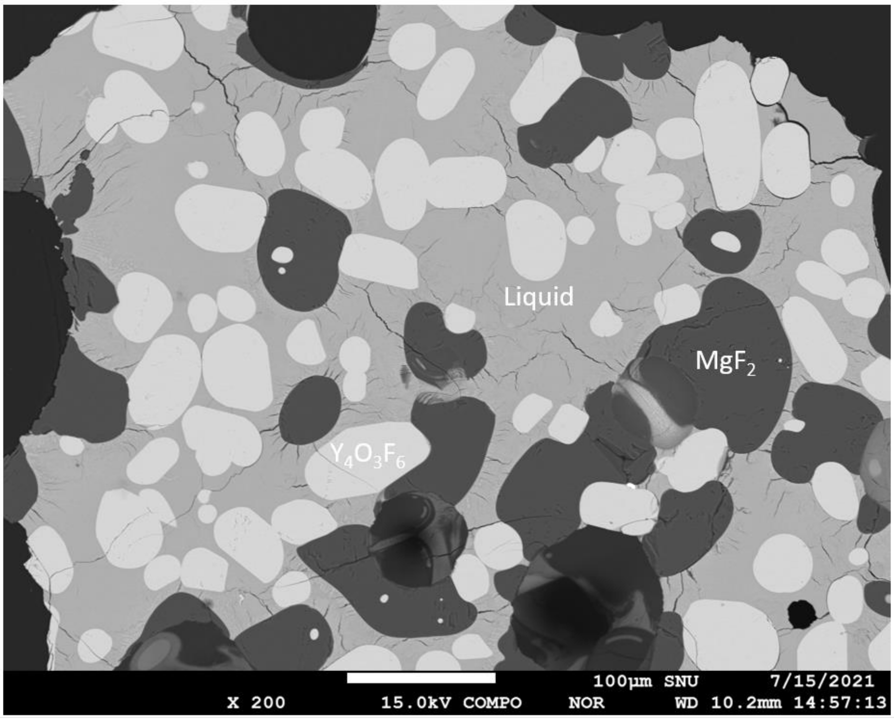

(e)

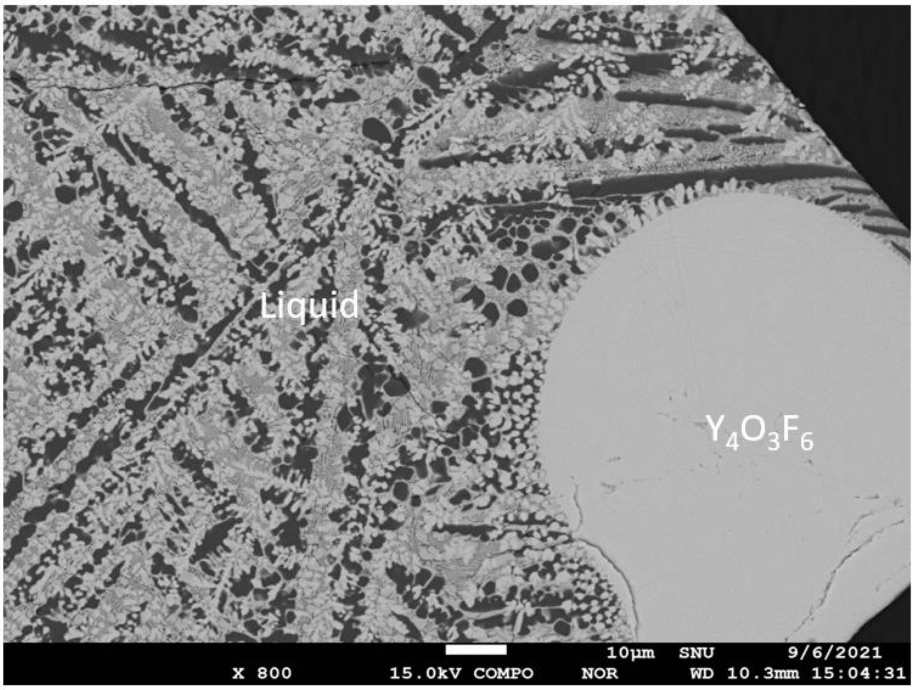

(f)

Figure 4.5 EPMA BSE image of the quenched sample (a) sample #4, (b) #6, (c) #3, (d) #9, (e) 11, and (f) #14.

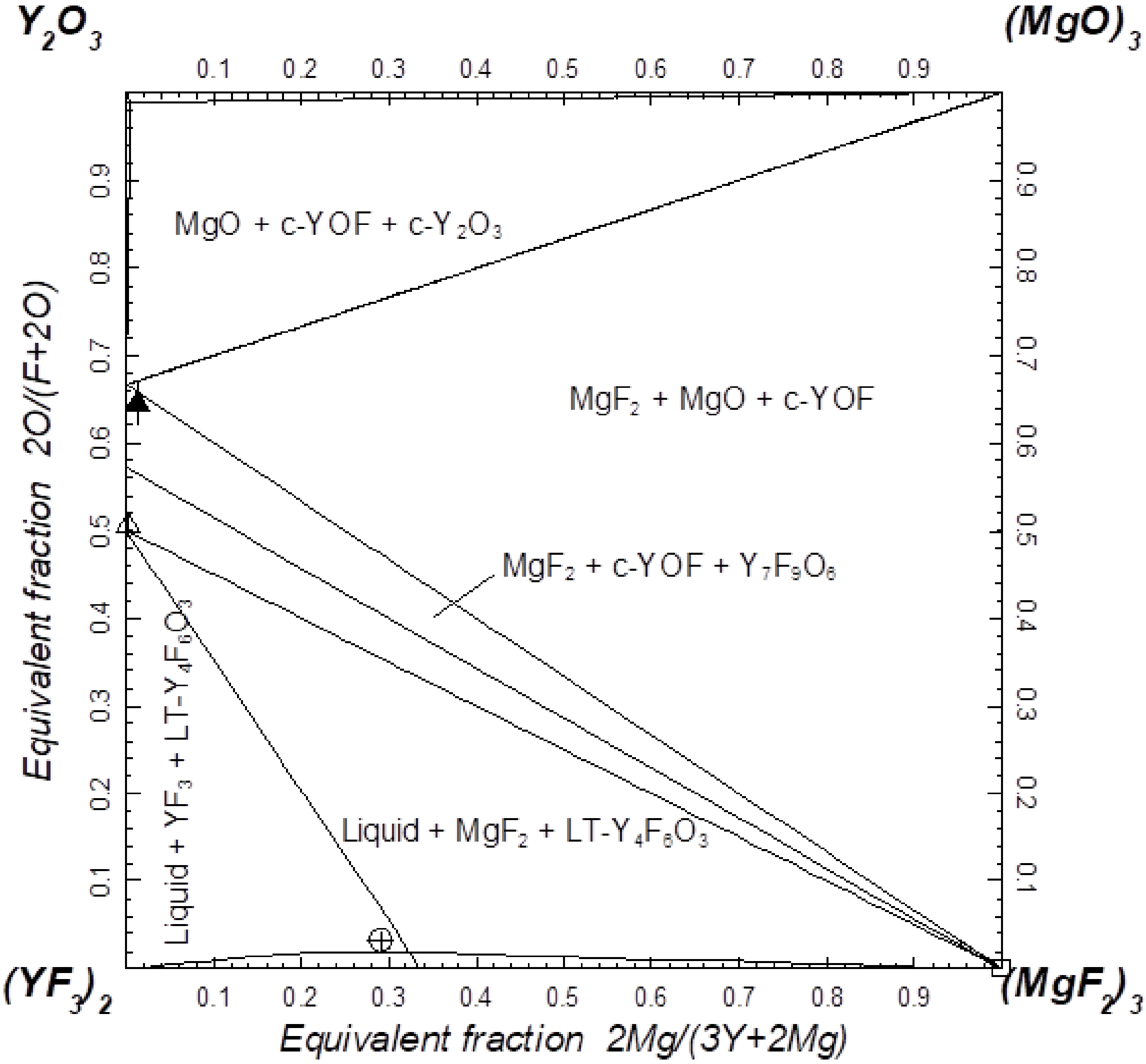
Y_2O_3
$(MgO)_3$
$(YF_3)_2$
$(MgF_2)_3$
0.1
0.2
0.3
0.4
0.5
0.6
0.7
0.8
0.9
Equivalent fraction 2O/(F+2O)
Equivalent fraction 2Mg/(3Y+2Mg)
MgO + c-YOF + c-Y_2O_3
MgF_2 + MgO + c-YOF
MgF_2 + c-YOF + $Y_7F_9O_6$
Liquid + MgF_2 + LT-$Y_4F_6O_3$
Liquid + YF_3 + LT-$Y_4F_6O_3$

(a)

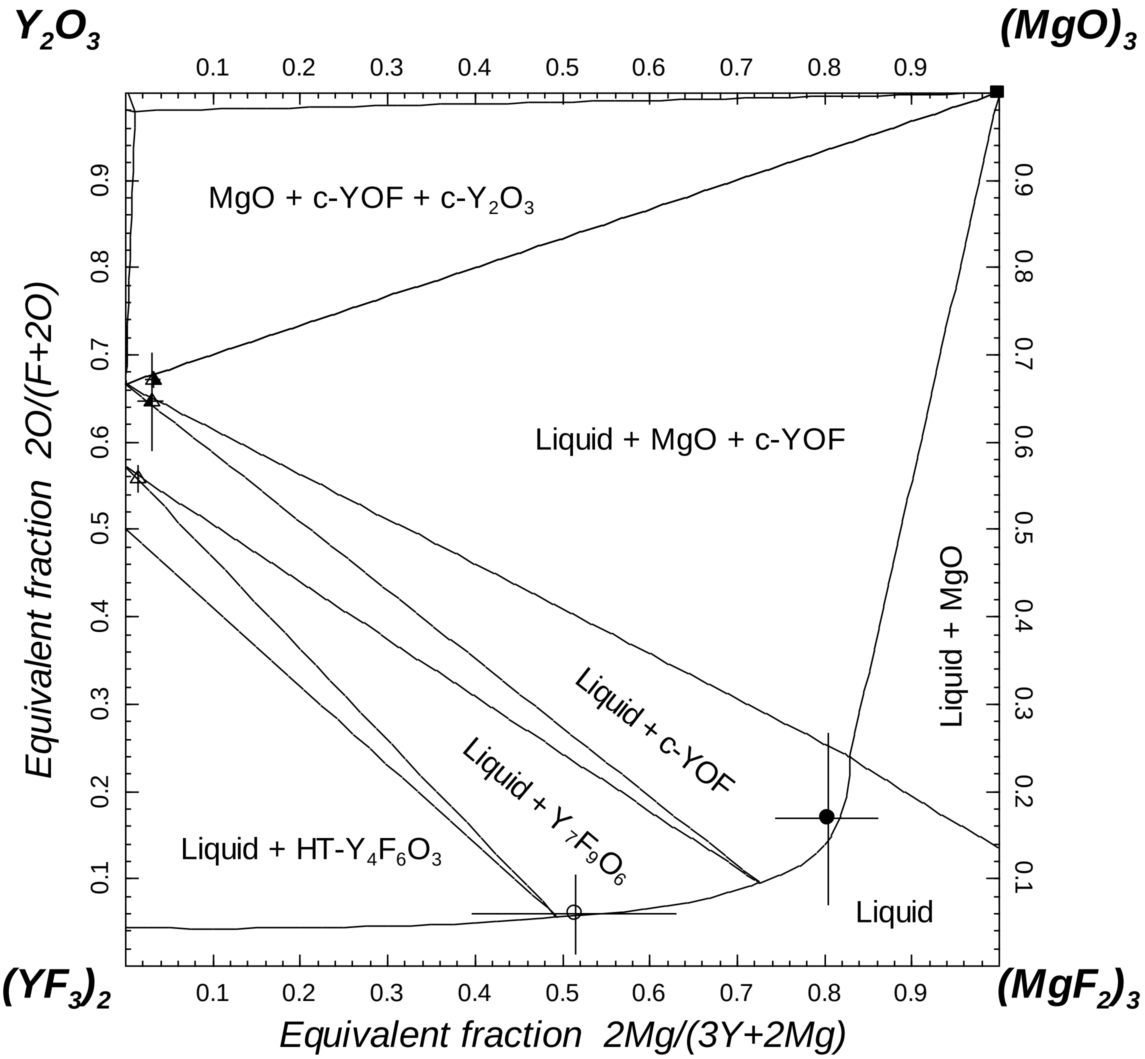

Y_2O_3
$(MgO)_3$
$(YF_3)_2$
$(MgF_2)_3$
0.1
0.2
0.3
0.4
0.5
0.6
0.7
0.8
0.9
Equivalent fraction 2O/(F+2O)
Equivalent fraction 2Mg/(3Y+2Mg)
MgO + c-YOF + c-Y_2O_3
Liquid + MgO + c-YOF
Liquid + MgO
Liquid + c-YOF
Liquid + $Y_7F_9O_6$
Liquid + HT-$Y_4F_6O_3$
Liquid

(b)

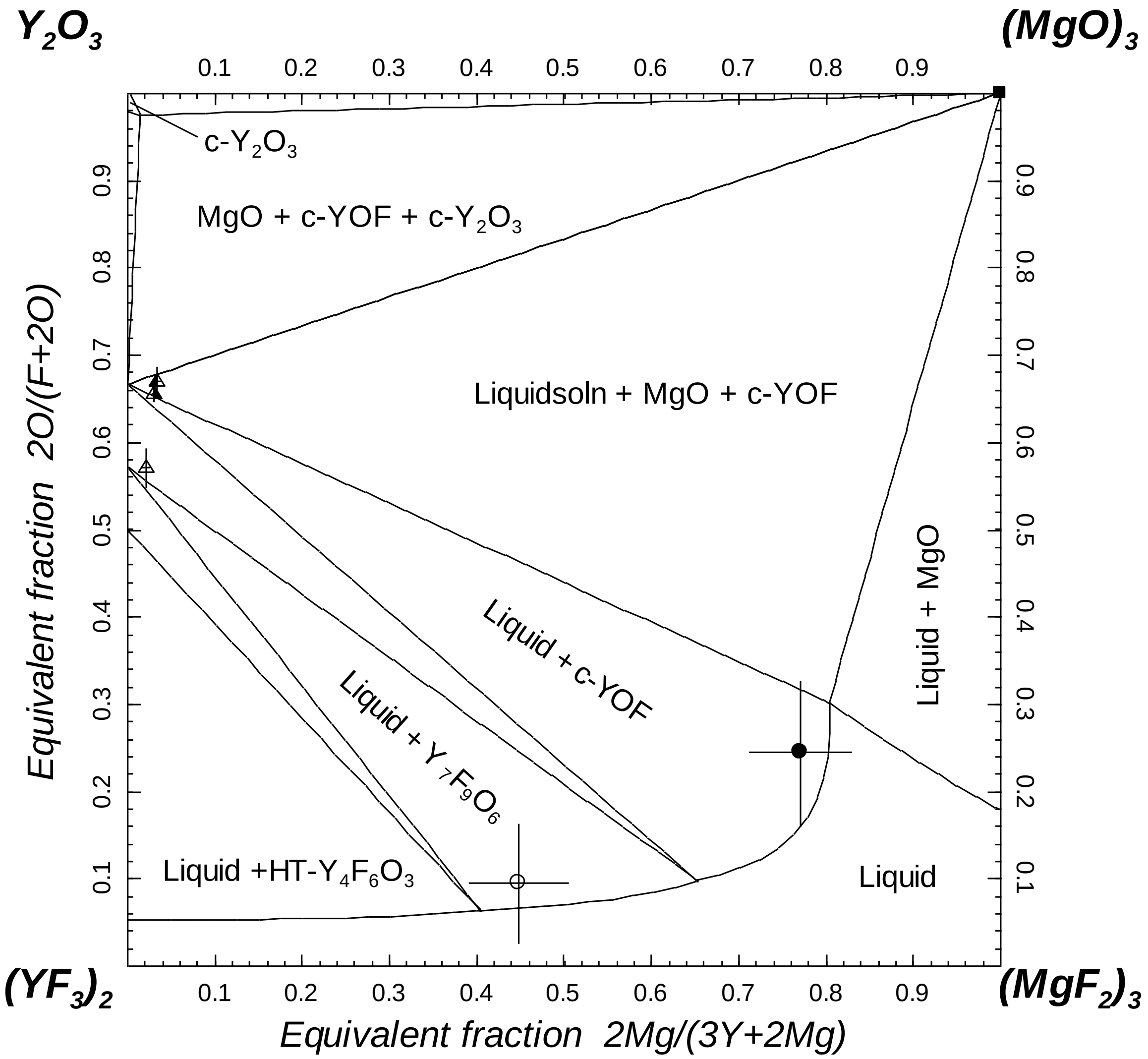

Y_2O_3
$(MgO)_3$
$(YF_3)_2$
$(MgF_2)_3$
0.1
0.2
0.3
0.4
0.5
0.6
0.7
0.8
0.9
c-Y_2O_3
MgO + c-YOF + c-Y_2O_3
Liquidsoln + MgO + c-YOF
Liquid + c-YOF
Liquid + $Y_7F_9O_6$
Liquid + MgO
Liquid +HT-$Y_4F_6O_3$
Liquid
Equivalent fraction 2O/(F+2O)
Equivalent fraction 2Mg/(3Y+2Mg)

(c)

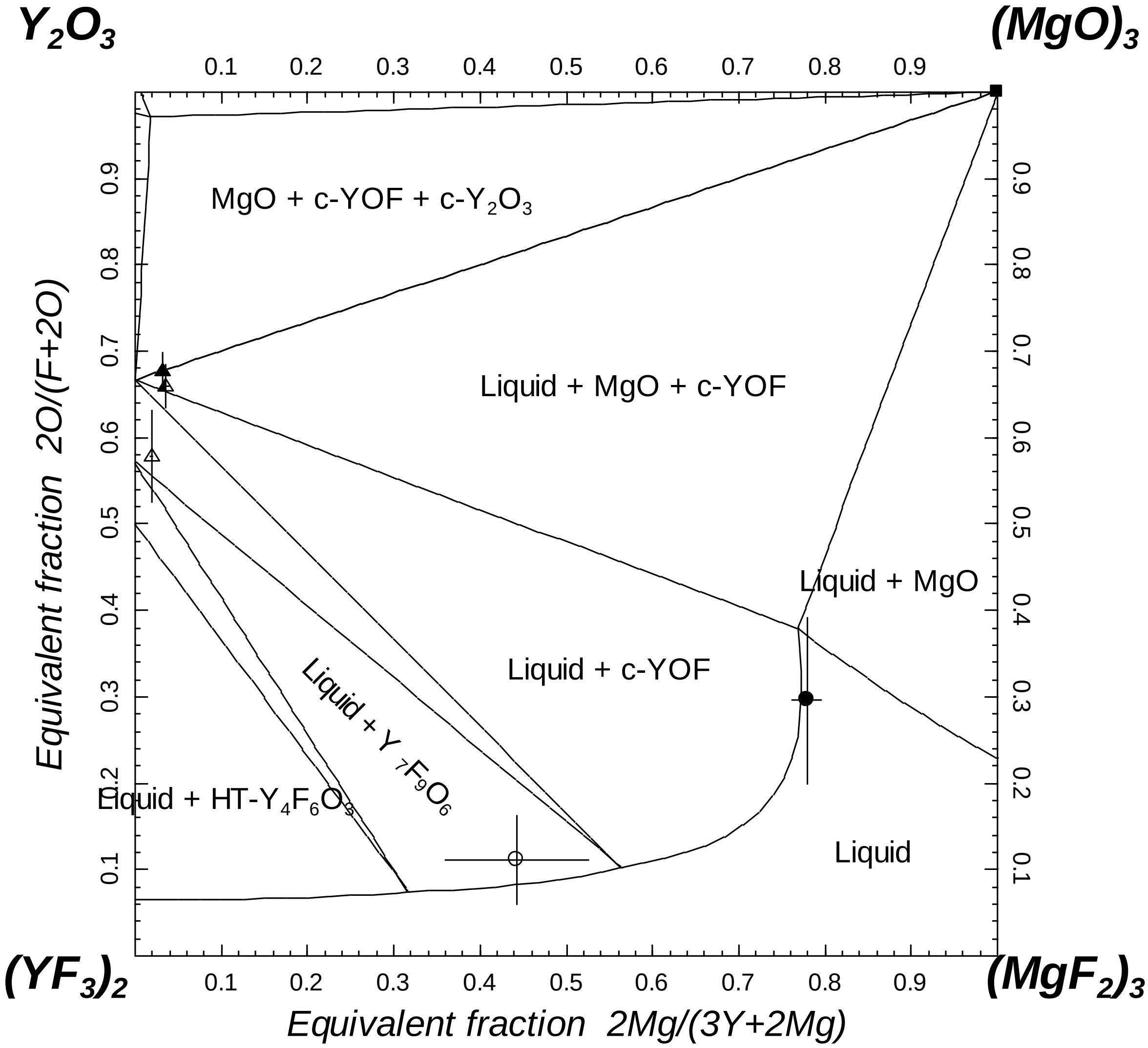

(d)

Figure 4.6 Calculated phase diagram compared with experimental results. (a) 1273, (b) 1573, (c) 1673, and (d) 1773 K.

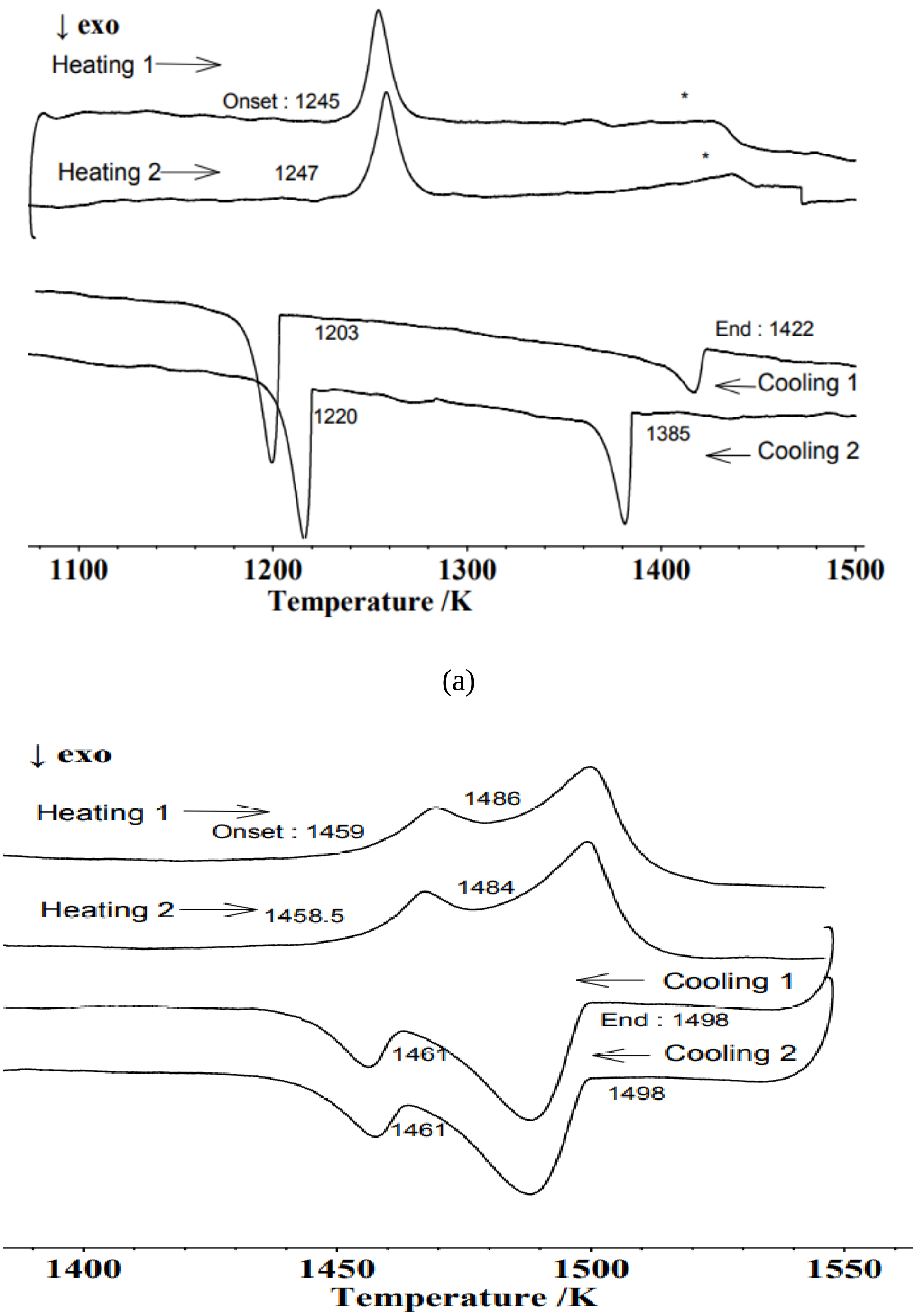

(a)

(b)

Figure 4.7 DTA result of for the samples: (a) sample with 0.5 YF_3-0.5 MgF_2-0.02 MgO composition and (b) 0.2 MgF_2-0.8 MgO-0.03YOF composition in mol fraction.

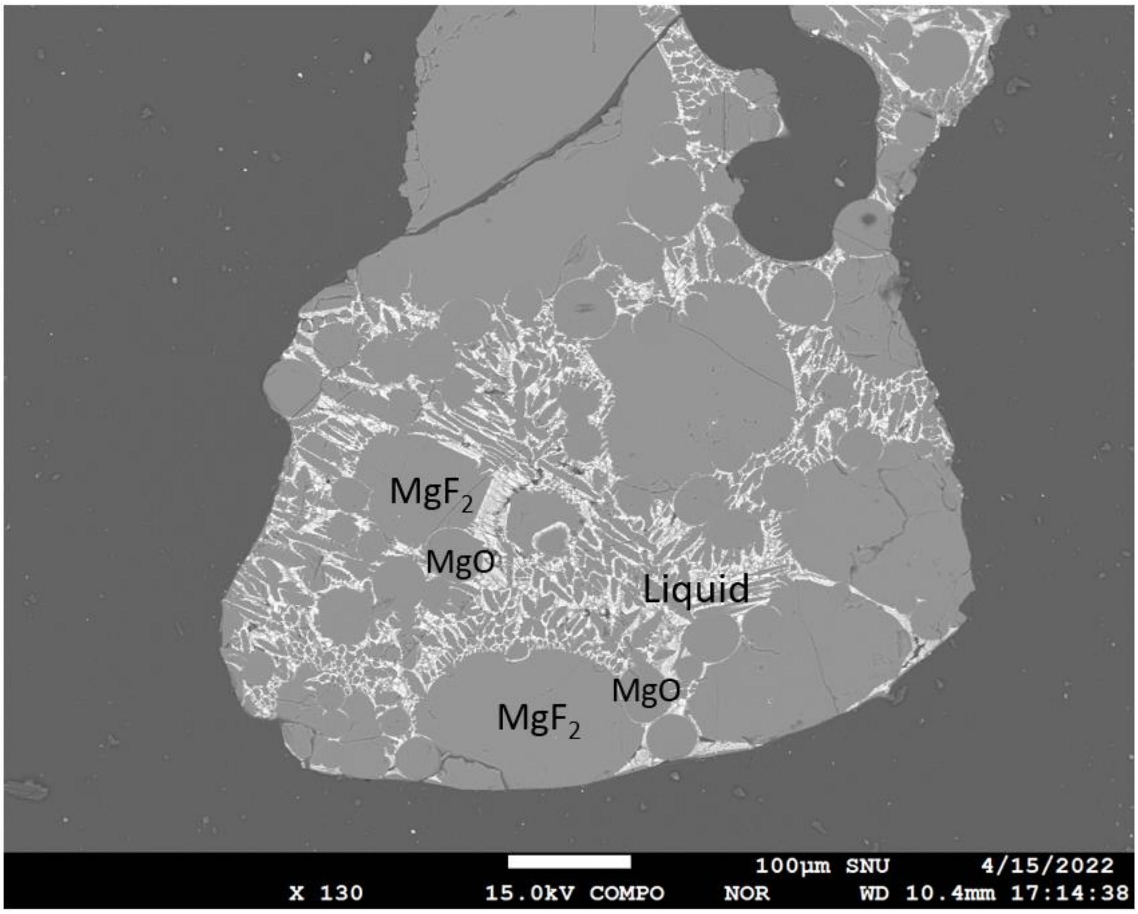

Figure 4.8 EPMA BSE image of the sample with 0.2 MgF$_2$-0.8 MgO-0.03YOF in mol fraction quenched at 1473 K.

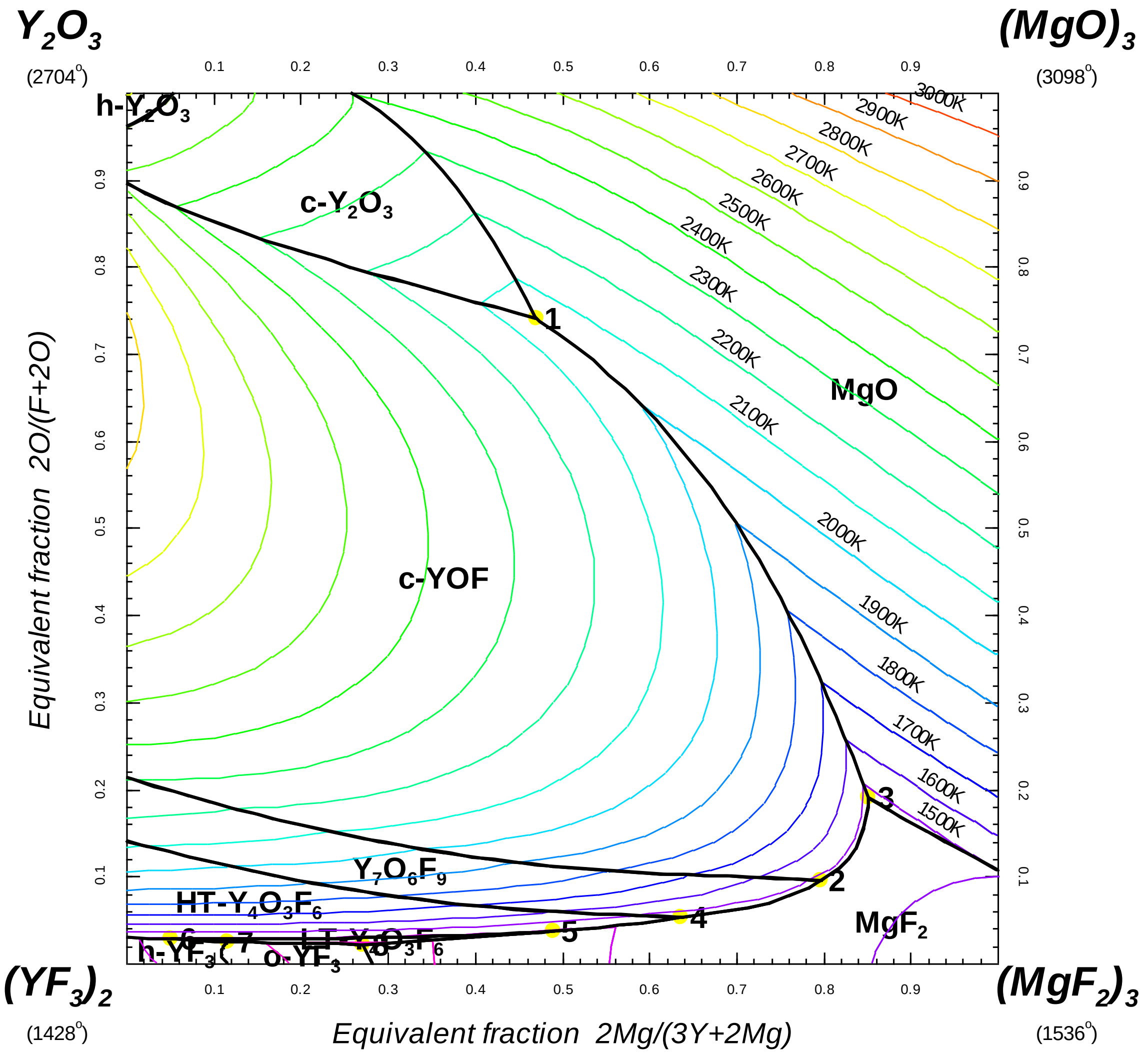
Y2O3
(2704°)
(MgO)3
(3098°)
(YF3)2
(1428°)
(MgF2)3
(1536°)
h-Y2O3
c-Y2O3
c-YOF
MgO
Y7O6F9
HT-Y4O3F6
LT-Y4O3F6
h-YF3
O-YF3
MgF2
1
2
3
4
5
6
7
8
3000K
2900K
2800K
2700K
2600K
2500K
2400K
2300K
2200K
2100K
2000K
1900K
1800K
1700K
1600K
1500K
0.1
0.2
0.3
0.4
0.5
0.6
0.7
0.8
0.9
Equivalent fraction 2O/(F+2O)
Equivalent fraction 2Mg/(3Y+2Mg)

(a)

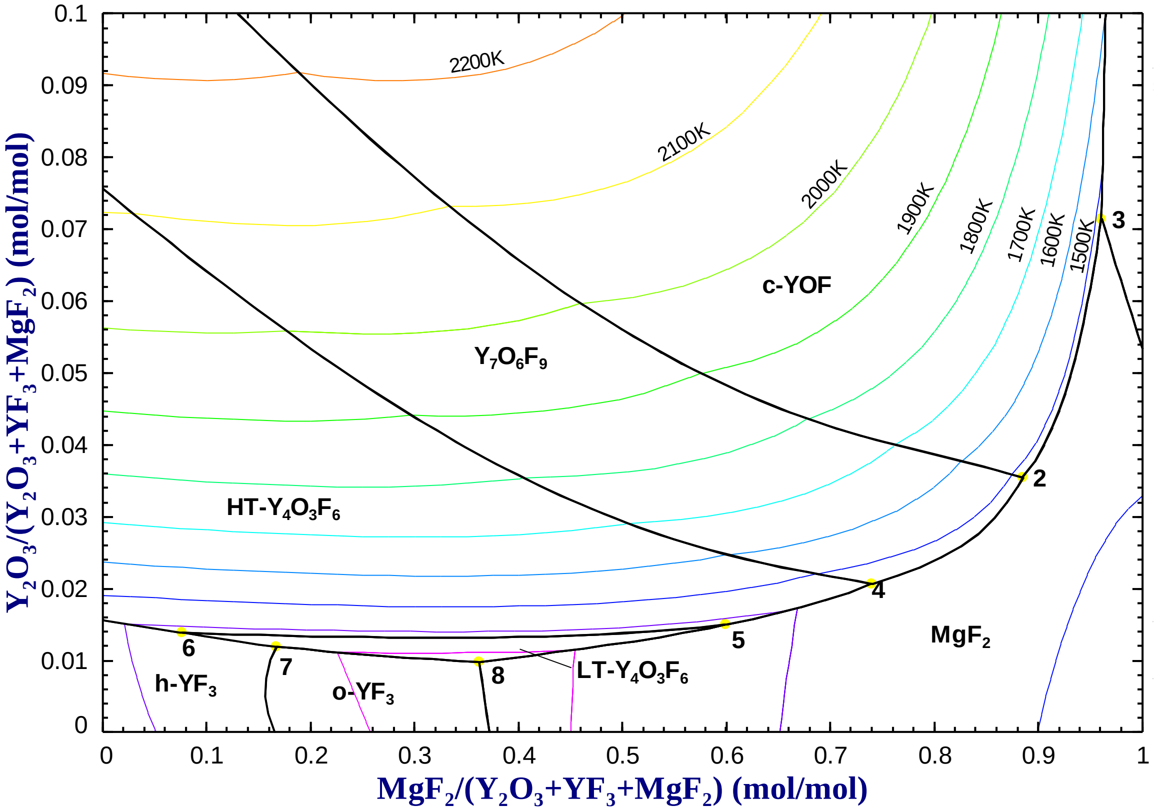

(b)

Figure 4.9 Predicted liquidus projection of the MgO-MgF_2-Y_2O_3-YF_3 reciprocal system in the present study. (a) overall reciprocal system, and (b) close-up view in the MgF_2-YF_3 rich region.

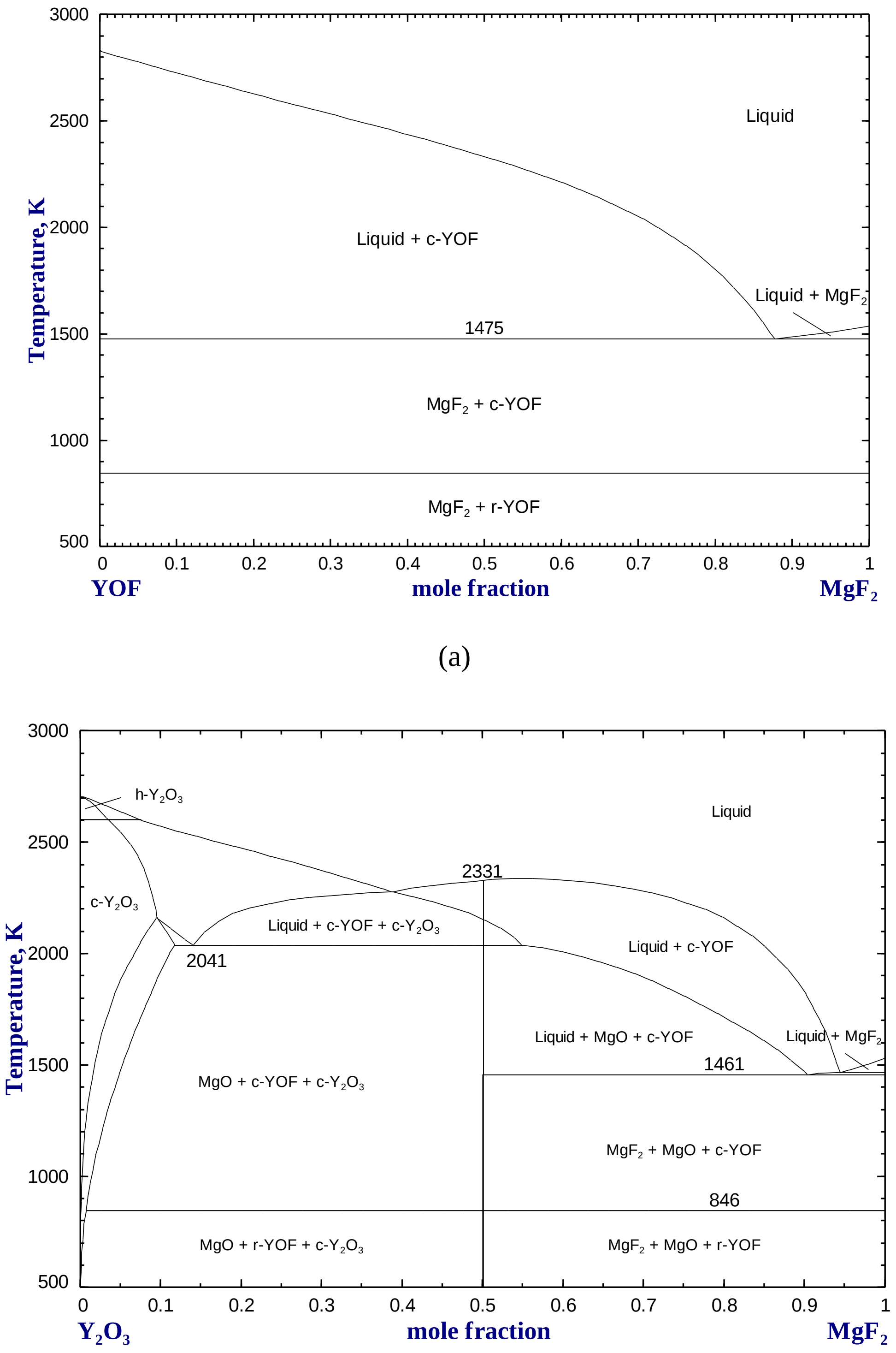

(a)

(b)

Figure 4.10 Calculated phase diagrams in the present study: (a) YOF-MgF_2 system and (b) Y_2O_3-MgF_2 system.

Table 4.1 Summary of the equilibration and quenching experimental results in the present study.

Sample	Starting composition (mol fraction)			T (K)	Duration (hrs)	Phase (XRD / EPMA)	Composition							
	MgO	MgF_2	YF_3				# of analyses	Mg (wt.%) (2σ)	Y (wt.%) (2σ)	O (wt.%) (2σ)	F (wt.%) (2σ)	Total (wt.%) (2σ)	2Mg /(3Y+2 Mg) (mol fr.) (2σ)	2O /(F+2O) (mol fr.) (2σ)
#1	0.93	0.00	0.07	1573	3	MgO	3	58.93 (0.65)	0.12 (0.02)	38.01 (0.46)	0.00 (0.00)	97.05 (1.09)	0.9992 (0.0001)	1.0000 (0.0000)
						YOF	3	0.92 (0.25)	69.43 (1.71)	12.31 (1.18)	14.24 (0.76)	96.90 (0.64)	0.0312 (0.0086)	0.6723 (0.0096)
						Liquid	Too scattered							
#2	0.93	0.00	0.07	1673	3	MgO	5	58.33 (0.75)	0.05 (0.11)	37.62 (0.99)	0.00 (0.00)	96.00 (1.01)	0.9996 (0.0008)	1.0000 (0.0000)
						YOF	3	0.98 (0.16)	69.01 (0.73)	12.30 (0.42)	14.42 (0.66)	96.71 (0.89)	0.0334 (0.0052)	0.6695 (0.0174)
						Liquid	Too scattered							

#3	0.93	0.00	0.07	1773	3	MgO	4	57.42 (0.95)	0.08 (0.13)	35.80 (1.06)	0.00 (0.00)	93.30 (1.99)	0.9994 (0.0005)	1.0000 (0.0000)
						YOF	3	0.93 (0.08)	68.52 (0.61)	12.25 (1.40)	13.89 (0.32)	95.60 (1.23)	0.0322 (0.0027)	0.6766 (0.0229)
						Liquid		Too scattered						
#4	0.69	0.00	0.31	1273	45	MgO		Not analyzed						
						MgF_2	4	38.11 (6.10)	0.04 (0.03)	0.73 (0.92)	64.82 (1.93)	103.71 (6.88)	0.9996 (0.0003)	0.0262 (0.0326)
						YOF	4	0.36 (0.16)	73.06 (2.53)	11.06 (1.32)	14.39 (2.27)	98.88 (3.42)	0.0120 (0.0050)	0.6460 (0.0248)
#5	0.69	0.00	0.31	1573	5	MgO	3	59.57 (0.61)	0.06 (0.05)	38.78 (0.80)	0.00 (0.00)	98.43 (1.22	0.9997 (0.0004)	1.0000 (0.0000)
						YOF	7	0.89 (0.41)	71.25 (4.23)	12.54 (1.29)	16.20 (2.38)	100.88 (4.77)	0.0298 (0.0150)	0.6474 (0.0562)
						Liquid	14	29.04 (3.21)	16.84 (4.18)	3.56 (2.00)	51.36 (3.29)	100.81 (3.51)	0.8075 (0.0529)	0.1408 (0.0688)
#6	0.69	0.00	0.31	1673	8	MgO	7	58.58 (0.50)	0.02 (0.04)	38.42 (0.85)	0.00 (0.00)	97.03 (1.15)	0.9998 (0.0003)	1.0000 (0.0000)

						YOF	7	0.92 (0.08)	72.52 (0.56)	12.44 (0.38)	15.51 (0.68)	101.39 (0.87)	0.0300 (0.0027)	0.6558 (0.0082)
						Liquid	11	30.03 (1.57)	16.15 (2.77)	3.39 (2.66)	53.88 (2.84)	103.45 (1.99)	0.8193 (0.0328)	0.1287 (0.0868)
#7	0.69	0.00	0.31	1773	4	MgO	5	59.30 (0.90)	0.08 (0.19)	38.52 (1.71)	0.00 (0.00)	97.90 (2.62)	0.9994 (0.0013)	1.0000 (0.0000)
						YOF	9	1.07 (0.16)	71.45 (2.41)	12.55 (1.24)	15.34 (0.69)	100.41 (1.93)	0.0354 (0.0058)	0.6598 (0.0258)
						Liquid	20	31.01 (3.16)	14.07 (4.64)	2.72 (2.31)	54.13 (5.22)	101.94 (5.36)	0.8427 (0.0566)	0.1059 (0.0818)
#8	0.43	0.43	0.14	1573	3	MgO	5	59.49 (0.66)	0.09 (0.06)	42.97 (0.43)	0.00 (0.00)	102.55 (0.96)	0.9994 (0.0004)	1.0000 (0.0000)
						YOF		Not analyzed						
						Liquid	12	28.99 (3.49)	16.96 (4.81)	4.35 (2.97)	50.59 (3.99)	100.88 (4.48)	0.8060 (0.0596)	0.1677 (0.1019)
#9	0.43	0.43	0.14	1673	3	MgO	4	59.69 (1.82)	0.12 (0.03)	35.30 (0.63)	0.00 (0.00)	95.11 (1.58)	0.9992 (0.0002)	1.0000 (0.0000)
						YOF		Not analyzed						

						Liquid	16	28.21 (2.76)	20.35 (5.07)	6.03 (1.97)	44.23 (6.31)	98.81 (4.54)	0.7715 (0.0597)	0.2451 (0.0837)
#10	0.43	0.43	0.14	1773	3	MgO	4	59.95 (0.55)	0.01 (0.03)	43.32 (1.03)	0.00 (0.00)	103.27 (1.29)	0.9999 (0.0002)	1.0000 (0.0000)
						YOF		Not analyzed						
						Liquid	15	28.48 (0.74)	19.57 (1.82)	8.29 (2.78)	46.77 (6.60)	103.11 (4.72)	0.7802 (0.0175)	0.2962 (0.0968)
#11	0.29	0.14	0.57	1273	36	MgF_2	4	38.97 (0.91)	0.02 (0.01)	0.00 (0.01)	64.55 (3.57)	103.54 (4.47)	0.9998 (0.0001)	0.0001 (0.0004)
						$Y_4O_3F_6$	5	0.05 (0.01)	70.54 (2.15)	9.27 (0.37)	21.48 (0.61)	101.35 (2.29)	0.0019 (0.0003)	0.5062 (0.0117)
						Liquid	9	8.96 (0.57)	53.17 (2.57)	0.54 (0.20)	38.09 (3.23)	100.77 (1.03)	0.2913 (0.0163)	0.0325 (0.0121)
#12	0.29	0.14	0.57	1573	5	$Y_7O_6F_9$	7	0.43 (0.04)	71.82 (1.79)	9.20 (1.59)	17.19 (2.21)	98.65 (3.16)	0.0146 (0.0013)	0.5593 (0.0155)
						Liquid	10	16.53 (4.61)	37.85 (6.83)	1.39 (1.04)	51.19 (4.24)	106.96 (2.57)	0.5142 (0.1168)	0.0608 (0.0459)
#13	0.29	0.14	0.57	1673	8	$Y_7O_6F_9$	9	0.65 (0.17)	71.77 (0.94)	9.90 (0.82)	17.66 (2.68)	99.98 (2.52)	0.0217 (0.0054)	0.5714 (0.0228)

						Liquid	15	14.09	42.16	1.93	44.00	102.19	0.4487	0.0956
								(2.13)	(3.46)	(1.30)	(7.10)	(5.89)	(0.0569)	(0.0688)
#14	0.29	0.14	0.57	1773	4	$Y_7O_6F_9$	6	0.58	71.18	10.67	18.39	100.82	0.0195	0.5793
								(0.03)	(1.41)	(1.36)	(1.88)	(1.20)	(0.0014)	(0.0536)
						Liquid	10	13.81	42.28	2.47	47.33	105.89	0.4431	0.1119
								(3.04)	(6.66)	(0.89)	(10.17)	(7.05)	(0.0837)	(0.0519)

Table 4.2 Phase transitions confirmed by differential thermal analysis in the present study.

No.	Composition (mol fr.)				Temperature (K)		Reaction
	MgO	MgF_2	YOF	YF_3	1st heating	2nd heating	
1	0.8	0.2			1495*	1493*	$MgO + MgF_2 \rightarrow$ liquid + MgO
2	0.02	0.5		0.5	1245	1247	$MgF_2 + YF_3 +$ LT-$Y_4O_3F_6 \rightarrow$ liquid + MgF_2 +LT-$Y_4O_3F_6$
					1422*	1385*	liquid + $MgF_2 \rightarrow$ liquid
3	0.8	0.2	0.033		1459	1458	?
					1486	1484	$MgO + MgF_2$ + c-YOF $\rightarrow$ liquid + MgO + c-YOF

* LT- and c- represent low temperature phase and cubic, respectively.

Table 4.3 The optimized thermodynamic parameters of solid and liquid solutions in the present study.

Phase and formula	Thermodynamic parameter
Liquid	$g^{o}_{Y,Mg;O,F} = -48316 + 25.559 * T$
(Y,Mg)(O,F)	$g^{00}_{Y,Mg;O} = 3000$
	$g^{10}_{Y,Mg;O} = 41000$
	$g^{00}_{Y,Mg;F} = 16599 - 13.986 * T$
	$g^{10}_{Y,Mg;F} = -5000$
	$g^{00}_{Y;O,F} = -31690 + 30 * T$
	$g^{02}_{Y;O,F} = -18000$
	$g^{00}_{Mg;O,F} = -6500$
c-Y_2O_3	$G^{o}_{Y_2;O_3;Va_1} = G^{o}_{Y_2O_3\#cubic}$
(Y,Mg)$_2$[O,F,Va]$_3$[F,Va]$_1$	$G^{o}_{Y_2;F_3;Va_1} = G^{o}_{Y\#hcp} + G^{o}_{YF_3\#hexagonal}$
	$G^{o}_{Y_2;O_3;F_1} = 2G^{o}_{YOF\#cubic} - \frac{1}{3} G^{o}_{Y\#hcp} - \frac{1}{3} G^{o}_{YF_3\#hexagonal} + \frac{1}{3} G^{o}_{Y_2O_3\#cubic} + 65000 + 15.876 * T$

	$G^{o}_{Y_2;F_3;F_1} = 2G^{o}_{YOF\#cubic} + \frac{2}{3}G^{o}_{Y\#hcp} + \frac{2}{3}\ G^{o}_{YF_3\#hexagonal} - \frac{2}{3}\ G^{o}_{Y_2O_3\#cubic} + 65000 + 15.876 * T$
	$G^{o}_{Y_2;Va_3;Va_1} = 2G^{o}_{Y\#hcp} +\ 250000$
	$G^{o}_{Y_2;Va_3F_1} = 2G^{o}_{YOF\#cubic} + \frac{5}{3}G^{o}_{Y\#hcp} - \frac{1}{3}\ G^{o}_{YF_3\#hexagonal}\ - \frac{2}{3}\ G^{o}_{Y_2O_3\#cubic} + 31500 + 15.876 * T$
	$G^{o}_{Mg_2;Va_3;Va_1} = 2G^{o}_{Mg\#hcp}$
	$G^{o}_{Mg_2;O_3;Va_1} = 3G^{o}_{MgO\#periclase} -\ G^{o}_{Mg\#hcp} + 95263 - 4.519 * T$
	$G^{o}_{Mg_2;Va_3;F_1} = 2G^{o}_{Mg\#hcp} +\ 2G^{o}_{YOF\#cubic} - \frac{1}{3}G^{o}_{Y\#hcp} - \frac{1}{3}\ G^{o}_{YF_3\#hexagonal} - \frac{2}{3}\ G^{o}_{Y_2O_3\#cubic} + 65000 + 12.876 * T$
	$G^{o}_{Mg_2;O_3;F_1} = 3G^{o}_{MgO\#periclase} -\ G^{o}_{Mg\#hcp} +\ 2G^{o}_{YOF\#cubic} - \frac{1}{3}G^{o}_{Y\#hcp} - \frac{1}{3}\ G^{o}_{YF_3\#hexagonal} - \frac{2}{3}G^{o}_{Y_2O_3\#cubic} + 160263 + 8.357 * T$
	$G^{o}_{Mg_2;F_3;F_1} = 2G^{o}_{MgF_2\#sellaite} +\ 70000$
	$G^{o}_{Mg_2;F_3Va_1} = 2G^{o}_{MgF_2\#sellaite} -\ 2G^{o}_{YOF\#cubic} + \frac{1}{3}G^{o}_{Y\#hcp} +\ \frac{1}{3}\ G^{o}_{YF_3\#hexagonal}\ +\ \frac{2}{3}\ G^{o}_{Y_2O_3\#cubic} + 135000 - 12.876 * T$
h-Y_2O_3	$G^{o}_{Y_2;O_3;Va_1} = G^{o}_{Y_2O_3\#hexagonal}$
$(Y)_2[O,F]_3[F,Va]_1$	$G^{o}_{Y_2;F_3;Va_1} = G^{o}_{Y\#hcp} +\ G^{o}_{YF_3\#hexagonal}$
	$G^{o}_{Y_2;O_3;F_1} = 2G^{o}_{YOF\#cubic} - \frac{1}{3}G^{o}_{Y\#hcp} - \frac{1}{3}\ G^{o}_{YF_3\#hexagonal} + \frac{1}{3}G^{o}_{Y_2O_3\#hexagonal} + 65000 + 15.876 * T$

	$G^o_{Y_2;F_3;F_1} = 2G^o_{YOF\#cubic} + \frac{2}{3}G^o_{Y\#hcp} + \frac{2}{3}\ G^o_{YF_3\#hexagonal} - \frac{2}{3}\ G^o_{Y_2O_3\#hexagonal} + 65000 + 15.876 * T$ $G^o_{Y_2;Va_3;Va_1} = 2G^o_{Y\#hcp} +\ 250000$ $G^o_{Y_2;Va_3F_1} = 2G^o_{YOF\#cubic} + \frac{5}{3}G^o_{Y\#hcp} - \frac{1}{3}\ G^o_{YF_3\#hexagonal}\ - \frac{2}{3}\ G^o_{Y_2O_3\#hexagonal} + 31500 + 15.876 * T$ $G^o_{Mg_2;Va_3;Va_1} = 2G^o_{Mg\#hcp}$ $G^o_{Mg_2;O_3;Va_1} = 3G^o_{MgO\#periclase} -\ G^o_{Mg\#hcp} + 95263 - 4.519 * T$ $G^o_{Mg_2;Va_3;F_1} = 2G^o_{Mg\#hcp} +\ 2G^o_{YOF\#cubic} - \frac{1}{3}G^o_{Y\#hcp} - \frac{1}{3}\ G^o_{YF_3\#hexagonal} - \frac{2}{3}\ G^o_{Y_2O_3\#hexagonal} + 65000 + 12.876 * T$ $G^o_{Mg_2;O_3;F_1} = 3G^o_{MgO\#periclase} -\ G^o_{Mg\#hcp} +\ 2G^o_{YOF\#cubic} - \frac{1}{3}G^o_{Y\#hcp} - \frac{1}{3}\ G^o_{YF_3\#hexagonal} - \frac{2}{3}G^o_{Y_2O_3\#hexagonal} + 160263 + 8.357 * T$ $G^o_{Mg_2;F_3;F_1} = 2G^o_{MgF_2\#sellaite} +\ 70000$ $G^o_{Mg_2;F_3Va_1} = 2G^o_{MgF_2\#sellaite} -\ 2G^o_{YOF\#cubic} + \frac{1}{3}G^o_{Y\#hcp} +\ \frac{1}{3}\ G^o_{YF_3\#hexagonal}\ +\ \frac{2}{3}G^o_{Y_2O_3\#hexagonal} + 135000 -\ 12.876 * T$
h-YF_3	$G^o_{YF_3} = G^o_{YF_3\#hexagonal}$
($YO_{1.5}$, YF_3, MgF_2)	$G^o_{YO_{1.5}} = \frac{1}{2}G^o_{Y_2O_3\#cubic}\ +\ 2500$

$$G^{o}_{MgF_2} = G^{o}_{MgF_2\#sellaite} + 25000$$

$$q^{11}_{YO_{1.5};YF_3} = -75000 + 40 * T$$

$$q^{11}_{MgF_2;YF_3} = -15324 + 9.5251 * T$$

Table 4.4 Calculated invariant reactions in the MgO-MgF_2-Y_2O_3-YF_3 system indicated in Fig. 8 (a).

No.	Equivalent fraction		Temperature (K)	Reaction
	2Mg / (3Y + 2Mg)	2O / (F + 2O)		
1	0.4702	0.7407	2041	MgO + c-Y_2O_3 soln + c-YOF → liquid
2	0.7966	0.0956	1472	liquid + MgF_2 + $Y_7O_6F_9$ → liquid + c-YOF + $Y_7O_6F_9$
3	0.8522	0.1901	1460	MgO + MgF_2 + c-YOF → liquid
4	0.6371	0.0533	1428	liquid + MgF_2 + HT-$Y_4O_3F_6$ → liquid + MgF_2 + $Y_7O_6F_9$
5	0.4900	0.0366	1371	liquid + MgF_2 + LT-$Y_4O_3F_6$ → liquid + MgF_2 + HT-$Y_4O_3F_6$
6	0.0510	0.0279	1371	liquid + LT-$Y_4O_3F_6$ + h-YF_3 soln → liquid + HT-$Y_4O_3F_6$ +h-YF_3 soln
7	0.1164	0.0248	1321	liquid + LT-$Y_4O_3F_6$ + o-YF_3 → liquid + h-YF_3 soln + o-YF_3
8	0.2713	0.0219	1246	MgF_2 + LT-$Y_4O_3F_6$ + o-YF_3 → liquid

Chapter 5. Conclusion

5.1 Summary

All phase diagram experimental data in the literatures for MgO-MgF_2, MgO-Y_2O_3, and MgF_2-YF_3 binary systems were critically evaluated and optimized in the present study. Since there are insufficient phase diagram data of the Y_2O_3-YF_3 binary system and no phase diagram data in the MgO-MgF_2-Y_2O_3-YF_3 reciprocal system, phase diagram experiments were carried out for both systems. Accurate and consistent thermodynamic database of each binary systems and reciprocal system was constructed employing CALPHAD technique based on new experimental data in the present study and available literature data. The Gibbs energy of compounds were determined based on the data from the literature. The Modified Quasichemical Model (MQM) was used to describe the Gibbs energy of the liquid solutions. The Gibbs energy of the solid solutions were modeled using Compound Energy Formalism (CEF) or Bragg-Williams random mixing model considering their crystal structures. The model parameters were optimized to reproduce the phase diagram data as well as thermodynamic property data.

The phase diagrams of the Y_2O_3-YF_3 and MgO-MgF_2-Y_2O_3-YF_3 systems were established for the very first time based on the experimental data and thermodynamic modeling results of the present study. The thermodynamic properties and phase diagram within the system can be calculated by using the thermodynamic database with Gibbs energy minimization routine in FactSage^{TM} software. The database developed in the present study can be integrated to the existing database in the FactSage^{TM} and employed for the complex thermodynamic calculations of multicomponent systems relevant to various industrial processes.

As applications of the present thermodynamic database, the possibility of metastable dissolution of F in Y_2O_3 ceramic heater material during the plasma etching and cleaning process was calculated. In comparison to solid YOF, the diffusion penetration of F into solid Y_2O_3 was explained by the nature of cubic-Y_2O_3 with a bixbyite crystal structure.

5.2 Original contribution to knowledge

The original contributions of the present study to knowledge are as below:

1. The phase diagram of the Y_2O_3-YF_3 system was experimentally investigated up to 1973 K and the overall phase diagram of this binary system was presented for the first time.
2. The solubility of the Y_2O_3 solid solution was experimentally determined and modeled using new CEF sublattice structure model which reflects the crystal structure of the solution.
3. Thermodynamic properties of the YOF compound was determined properly based on the critical evaluations of all literature data for the first time.
4. The present study predicted the melting point of YOF and vernier phases by evaluating the thermodynamic property data from literatures and phase diagram data of this study.
5. The phase diagram of the MgO-MgF_2-Y_2O_3-YF_3 reciprocal system at high temperature was investigated for the first time.
6. The thermodynamic database for the rare earth oxy-fluoride system was constructed

and integrated to to the FactSage thermodynamic database.

5.3 Future suggestions

Even though the given findings are the best that can be achieved at the current state, it would be helpful to investigate the following information in understanding the thermodynamics of the MgO-MgF_2-Y_2O_3-YF_3 system.

1. The exact melting point of YOF and vernier phases by the experiments.
2. The exact temperature of the eutectic reaction between Y_2O_3 and YOF.
3. Thermodynamic properties of the liquid phase.
4. Expansion of the thermodynamic modeling and database including CaO and CaF_2 to the MgO-MgF_2-Y_2O_3-YF_3 system for more relevant industrial applications.
5. The phase diagram study forrare earth oxide-rare earth fluoride systems other than Y_2O_3-YF_3 system to investigate the general trends in the phase diagram depending on rare earth elements and expand the thermodynamic database.

Appendix. Review of rare earth oxyfluoride systems

As mentioned in section 5.3, it would be useful to expand the database by integrating other rare earth oxide-rare earth fluoride systems. Thus, the available thermodynamic data for other REOF compounds (NdOF, LaOF, and CeOF) from the literature were reviewed and critically assessed/recalculated using the reference data in FactSage database. In addition, based on the simple assumptions, the phase diagrams of RE_2O_3-REF_3 system were roughly estimated.

A1. Evaluation of the Gibbs energy of REOF

A1.1 NdOF

Levitskii and Balak [12] performed the emf measurement for the $Nd_{2-x}O_{3-3x}F_{3x}$ (x = 0.1 ~ 0.48) samples using the following cell configuration at 960-1465 K:

Cell-A: (-) O_2, Pt | CaO, CaF_2 || CaF_2 || $Nd_{2-x}O_{3-3x}F_{3x}$ | Pt, O_2 (+)

The samples of $Nd_{2-x}O_{3-3x}F_{3x}$ (x = 0.1 ~ 0.48) should be all 'Nd_2O_3+NdOF' mixtures. The oxygen partial pressures were fixed at 10^{-5} Pa and $1\sim10^2$ Pa. The difference of F_2 partial pressures were measured by emf technique to determine the Gibbs energy of NdOF phase. It should be noted that the emf values for all $Nd_{2-x}O_{3-3x}F_{3x}$ samples were the same regardless of sample compositions but varied with temperature. The Gibbs energies of hexagonal Nd_2O_3 were taken from the previous study of rare earth sesquioxides by our group.[26] The Gibbs energies of NdF_3 were taken from the FactSage FactPS database [1, 15, 16], originated from the thermodynamic data compilation by Barin.[27]

$$2NdOF(s) + CaO(s) = Nd_2O_3(s) + CaF_2(s) \qquad (25)$$

$$\Delta G_T^o = (-25{,}700 \pm 1{,}100) + (12.8 \pm 0.8) * T \ \text{(J/mol)} \qquad (26)$$

Considering the Gibbs energies of pure CaO, CaF_2, Nd_2O_3, and NdF_3 used in the present study [15, 16, 26], the Gibbs energy for the formation of NdOF were re-calculated in the temperature range between 1193 and 1388 K in order to keep the internal consistency:

$$1/3\ Nd_2O_3(s) + 1/3\ NdF_3(s) = NdOF(s) \quad (27)$$

$$\Delta G_T^o = -(26{,}992 \pm 964) - (10.617 \pm 0.729) * T\ (\mathrm{J/mol})\ \text{ at 1193-1388 K} \quad (28)$$

It should be noted that the Gibbs energy of NdOF phase derived in the present study (see Eq. (28)) is more negative than the value by Levitskii and Balak [12], which would result from the difference in the standard Gibbs energies of CaO, CaF_2, Nd_2O_3 and NdF_3 used in the conversion.

Ji and Xi [46] also performed the emf measurement for the NdOF samples using the following cell configuration at 981-1168 K:

Cell-B: O_2, Pt | MgO, MgF_2 || CaF_2 || NdOF, Nd_2O_3 | Pt, O_2

The oxygen partial pressures were fixed at 2.17×10^4 Pa. The difference of F_2 partial pressures were measured by emf technique to determine the Gibbs energy of NdOF phase.

$$2NdOF(s) + MgO(s) = Nd_2O_3(s) + MgF_2(s) \quad (29)$$

$$\Delta G_T^o = -69{,}662 + 9.65 * \mathrm{T}\ (\mathrm{J/mol}) \quad (30)$$

Considering the Gibbs energies of pure CaO, CaF_2, Nd_2O_3, and NdF_3 used in the present study [15, 16, 26], the Gibbs energy for the formation of NdOF were re-calculated in the temperature range between 1193 and 1388 K in order to keep the internal consistency:

$$1/3\ Nd_2O_3(s) + 1/3\ NdF_3(s) = NdOF(s) \quad (27)$$

$$\Delta G_T^o = -40{,}757 + 1.595 * T\ (\mathrm{J/mol})\ \text{ at 981-1168 K} \quad (31)$$

A1.2. LaOF

Hong et al. [47] performed the emf measurement for the LaOF using the following cell configuration at 950-1120 K:

Cell-A: O_2, Pt | CaF_2, LaOF, La_2O_3 || Caβ”-Al_2O_3 || CaO| Pt, O_2

The samples of LaOF are all ‘La_2O_3+LaF_3 (1:1 mole fraction)’ mixtures. The difference of F_2 partial pressures were measured by emf technique to determine the Gibbs energy of LaOF phase. The Gibbs energies of hexagonal La_2O_3 were taken from the previous study of rare earth sesquioxides by our group.[26] The Gibbs energies of LaF_3 were taken from the FactSage FactPS database [1, 15, 16], originated from the thermodynamic data compilation by Barin.[27]

$La_2O_3(s) + CaF_2(s) = 2LaOF(s) + CaO(s)$ (29)

$$\Delta G_T^o = (-93{,}324 \pm 737) + (42.666 \pm 0.68) * \mathrm{T} \ \ (\mathrm{J/mol}) \qquad (30)$$

Considering the Gibbs energies of pure CaO, CaF_2, La_2O_3, and LaF_3 used in the present study [15, 16, 26], the Gibbs energy for the formation of LaOF were re-calculated in the temperature range between 950 and 1120 K in order to keep the internal consistency:

$1/3\ La_2O_3(s) + 1/3\ LaF_3(s) = LaOF(s)$ (31)

$$\Delta G_T^o = -(42{,}580 \pm 368) + (16.133 \pm 0.338) * T\ (\mathrm{J/mol}) \text{ at 950-1120 K} \qquad (32)$$

A1.3 CeOF

Hong et al. [47] also performed the emf measurement for the CeOF using the following cell configuration at 1077-1277 K:

Cell-A: Pt | CeO_2, CeOF, CaF_2, CaO || CSZ || Pt, O_2

They used calcia stabilized zirconia (CSZ) for the sold electrolytes. They indicated that the CeOF samples are the mixture of CeO_2 + CeF_3 (2:1 mole fraction), but the exact molar raio of CeOF cannot be made from CeO_2 and CeF_3 mixtures.

The difference of O_2 partial pressures were measured by emf technique to determine the Gibbs energy of CeOF phase. The Gibbs energies of CeO_2 and CeF_3 were taken from the FactSage FactPS database [1, 15, 16], originated from the thermodynamic data compilation by Barin.[27]

$$2CeOF(s) + CaO(s) + 1/2O_2(g) = 2CeO_2(s) + CaF_2(s) \qquad (33)$$

$$\Delta G_T^o = -204{,}355 + 93.89 * \mathrm{T}\ (\mathrm{J/mol}) \qquad (34)$$

Considering the Gibbs energies of pure CaO, CaF_2, CeO_2, and CeF_3 used in the present study [1, 15, 16, 26], the Gibbs energy for the formation of CeOF were re-calculated in the temperature range between 1077 and 1277 K in order to keep the internal consistency:

$$1/3\ Ce_2O_3(s) + 1/3\ CeF_3(s) = CeOF(s) \qquad (35)$$

$$\Delta G_T^o = 21097 - 40.559 * T\ (\mathrm{J/mol})\ \text{ at 950-1120 K} \qquad (36)$$

A1.4 Summary

All the evaluated Gibbs energy data are plotted in the following Fig. A-1. As can be seen, unfortunately, there is no certain trend in the standard Gibbs energy of REOF (RE(s) + $0.5O_2(g) + 0.5F_2(g)$ = REOF(s)) or Gibbs energy of reaction of REOF ($1/3RE_2O_3(s) + 1/3REF_3(s)$ = REOF(s)). Roughly, the Gibbs energy of reaction of all REOF including YOF, NdOF, LaOF, and CeOF are existing within about -40 to 0 kJ/mol. The temperature dependence of the reaction Gibbs energy (that is, entropy of reaction, $-\Delta S_{reaction}$) for all REOF is also varied from positive and negative value without any general trend.

A2. Simple estimation of phase diagram of RE_2O_3-REF_3 system

In spite of its importance, the phase diagram of the RE_2O_3-REF_3 system has not been well studied. In order to provide a rough phase diagram for each RE_2O_3-REF_3 system, the following assumptions were made, and thermodynamic calculations were performed to predict the phase diagram.

Assumption (1): 1/3RE_2O_3(cubic) + 1/3REF_3(orthorhombic) = REOF(s) : ΔG^{o}_{rxn} = -40 kJ/mol

Assumption (2): Liquid RE_2O_3-1/3REF_3 solution is an ideal solution

Assumption (3): No solid solution and no vernier phases to simplify the system

As shown in Fig. A-1, the Gibbs energy of reaction of REOF is widely spready. But roughly speaking, it could be possible to fix the constant ΔG^{o}_{rxn} = -40 kJ/mol for REOF phase. According to the thermodynamic optimization of the Y_2O_3-YF_3 system (see Chapter 3), the liquid phase of the Y_2O_3-YF_3 system was close to an ideal solution. So, similar assumption can be applied for other RE_2O_3-REF_3 liquid solution. The predicted phase diagram of the RE_2O_3-REF_3 system based on the above assumptions are presented in Fig. A2, and the general trend of the melting temperature of REOF is plotted in Fig. A3. The accuracy of the prediction should be evaluated in future study.

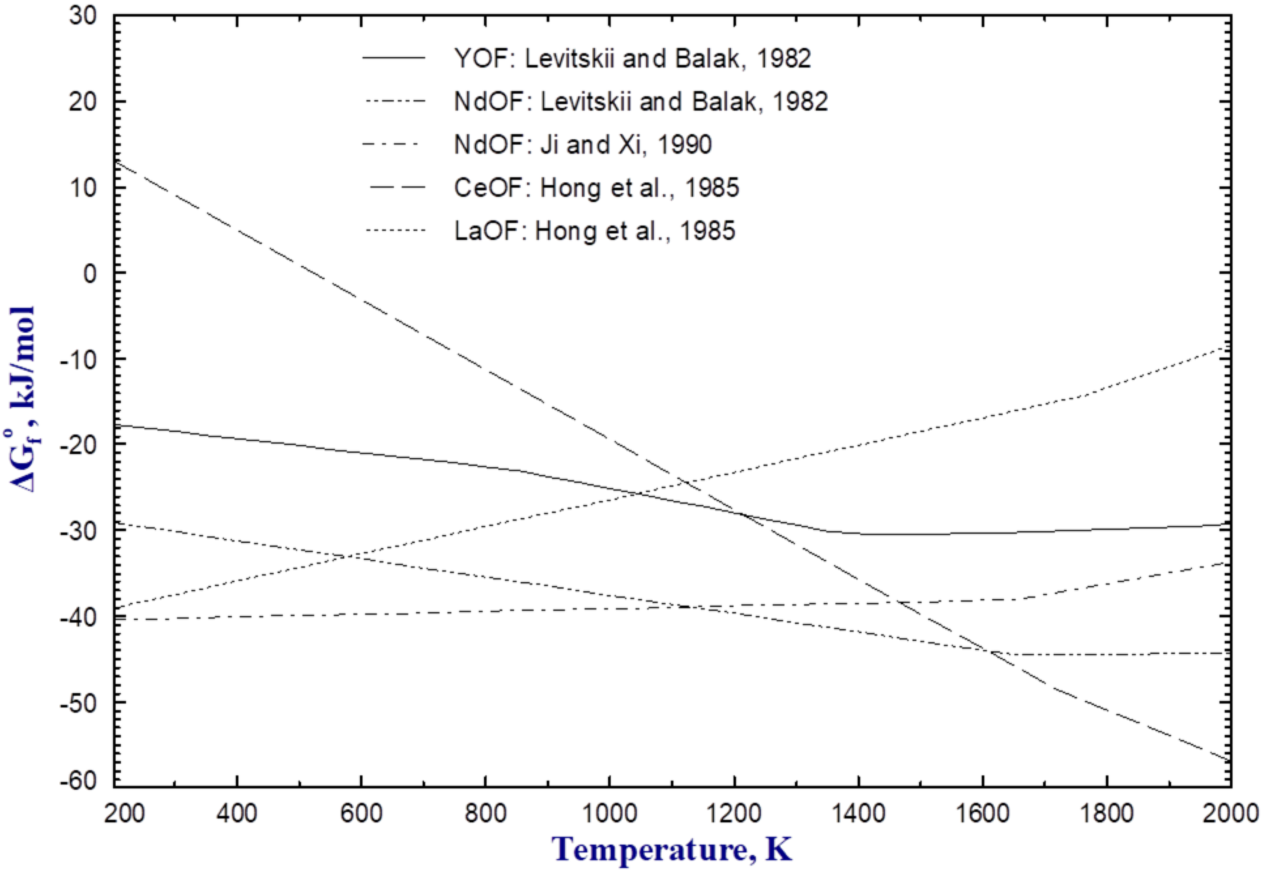
YOF: Levitskii and Balak, 1982
NdOF: Levitskii and Balak, 1982
NdOF: Ji and Xi, 1990
CeOF: Hong et al., 1985
LaOF: Hong et al., 1985
ΔG_f^o, kJ/mol
Temperature, K
30
20
10
0
-10
-20
-30
-40
-50
-60
200
400
600
800
1000
1200
1400
1600
1800
2000

(a)

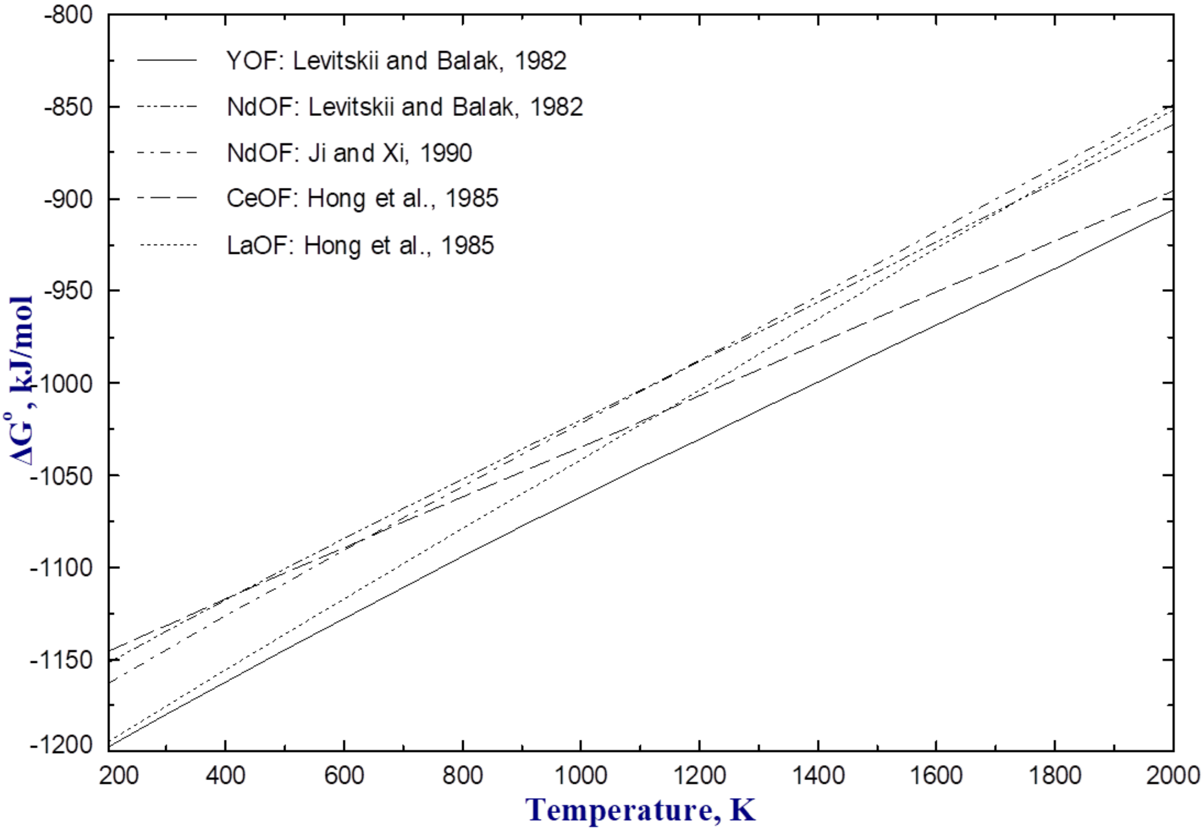

(b)

Fig. A-1 (a) Standard Gibbs energy of REOF(s) (RE(s) + $0.5O_2$(g) + $0.5F_2$(g) = REOF(s)), and (b) Gibbs energy of reaction of REOF from RE2O3 and REF3 (1/3RE_2O_3(s) + 1/3REF_3(s) = REOF(s)).

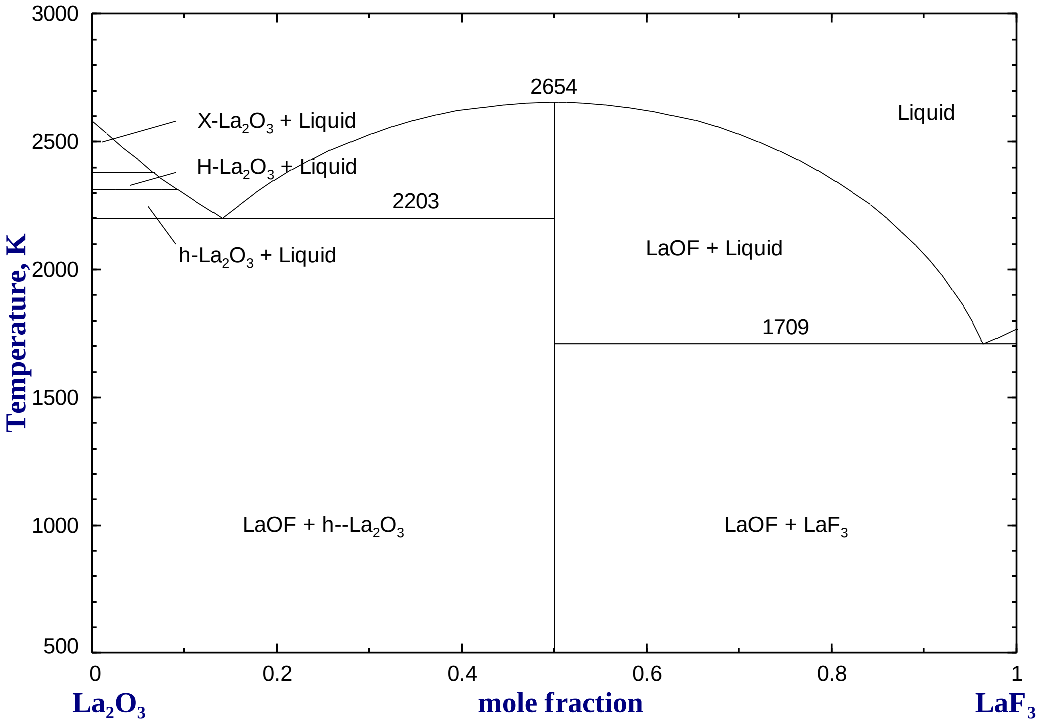
3000
2500
2000
1500
1000
500
Temperature, K
0
0.2
0.4
0.6
0.8
1
La_2O_3
mole fraction
LaF_3
2654
Liquid
X-La_2O_3 + Liquid
H-La_2O_3 + Liquid
2203
h-La_2O_3 + Liquid
LaOF + Liquid
1709
LaOF + h--La_2O_3
LaOF + LaF_3

(a)

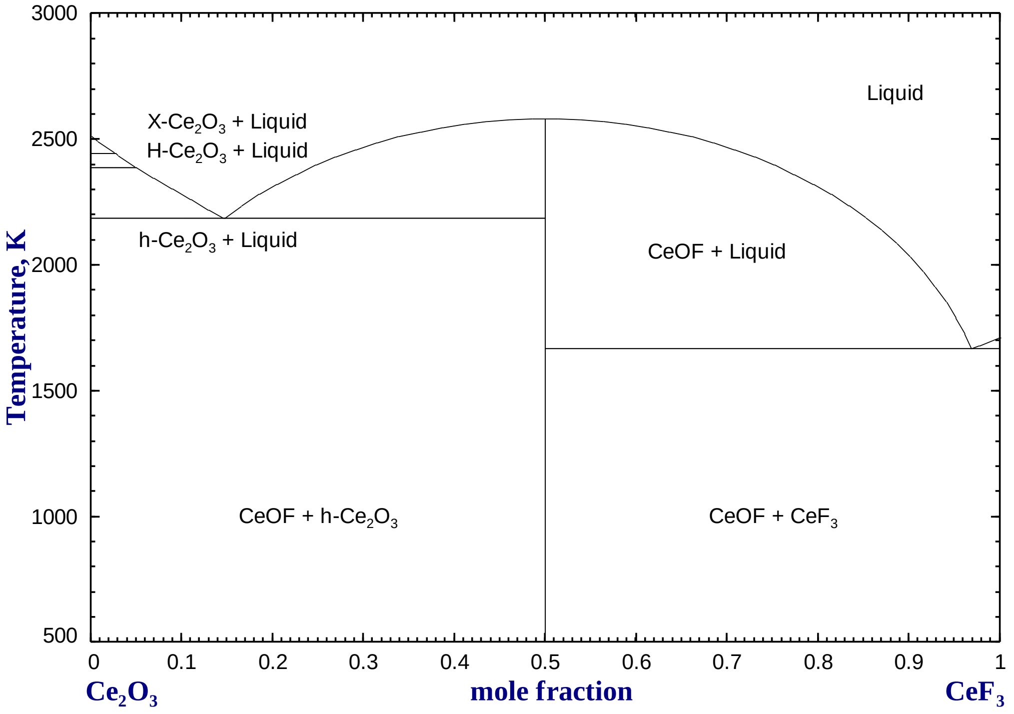
3000
2500
2000
1500
1000
500
Temperature, K
0
0.1
0.2
0.3
0.4
0.5
0.6
0.7
0.8
0.9
1
Ce_2O_3
mole fraction
CeF_3
Liquid
X-Ce_2O_3 + Liquid
H-Ce_2O_3 + Liquid
h-Ce_2O_3 + Liquid
CeOF + Liquid
CeOF + h-Ce_2O_3
CeOF + CeF_3

(b)

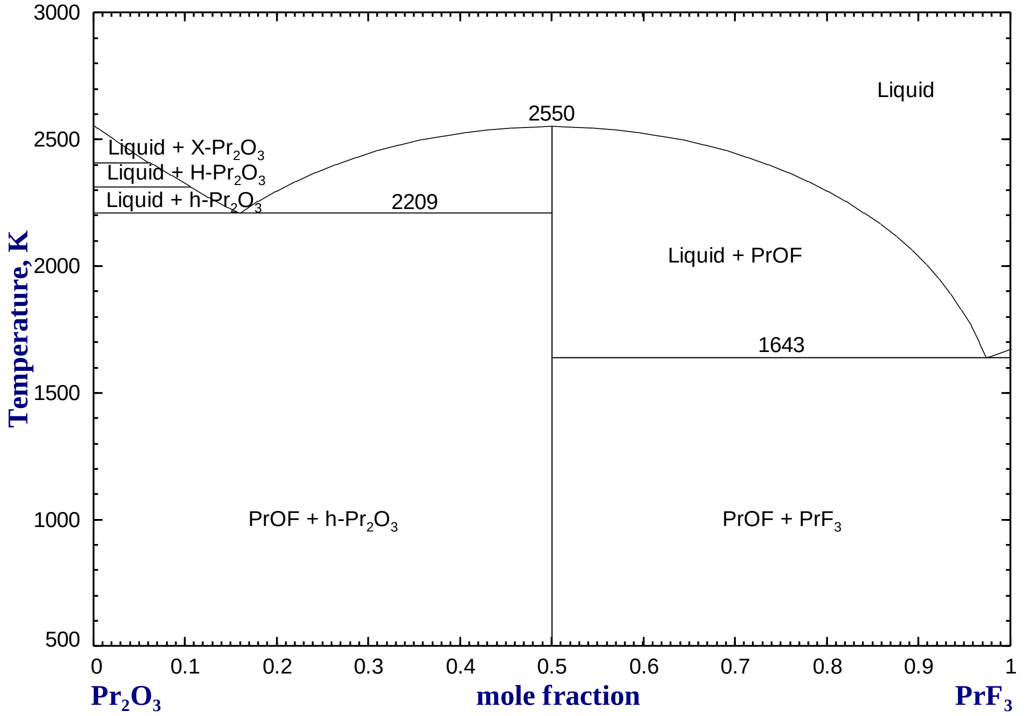
3000
2500
2000
1500
1000
500
Temperature, K
0
0.1
0.2
0.3
0.4
0.5
0.6
0.7
0.8
0.9
1
Pr_2O_3
mole fraction
PrF_3
Liquid
2550
Liquid + X-Pr_2O_3
Liquid + H-Pr_2O_3
Liquid + h-Pr_2O_3
2209
Liquid + PrOF
1643
PrOF + h-Pr_2O_3
PrOF + PrF_3

(c)

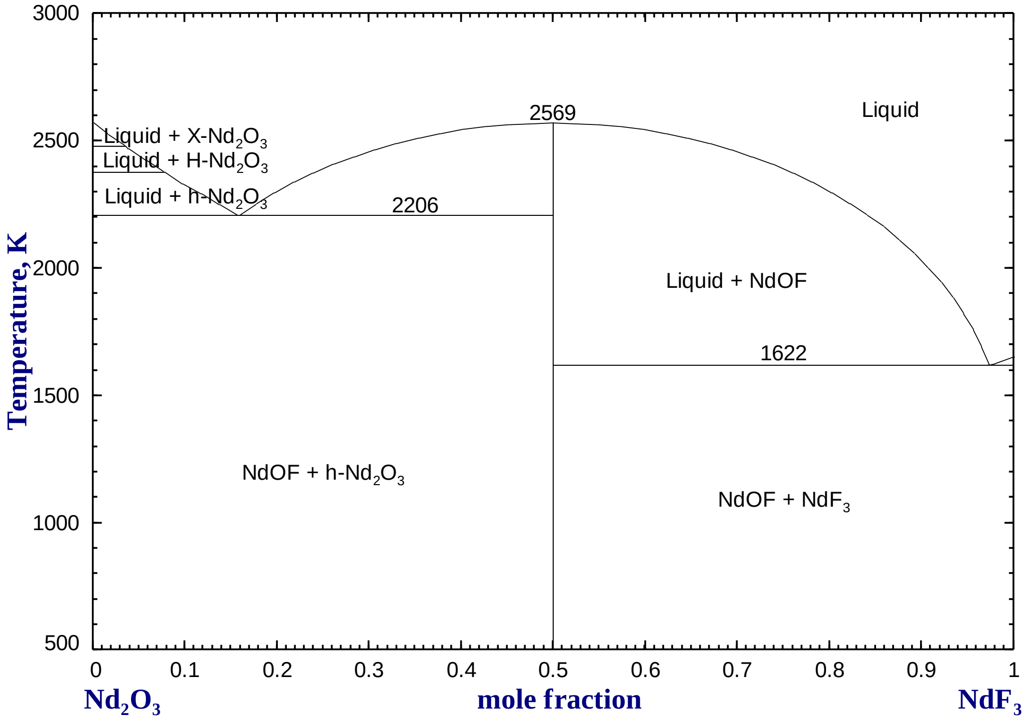
3000
2500
2000
1500
1000
500
Temperature, K
0
0.1
0.2
0.3
0.4
0.5
0.6
0.7
0.8
0.9
1
Nd_2O_3
mole fraction
NdF_3
Liquid
2569
Liquid + X-Nd_2O_3
Liquid + H-Nd_2O_3
Liquid + h-Nd_2O_3
2206
Liquid + NdOF
1622
NdOF + h-Nd_2O_3
NdOF + NdF_3

(d)

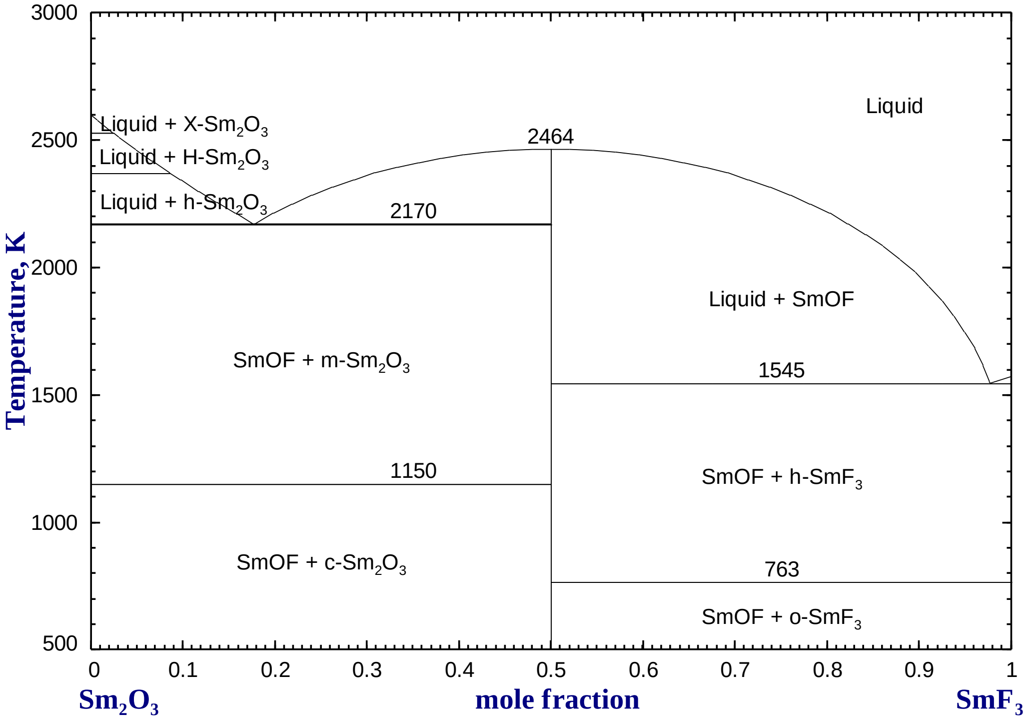
3000
2500
2000
1500
1000
500
Temperature, K
0
0.1
0.2
0.3
0.4
0.5
0.6
0.7
0.8
0.9
1
Sm_2O_3
mole fraction
SmF_3
Liquid
Liquid + X-Sm_2O_3
Liquid + H-Sm_2O_3
Liquid + h-Sm_2O_3
2464
2170
Liquid + SmOF
SmOF + m-Sm_2O_3
1545
1150
SmOF + h-SmF_3
SmOF + c-Sm_2O_3
763
SmOF + o-SmF_3

(e)

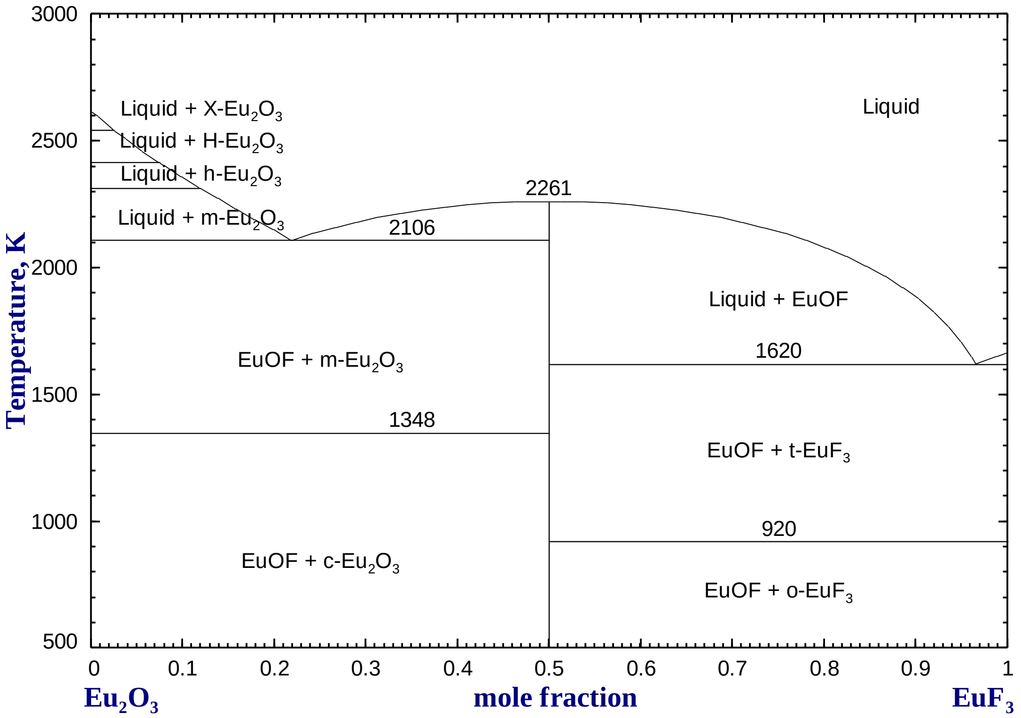
3000
2500
2000
1500
1000
500
Temperature, K
0
0.1
0.2
0.3
0.4
0.5
0.6
0.7
0.8
0.9
1
Eu_2O_3
mole fraction
EuF_3
Liquid
Liquid + X-Eu_2O_3
Liquid + H-Eu_2O_3
Liquid + h-Eu_2O_3
Liquid + m-Eu_2O_3
2261
2106
Liquid + EuOF
EuOF + m-Eu_2O_3
1620
1348
EuOF + t-EuF_3
920
EuOF + c-Eu_2O_3
EuOF + o-EuF_3

(f)

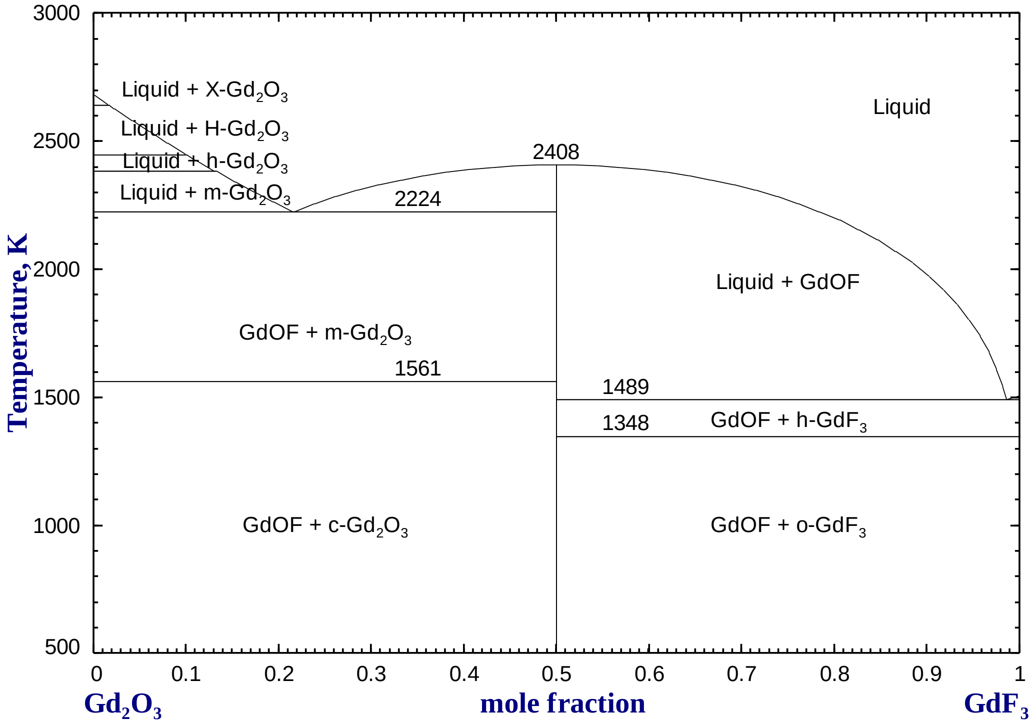
Temperature, K
3000
2500
2000
1500
1000
500
0
0.1
0.2
0.3
0.4
0.5
0.6
0.7
0.8
0.9
1
Gd2O3
mole fraction
GdF3
Liquid + X-Gd2O3
Liquid + H-Gd2O3
Liquid + h-Gd2O3
Liquid + m-Gd2O3
Liquid
2408
2224
Liquid + GdOF
GdOF + m-Gd2O3
1561
1489
1348
GdOF + h-GdF3
GdOF + c-Gd2O3
GdOF + o-GdF3

(g)

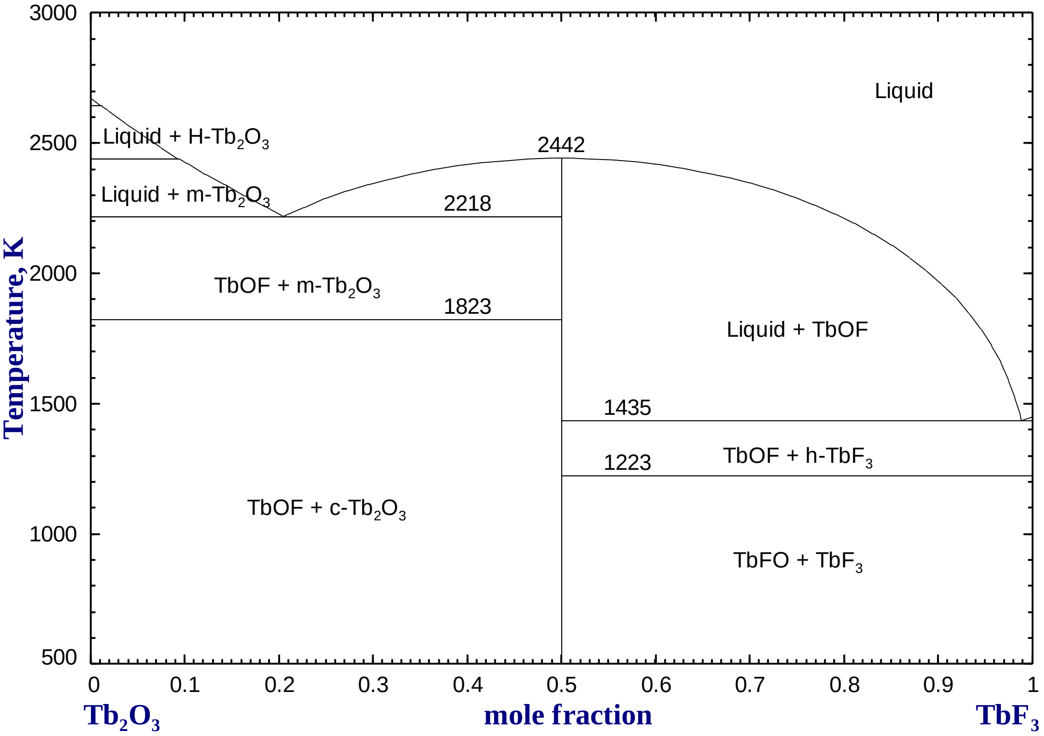
Temperature, K
3000
2500
2000
1500
1000
500
0
0.1
0.2
0.3
0.4
0.5
0.6
0.7
0.8
0.9
1
Tb2O3
mole fraction
TbF3
Liquid
Liquid + H-Tb2O3
2442
Liquid + m-Tb2O3
2218
TbOF + m-Tb2O3
1823
Liquid + TbOF
1435
1223
TbOF + h-TbF3
TbOF + c-Tb2O3
TbFO + TbF3

(h)

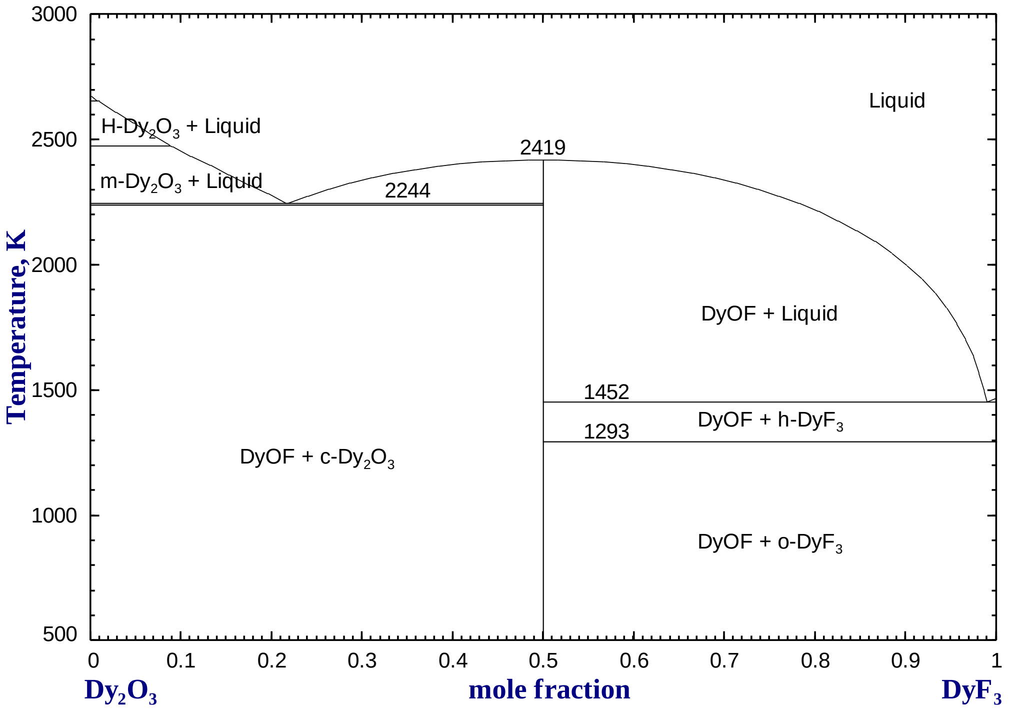
3000
2500
2000
1500
1000
500
Temperature, K
Liquid
H-Dy2O3 + Liquid
m-Dy2O3 + Liquid
2419
2244
DyOF + Liquid
1452
DyOF + h-DyF3
1293
DyOF + c-Dy2O3
DyOF + o-DyF3
0
0.1
0.2
0.3
0.4
0.5
0.6
0.7
0.8
0.9
1
Dy2O3
mole fraction
DyF3

(i)

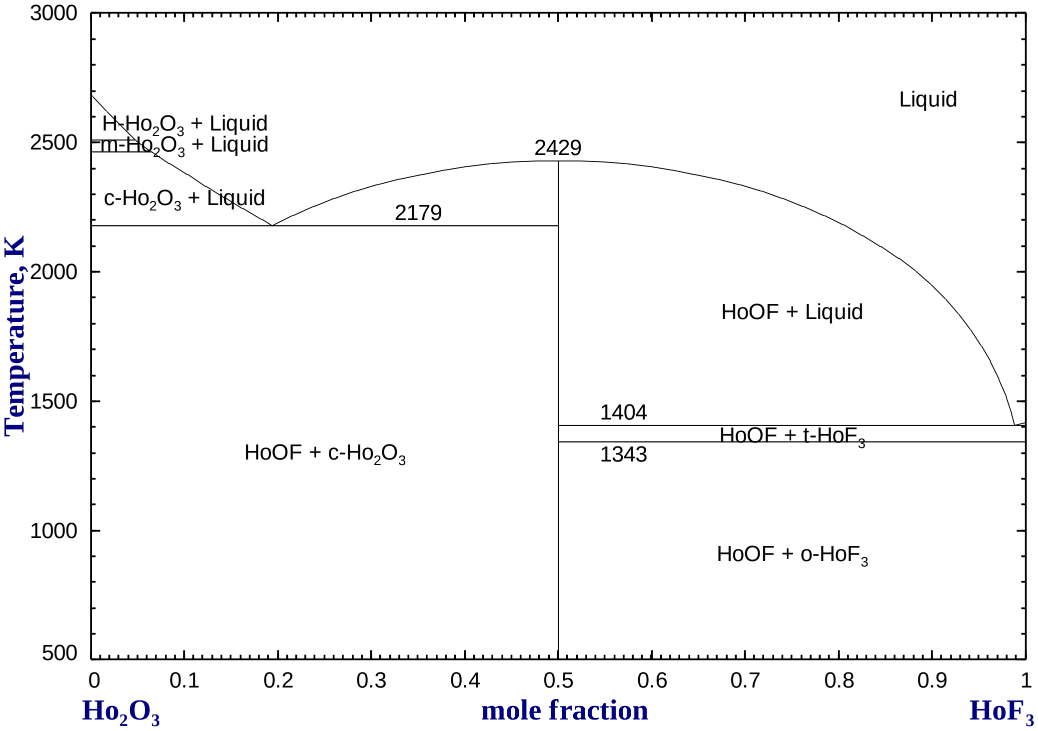
3000
2500
2000
1500
1000
500
Temperature, K
Liquid
H-Ho2O3 + Liquid
m-Ho2O3 + Liquid
2429
c-Ho2O3 + Liquid
2179
HoOF + Liquid
1404
HoOF + t-HoF3
1343
HoOF + c-Ho2O3
HoOF + o-HoF3
0
0.1
0.2
0.3
0.4
0.5
0.6
0.7
0.8
0.9
1
Ho2O3
mole fraction
HoF3

(j)

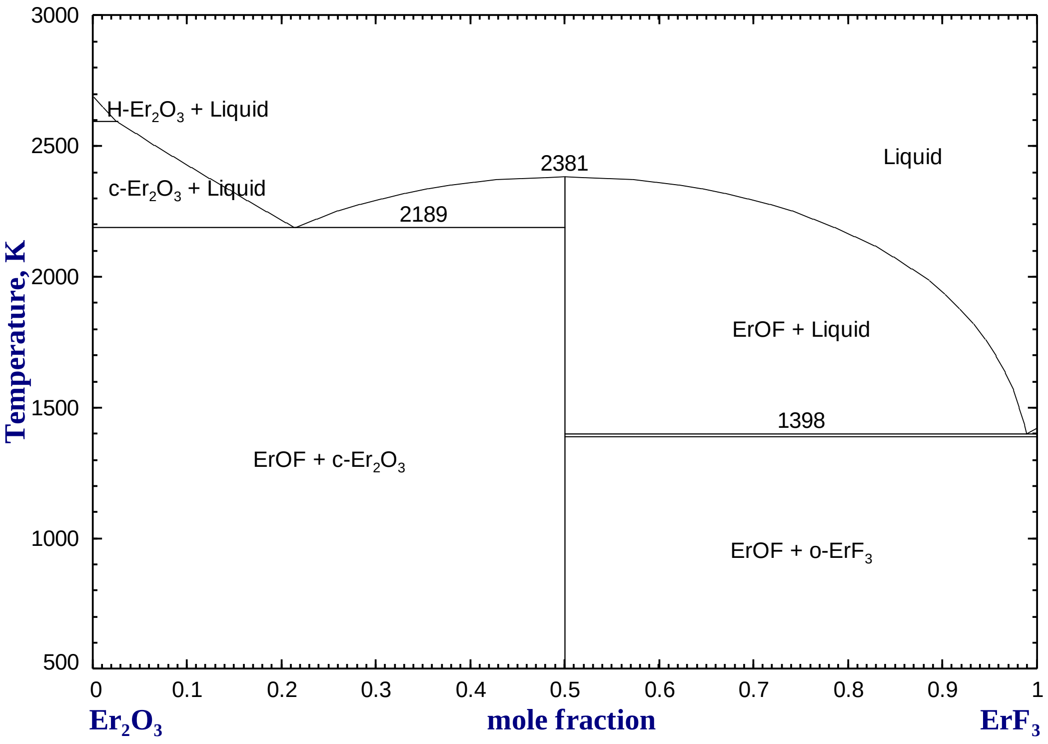
3000
2500
2000
1500
1000
500
Temperature, K
H-Er_2O_3 + Liquid
c-Er_2O_3 + Liquid
2381
2189
Liquid
ErOF + Liquid
1398
ErOF + c-Er_2O_3
ErOF + o-ErF_3
0
0.1
0.2
0.3
0.4
0.5
0.6
0.7
0.8
0.9
1
Er_2O_3
mole fraction
ErF_3

(k)

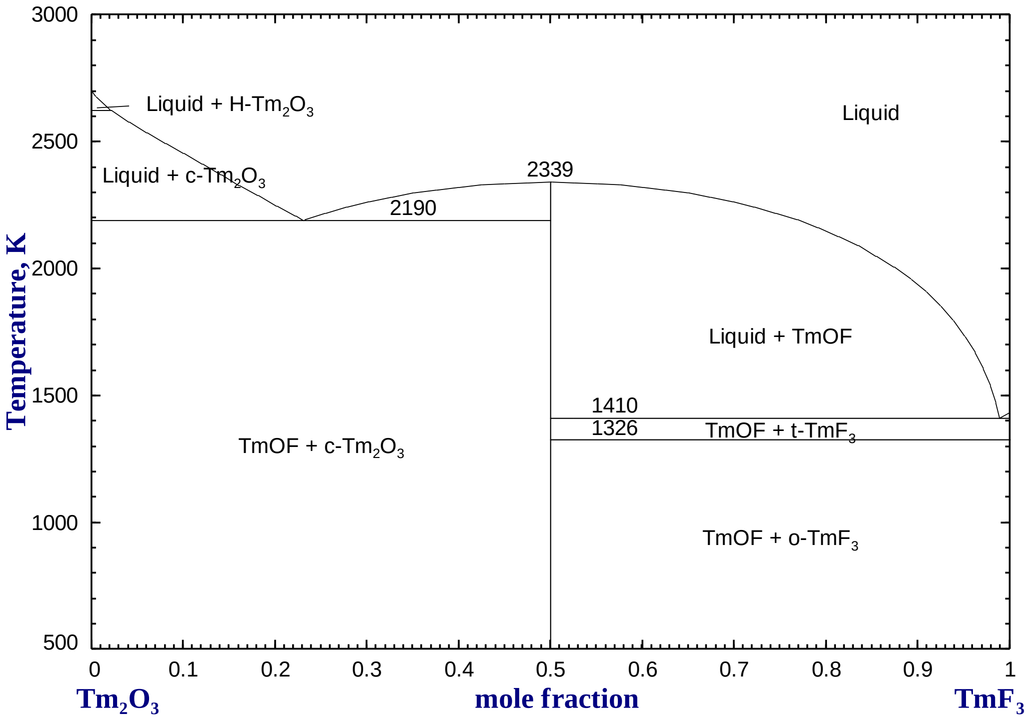
3000
2500
2000
1500
1000
500
Temperature, K
Liquid + H-Tm_2O_3
Liquid + c-Tm_2O_3
2339
2190
Liquid
Liquid + TmOF
1410
1326
TmOF + t-TmF_3
TmOF + c-Tm_2O_3
TmOF + o-TmF_3
0
0.1
0.2
0.3
0.4
0.5
0.6
0.7
0.8
0.9
1
Tm_2O_3
mole fraction
TmF_3

(l)

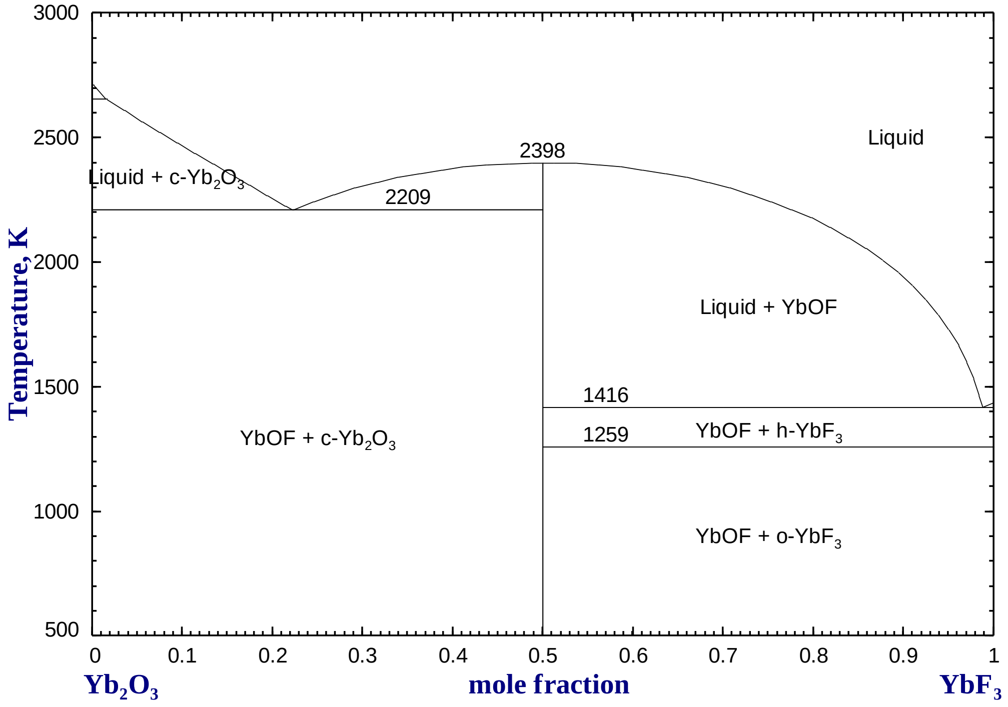
3000
2500
2000
1500
1000
500
Temperature, K
0
0.1
0.2
0.3
0.4
0.5
0.6
0.7
0.8
0.9
1
Yb_2O_3
mole fraction
YbF_3
Liquid
2398
Liquid + c-Yb_2O_3
2209
Liquid + YbOF
1416
YbOF + c-Yb_2O_3
1259
YbOF + h-YbF_3
YbOF + o-YbF_3

(m)

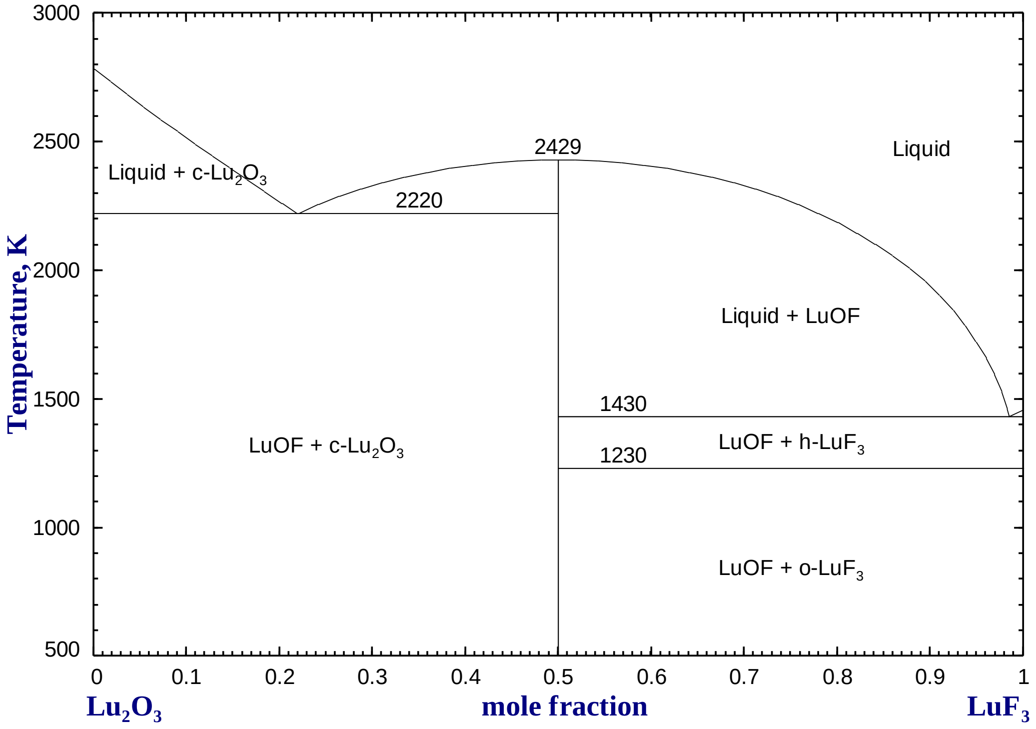
3000
2500
2000
1500
1000
500
Temperature, K
0
0.1
0.2
0.3
0.4
0.5
0.6
0.7
0.8
0.9
1
Lu_2O_3
mole fraction
LuF_3
Liquid
2429
Liquid + c-Lu_2O_3
2220
Liquid + LuOF
1430
LuOF + c-Lu_2O_3
LuOF + h-LuF_3
1230
LuOF + o-LuF_3

(n)

Fig. A-2 Predicted phase diagrams of the RE_2O_3-REF_3 systems in the present study.

(a) La_2O_3-LaF_3, (b) Ce_2O_3-CeF_3, (c) Pr_2O_3-PrF_3, (d) N_2O_3-NdF_3, (e) Sm_2O_3-SmF_3, (f) Eu_2O_3-EuF_3, (g) Gd_2O_3-GdF_3, (h) Tb_2O_3-TbF_3, (i) Dy_2O_3-DyF_3, (j) Ho_2O_3-HoF_3, (k) Er_2O_3-ErF_3, (l) Tm_2O_3-TmF_3, (m) Yb_2O_3-YbF_3, and (n) Lu_2O_3-LuF_3.

* c-, h-, m-, o-, H-, and X- represent cubic, hexagonal, monoclinic, orthorhombic, high temperature hexagonal, and high temperature cubic, respectively.

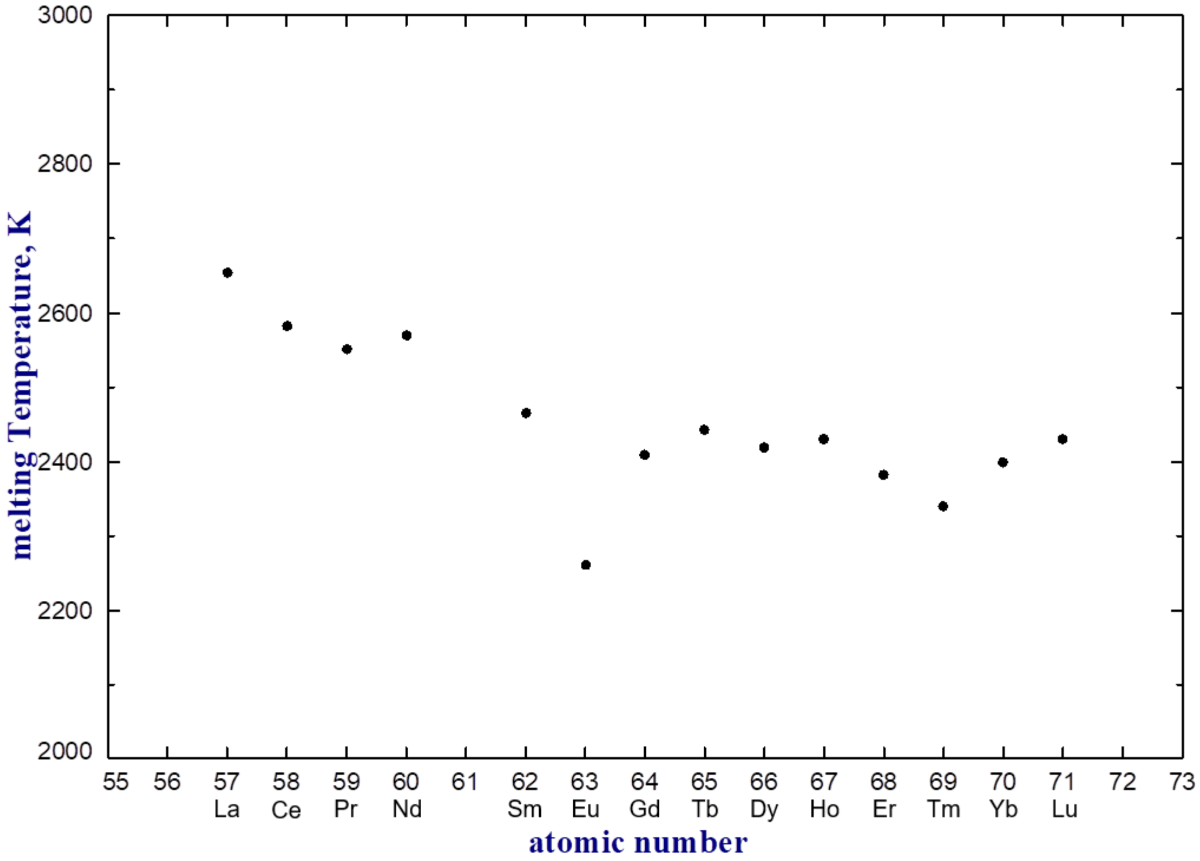

Fig. A-3 Predicted trend in the melting temperature of REOF in the RE_2O_3-REF_3 systems.

References

[1] FactSage. www.FactSage.com. FactSage 8.0., (n.d.).

[2] A.D. Pelton, S.A. Degterov, G. Eriksson, C. Robelin, Y. Dessureault, The modified quasichemical model I—Binary solutions, Metallurgical and Materials Transactions B 31(4) (2000) 651-659.

[3] A.D. Pelton, P. Chartrand, G. Eriksson, The modified quasi-chemical model: Part IV. Two-sublattice quadruplet approximation, Metallurgical and Materials Transactions A 32(6) (2001) 1409-1416.

[4] M. Hillert, The compound energy formalism, Journal of Alloys and Compounds 320(2) (2001) 161-176.

[5] S. Baek, I.-H. Jung, Phase diagram study and thermodynamic assessment of the Y2O3-YF3 system, Journal of the European Ceramic Society (2022).

[6] D.P. Kim, J.W. Yeo, C.I. Kim, Etching properties of Al2O3 films in inductively coupled plasma, Thin Solid Films 459(1-2) (2004) 122-126.

[7] K. Miwa, N. Takada, K. Sasaki, Fluorination mechanisms of Al2O3 and Y2O3 surfaces irradiated by high-density CF4/O2 and SF6/O2 plasmas, Journal of Vacuum Science & Technology A Vacuum Surfaces and Films 27 (2009).

[8] S.H. Park, K.E. Kim, S.J. Hong, Surface Analysis of Chamber Coating Materials Exposed to CF4/O2 Plasma, Coatings 11(1) (2021) 105.

[9] T. Tsunoura, K. Yoshida, T. Yano, Y. Kishi, Fabrication, characterization, and fluorine-plasma exposure behavior of dense yttrium oxyfluoride ceramics, Japanese Journal of Applied Physics 56 (2017) 06HC02.

[10] S. Lee, J. Lee, W. Kim, N.-M. Hwang, Plasma Etching Behavior of YOF Coating Deposited by Suspension Plasma Spraying in Inductively Coupled CHF3/Ar Plasma, Coatings 10(11) (2020).

[11] Y. Shiba, A. Teramoto, T. Goto, Y. Kishi, Y. Shirai, S. Sugawa, Stable yttrium oxyfluoride used in plasma process chamber, Journal of Vacuum Science & Technology A: Vacuum, Surfaces, and Films 35 (2017) 021405.

[12] V.A. Levitskii, G.M. Balak, Determination of the Thermodynamic Properties of the Oxide Fluorides of Yttrium and of the Rare-earth Metals by the E.m.f. Method with a fluoride Ion Electrolyte, Russian Journal of Physical Chemistry 56(5) (1982) 7.

[13] V.M. Vintonyak, Y.Y. Skolis, V.A. Levitski, Y.I. Gerasimov, Determination of the thermodynamic properties of yttrium oxyfluorides by the EMF method using solid fluorine-ion electrolyte, Doklady Akademii Nauk SSSR 273(2) (1983) 368-370.

[14] Y.Y. Skolis, S.V. Pashina, Phase relations and the thermodynamic properties of phases in the Y2O3-YF3 system, Russian Journal of Physical Chemistry A 75 (2001) 1774-1779.

[15] I.-H. Jung, M.-A. Van Ende, Computational Thermodynamic Calculations: FactSage from CALPHAD Thermodynamic Database to Virtual Process Simulation, Metallurgical and Materials

Transactions B 51(5) (2020) 1851-1874.

[16] C.W. Bale, E. Bélisle, P. Chartrand, S.A. Decterov, G. Eriksson, A.E. Gheribi, K. Hack, I.H. Jung, Y.B. Kang, J. Melançon, A.D. Pelton, S. Petersen, C. Robelin, J. Sangster, P. Spencer, M.A. Van Ende, FactSage thermochemical software and databases, 2010–2016, Calphad 54 (2016) 35-53.

[17] W. Zachariasen, Crystal chemical studies of the 5f-series of elements. XIV. Oxyfluorides, XOF, Acta Crystallographica 4(3) (1951) 231-236.

[18] K. Niihara, S. Yajima, The Crystal Structure and Nonstoichiometry of Rare Earth Oxyfluoride, Science reports of the Research Institutes, Tohoku University. Ser. A, Physics, chemistry and metallurgy 23 (1971) 218.

[19] A.W. Mann, D.J.M. Bevan, The crystal structure of stoichiometric yttrium oxyfluoride, YOF, Acta Crystallographica Section B 26(12) (1970) 2129-2131.

[20] D.J.M. Bevan, R.S. Cameron, A.W. Mann, G. Brauer, U. Roether, New oxyfluoride phases of the rare-earth metals and yttrium, Inorganic and Nuclear Chemistry Letters 4(4) (1968) 241-247.

[21] D.B. Shinn, H.A. Eick, Phase analyses of lanthanide oxide fluorides, Inorganic Chemistry 8(2) (1969) 232-235.

[22] K. Niihara, S. Yajima, Studies of Rare Earth Oxyfluorides in the High-temperature Region, Bulletin of the Chemical Society of Japan 45(1) (1972) 20-23.

[23] D.J.M. Bevan, A.W. Mann, The crystal structure of Y7O6F9, Acta Crystallographica Section B 31(5) (1975) 1406-1411.

[24] A.W. Mann, D.J.M. Bevan, Intermediate fluorite-related phases in the Y2O3 YF3 system—Examples of one-dimensional ordered intergrowth, Journal of Solid State Chemistry 5(3) (1972) 410-418.

[25] B.P. Sobolev, P. Fedorov, D.B. Shteynberg, B.V. Sinitsyn, G.S. Shakhkalamian, On the problem of polymorphism and fusion of lanthanide trifluorides. I. The influence of oxygen on phase transition temperatures, Journal of Solid State Chemistry 17 (1976) 191-199.

[26] Y. Zhang, I.-H. Jung, Critical evaluation of thermodynamic properties of rare earth sesquioxides (RE = La, Ce, Pr, Nd, Pm, Sm, Eu, Gd, Tb, Dy, Ho, Er, Tm, Yb, Lu, Sc and Y), Calphad 58 (2017) 169-203.

[27] I. Barin, Thermochemical Data of Pure Substances1995, pp. 1815-1885.

[28] G. Eriksson, A.D. Pelton, Critical evaluation and optimization of the thermodynamic properties and phase diagrams of the CaO-Al2O3, Al2O3-SiO2, and CaO-Al2O3-SiO2 systems, Metallurgical Transactions B 24(5) (1993) 807-816.

[29] R.J. Gaboriaud, F. Paumier, B. Lacroix, Disorder–order phase transformation in a fluorite-related oxide thin film: In-situ X-ray diffraction and modelling of the residual stress effects, Thin Solid Films 601 (2015).

[30] V.A. Levitskii , P.B. Narchuk, J. Hekimov, J.I. Gerassimov, Thermodynamic Study of Some Solutions in the CaO-ZrO2 System by emf Method, Journal of Solid State Chemistry 20 (1977) 119-125.

[31] S. Kwon, W.-Y. Kim, P. Hudon, I.-H. Jung, Thermodynamic modeling of the CaO-SiO2-ZrO2

system coupled with key phase diagram experiments, Journal of the European Ceramic Society 37 (2016).

[32] H. Kopp, Investigations of the Specific Heat of Solid Bodies, Philosophical Transactions of the Royal Society of London 155 (1865) 71-202.

[33] H. Prophet, D.R. Stull, JANAF thermochemical tables, U.S. Department of Commerce, Washington (1985).

[34] D.-M. Kim, Y.-S. Oh, S. Kim, H.-T. Kim, D.-S. Lim, S.-M. Lee, The erosion behaviors of Y2O3 and YF3 coatings under fluorocarbon plasma, Thin Solid Films 519(20) (2011) 6698-6702.

[35] H.-M. Oh, Y.-J. Park, H.-N. Kim, K. Kumar, J.-W. Ko, C.-E. Lee, H.-K. Lee, Remarkable plasma-resistance performance by nanocrystalline Y(2)O(3)·MgO composite ceramics for semiconductor industry applications, Scientific reports 11(1) (2021) 10288-10288.

[36] D.-M. Kim, M.-R. Jang, Y.-S. Oh, S. Kim, S.-M. Lee, S.-H. Lee, Relative sputtering rates of oxides and fluorides of aluminum and yttrium, Surface and Coatings Technology 309 (2017) 694-697.

[37] R. Marder, R. Chaim, G. Chevallier, C. Estournès, Effect of 1wt% LiF additive on the densification of nanocrystalline Y2O3 ceramics by spark plasma sintering, Journal of the European Ceramic Society 31(6) (2011) 1057-1066.

[38] W. Hinz, P.-O. Kunth, Phase equilibrium data for the system MgO-MgF2-SiO2, American Mineralogist 45(11-12) (1960) 1198-1210.

[39] J. Berak, I. Tomczak, Phase equilibria in the system MgO–P2O5–MgF2. I. The systems: MgO–MgF2, Mg3 (PO4) 2–MgF2, MgO–Mg3 (PO4) 2–MgF2, Roczniki Chemii (Ann. Soc. Chim. Polonorum) 39 (1965) 519-525.

[40] J. Tomlinson, B. Welch, The solubilities of MgO and UO2 in molten MgF2, Journal of Inorganic and Nuclear Chemistry 28(10) (1966) 2131-2136.

[41] R.A. Sharma, Phase Equilibria and Structural Species in MgF2-MgO, MgF2-CaO, and MgF2-Al2O3 Systems, Journal of the American Ceramic Society 71(4) (1988) 272-276.

[42] S.G. Tresvyatskii, L.M. Lopato, A.A. Ogorodnikova, A.V. Shevchenko, PHASE DIAGRAMS OF THE SYSTEMS FORMED BY YTTRIUM, ERBIUM, AND YTTERBIUM OXIDES WITH MAGNESIUM OXIDE, (1971).

[43] R.H. Nafziger, R.L. Lincoln, N. Riazance, High-temperature thermal analysis of the systems LaF3 YF3, SrF2 YF3 and MgF2 YF3, Journal of Inorganic and Nuclear Chemistry 35(2) (1973) 421-426.

[44] L.A. Olkhovaya, P.P. Fedorov, D.D. Ikrami, B.P. Sobolev, Phase diagrams of MgF2-(Y, Ln)F3 systems, Journal of thermal analysis 15(2) (1979) 355-360.

[45] R.G. Berman, T.H. Brown, Heat capacity of minerals in the system Na2O-K2O-CaO-MgO-FeO-Fe2O3-Al2O3-SiO2-TiO2-H2O-CO2: representation, estimation, and high temperature extrapolation, Contributions to Mineralogy and Petrology 89(2) (1985) 168-183.

[46] C. Ji, Z. Xi, Standard Gibbs free energy of formation of neodymium oxyfluoride and borates, Journal of the Less Common Metals 158(2) (1990) 191-198.

[47] Y.R. Hong, R.V. Kumar, D.A.R. Kay, The high temperature thermodynamics of the La-O-F and Ce-O-F systems, Academic Press Inc, United States, 1985.

요약 (국문 초록)

$MgO-MgF_2-Y_2O_3-YF_3$ 4원계 시스템의 상태도 실험과 열역학 모델링

백 승 주
재료공학부
공과대학 대학원
서울대학교

열역학 특성과 상평형을 이해하기 위해 신뢰성 있는 열역학 데이터 베이스의 구축은 야금, 유리 제조 및 엔지니어링, 세라믹 제조를 포함한 고온 재료 가공에서 매우 중요하다. 반도체 공정에서 사용되는 세라믹 히터가 플라즈마 가스에 노출 됨에 따라 부식 및 수율 저하 문제가 발생하였고 그에 따라 새로운 코팅 물질에 대한 연구의 필요가 대두되었다. 따라서 본 연구에서는 CALculation of PHAse Diagram (CALPHAD) 방법을 기반으로 $MgO-MgF_2-Y_2O_3-YF_3$ 시스템의 열역학 데이터베이스를 개발하였다. Y2O3-YF3 이원계 시스템 및 MgO-MgF2-Y2O3-YF3 reciprocal 시스템의 상태도 및 열역학 실험 데이터가 매우 부족하기 때문에 상평형 실험 및 시차 열분석 (DTA) 기법을 이용하여 연구를 진행하였다. 평형상은 electron probe microanalysis (EPMA)와 X-ray diffraction (XRD)을 통해 분석하여 확인하였다. 본 연구를 통해 처음으로 옥시 불화 이트륨계 시스템의 전체 상태도가 연구되었고 고용체인 Y_2O_3 상은 1973 K에서 5 mol % 이상의 YF_3 상을 용해

하는 것으로 밝혀졌다. YOF 및 vernier 상의 융점은 1973 K 이상으로 밝혀졌고, 실험을 통해 YF_3 상 부근의 액상선의 조성이 결정되었다. $MgO-MgF_2-Y_2O_3-YF_3$ 시스템의 상태도는 처음으로 1273 K에서 1773 K까지 연구되었고 공융점과 등온 액상선을 정밀하게 분석하였다. 3원 혹은 4원 화합물은 확인되지 않았다. 실험을 통해 얻은 상태도 데이터와 문헌의 열역학 성질 데이터를 기반으로 $Y_2O_3-YF_3$ 및 $MgO-MgF_2-Y_2O_3-YF_3$ 시스템을 CALPHAD 방법을 이용하여 열역학 모델링하였고 정밀한 데이터베이스를 구축할 수 있었다. 데이터베이스의 응용으로 플라즈마 에칭 공정 동안 옥시 불화 이트륨계 시스템의 증기압을 계산하였고 이를 불화 알루미늄의 증기압과 비교하였다. 또한 준안정 상태에서 Y_2O_3 고용체에 YF_3가 용해되는 정도를 계산하였고 이를 Y_2O_3의 결정 구조를 통해 분석하였다.

Keywords : $MgO-MgF_2-Y_2O_3-YF_3$, YOF, Phase Diagram, Thermodynamics, CAPHAD